Université de Toulouse

THÈSE

En vue de l'obtention du

DOCTORAT DE L'UNIVERSITÉ DE TOULOUSE

Délivré par *l'INSTITUT NATIONAL DES SCIENCES APPLIQUEES DE TOULOUSE*
Discipline ou spécialité : *Nanophysique*

Présentée et soutenue par

Fan ZHAO

Le *7 juillet 2010*

Recombinaison Dépendante du Spin dans les Semiconducteurs Nitrures Dilués

---

JURY

Maria CHAMARRO	*Rapporteur*
Denis SCALBERT	*Rapporteur*
Daniel PAGET	*Examinateur*
Chantal FONTAINE	*Examinateur*
Andrea BALOCCHI	*Co-Directeur de thèse*
Xavier MARIE	*Directeur de thèse*

Ecole doctorale : *Sciences de la Matière*
Unité de recherche : *Laboratoire de Physique et Chimie de Nano-Objets, INSA-CNRS-UPS, UMR 5215*

Spécialité : Nanophysique
Nom : Zhao
Prénom : Fan

Thèse effectuée au : Laboratoire de Physique et Chimie des Nano-Objets de l'Institut National des Sciences Appliquées.

Titre de la thèse en français : Recombinaison dépendante du spin dans les semiconducteurs nitrures diluées.

Ce travail de thèse est une contribution à l'étude des propriétés de spin dans les semiconducteurs par spectroscopie de photoluminescence et par photoconductivité en vue d'applications possibles dans le domaine de l'électronique du spin.

Nous avons analysé les propriétés de spin des électrons de conduction dans les matériaux semiconducteurs nitrures dilués, massif et puits quantiques (GaAsN, GaAsN/GaAs). Nous avons étudié le mécanisme de recombinaison dépendante du spin des électrons de conduction sur les centres paramagnétiques induits par l'introduction d'azote dans GaAs. Nous avons mis en évidence l'effet de « filtrage » de spin des électrons de conduction que ce mécanisme peut induire ; en particulier, nous avons mené des études détaillées en fonction de la concentration d'azote, de la puissance excitatrice, d'un champ magnétique externe et, pour les hétérostructures, de l'épaisseur des puits quantiques. L'origine chimique des centres paramagnétiques a été, de plus, identifiée par des études de résonance paramagnétique détectée optiquement (ODMR).

Nous avons également complété ces études purement optiques sur la recombinaison dépendante du spin, par des expériences de photoconductivité en vue d'applications possibles liées à l'électronique du spin. Nous avons montré que la photoconductivité des matériaux nitrures dilués peut être contrôlée par la polarisation de la lumière incidente. Un détecteur électrique de la polarisation de la lumière à base de GaAsN a été ainsi fabriqué et testé.

Ces résultats ont été également interprétés et simulés grâce à un système d'équations dynamiques pouvant rendre compte à la fois des résultats de photoluminescence et de transport.

Mots-Clés : Spintronique, Electronique de spin, Recombinaison dépendante du spin, Spectroscopie ultra-rapide, Photoluminescence, Photoconductivité, Semiconducteurs nitrures, hétérostructures semiconductrices.

Remerciements

Je voudrais remercier toutes les personnes, qui m'ont apporté, de près ou de loin, leur aide, leur soutien, leurs encouragements...

Ce fut un privilège pour moi d'effectuer mes études sous la direction du Professeur Xavier Marie et du Dr Andrea Balocchi. C'est donc à eux que je dédie mes remerciements les plus sincères.

Merci à Xavier pour avoir encadré cette thèse et pour m'avoir mis sur la voie grâce à ses profondes connaissances dans le domaine des Spintronics, domaine nouveau pour moi, et pour lequel j'ai pu bénéficier de conseils constructifs et d'explications lumineuses.

Merci à Andréa pour avoir co-encadré ma thèse. Merci de m'avoir guidé pour une bonne utilisation des dispositifs expérimentaux et des appareils. Nos discussions ont toujours été précieuses que ce soit au niveau des manipulations ou de la compréhension des résultats. Merci également pour l'aide apportée dans la rédaction de ma thèse en anglais.

Un grand merci à Messieurs Thierry Amand et Alejando Kunold pour leurs explications et nos discussions sur les points essentiels qui m'ont permis de comprendre plus en profondeur mon sujet de recherche.

J'aimerais remercier vivement Madame Hélène Carrère, Monsieur Pierre Rénucci, Monsieur Bernhard Urbaszek pour leurs aides et leurs expositions pendant ma thèse.

Je remercie l'ensemble du jury: Madame Chantal Fontaine ,Monsieur Daniel Paget, pour leur participation à l'évaluation de ce travail et plus particulièrement Madame Maria Chamarro et Monsieur Denis Scalbert pour avoir accepté d'en être les rapporteurs.

Pour les doctorants et post-doctorants:

Delphine Lagarde, qui m'a aiguillé au début de mon intégration de l'équipe de recherche.

Thomas Belhadj et Claire-Marie Simon, avec lesquels tant d'activités ont été réalisées, et qui m'ont sauvé de si nombreuses procédures inconnues tout au long de ces 3 ans !

Pierre-Marie, dont la bonne humeur et l'humour ont été appréciables au bureau.

Giang, qui a toujours été d'excellent conseil pour la vie de tous les jours.

Un grand merci à vous tous !

Et pour les nouveaux doctorants, Sergei et Ha, je vous souhaite une très bonne continuation!

Merci également à Cathy et Mohammed pour leurs aides techniques.

Je remercie les secrétaires de notre laboratoire et Madame Fortuné, qui m'ont beaucoup aidé pour les dossiers administratifs.

Je tiens à remercier l'équipe du Professeur W.M.Chen du département de Physique-Chimie et de Biologie de l'Université de Linköping pour ses efforts significatifs au sujet de l'identification des centres paramagnétiques .

Je remercie l'équipe du Professeur Baoli Liu et le doctorant Hongming Zhao de L 'institut de Physique de l'Académie Chinoise des Sciences, pour sa collaboration et ses conversations agréables.

Je remercie les organisateurs du programme CSC/UT-INSA dont le financement a facilité ma venue en France pour réaliser ma thèse.

Je remercie tous les membres du programme CSC/UT-INSA à Toulouse: Ruijin, Yanwen, Junfeng, Susu, Hongwei, Xiaoxiao, Yanping, Binhong, Letian, Lei pi, Jing Xiao, Zhe Chen, Xinwei, Dong dong, Haojun, Hutao, Linqing, Hong Liu, Juan Lu.

Enfin, un grand merci à mes parents, qui m'ont toujours apporté leur précieux et affectueux soutien, et plus particulièrement lors de cette thèse lorsqu'il fallait avoir la force d'avancer et le courage de surmonter les moments de tristesse et de démotivation .

Table of content

Introduction

Representing an additional degree of freedom, independent from the charge, the spin has been proposed as a novel mean of storing and manipulating the information in future Spintronic devices. The possibility of controlling the carriers' spins state and charge, of tailoring the fundamental transition energy through band gap engineering or material alloying together with the well established industrial technology "savoir-faire", confer the semiconductor materials a key role in the Spintronics scenario.

The first works on the semiconductor spins properties have started already in the '70s, but it is only very recently that the research on this subject has attracted considerable attention. Several fundamental and technological stumbling blocks have still to be addressed before the spin could be integrated in "real" devices. Storing and manipulating the spin, for example, require the spin orientation to be stable over a reasonably long period of time and preferably at room temperature. Injection and transport of spin polarised carriers in addition to spin filtering and electrical spin detections are all so far restricted to a limited efficiency and primarily at low temperatures or under a magnetic field. Nevertheless, very promising results have been obtained by confining the carriers in the three spatial direction in nanometre-sized objects such as (In)GaAs or CdTe quantum dots, or more recently on wide gap (In)GaN materials.

Another approach has been lately gaining its way in the spintronic field, which does not rely on nano-structuring but rather on the engineering of deep defects in bulk or epilayer materials. Examples of this technique can be found with P atoms in Si, or N vacancies in Diamond. For instance, coherent manipulation of the defect electronic states, or large spin polarisation of carriers have been achieved in one or the other of this novel systems thanks to the relatively long defects' spin relaxations times.

Stemming from this last approach, this work aims at studying, by optical and transport techniques, the spin properties of carriers in dilute nitride GaAsN epilayers and heterostructures possessing deep paramagnetic centres. We show in this manuscript that the electron spin dynamics in GaAsN is governed by a very efficient Spin Dependent Recombination mechanism on these deep centres. This mechanism was evidenced more than 30 years ago by optical orientation experiments by C.Weisbuch and G.Lampel in AlGaAs and D.Paget in GaAs.

The manuscript is organised in four chapters:

The first chapter is dedicated to a concise description of the essential notions necessary for the comprehension of the physical phenomena governing the spin properties in III-V zinc-blende semiconductors. The fundamentals of the band structure theory, the optical selection rules and the spin relaxation mechanisms are briefly presented.

In Chapter 2 we present the different experimental set-ups used for the realisation of this work. The time and polarisation resolved photoluminescence set-up and the photoconductivity experiments are here introduced. We will also detail the Optically Detected Magnetic Resonant (ODMR) set-up used in the framework of our collaboration with the Linköping University in Sweden.

In Chapter 3 we will present the results obtained on the carrier spin properties in dilute nitride GaAsN epilayer and heterostructures by photoluminescence and ODMR spectroscopy. We will show how the paramagnetic defects can confer spin filtering properties to GaAsN, features which can be effectively interpreted in terms of the Spin Dependent Recombination mechanism of electrons on the paramagnetic centres. In particular we will address the role of the N fraction, the open question of the nature of the paramagnetic centres, the efficiency of the spin-filtering of heterostructures.

The Spin Dependent Photoconductivity of dilute nitride GaAsN is the subject of Chapter 4. By combining optical spin injection techniques with transport spectroscopy tools, we will evidence how the polarisation of an incident light can as well modulate the photoconductivity of GaAsN. The very similar polarisation features obtained by photoluminescence and photoconductivity experiments namely as a function of the light polarisation and intensity or under the influence of an external magnetic field will lead us to the outcome that the same SDR mechanism is at the origin of both optical and transport observations. We will conclude this chapter and thesis with the description of the transport theoretical model used to interpret the experimental data.

Chapter 1

Introduction to the electronic and optical properties of zinc blende III-V semiconductors

To pave the way for the following chapters, this first chapter concisely presents the fundamentals of band structure, optical orientation rules and spin relaxation mechanisms of III-V zinc blende materials.

My work has been essentially devoted to the study by photoluminescence and photoconductivity experiments of the spin properties of carriers in dilute GaAsN semiconductors. We start therefore, with an introduction of the electronic band structure at the centre of the Brillouin zone of III-V zinc-blende semiconductors. We will briefly present the electronic properties of bulk materials as well as of heterostructures, namely Quantum Wells.

We will then detail the fundamental principles of optical orientation experiments which are a consequence of the optical selection rules governing the interaction of electromagnetic radiation with the system under study. We will thus show how to link these selection rules to the polarisation of the incident or emitted light and the spin polarisation of the photogenerated carriers. These are the principles used in this work to study the spin polarisation properties of semiconductors by photoluminescence and photoconductivity experiments.

Finally, the main mechanisms responsible for the spin relaxation of carriers in semiconductor will be concisely reviewed.

1.1 Electronic structure of III-V zinc-blende semiconductors: from bulk to the heterostructure

1.1.1 Bulk materials

We will briefly present in this part the main characteristics of the electronic band structure of materials crystallizing in the zinc blende structure (*GaAs, InAs, etc…,* and relative alloys). The zinc blende structure belongs to the T_d representation group. In the case of a binary compound, the two atom types form two interpenetrating face-centred cubic lattices. The arrangement of the two types of atoms is the same as diamond cubic structure, but with alternating types of atoms at neighbouring lattice sites (see fig.1.1).

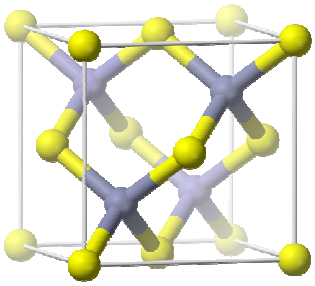

Fig.1.1 - *Schematic representation of the zinc blende structure.*

The Hamiltonian describing an electron in a crystal periodic potential *V*(r) can be expressed as:

$$H = \frac{-\hbar^2}{2m_0}\Delta_r + V(\vec{r}) \tag{1.1}$$

where m_0 is the electron mass in vacuum. According to the Bloch theorem, the wave function $\Psi_{n,\mathbf{k}}$ of the electron moving in such a potential is given by:

$$\Psi(\vec{r}) = u(\vec{r})e^{i\vec{k}\cdot\vec{r}} \tag{1.2}$$

where ***k*** is the wave vector associated to the electron and *u* is a function having the same periodicity of the crystal potential. In a bulk material, the carriers are free to move along the three direction of the space and the solution of Schrödinger equation gives the electron eigenenergies which are described by different bands, divided into conduction and valence bands, the latter being the lowest

unpopulated band at T=0 K. The solution of Schrödinger equation with Hamiltonian Eq.(1.1) at the zone centre (***k***=0), gives the eigenenergies of the band extreme. The energy corresponding to the conduction band is denoted $E_{c,0}$ and it's denoted |S> due to its spherical symmetry, whereas the threefold degenerate solutions of the valence bands of energy $E_{v,0}$ are noted |X>, |Y>, |Z> in analogy to the eigenfunctions of the Hydrogen atom p states.

Taking into account the electron spin and its interaction with the orbital angular momentum, it introduces a supplementary term W_{SO} in the crystal Hamiltonian H_0 (Eq.(1.1)).

$$H = H_0 + W_{SO} = \frac{p^2}{2m_0} + V(\vec{\boldsymbol{r}}) + \frac{\hbar}{4m_0^2c^2}\boldsymbol{\sigma}\cdot(\nabla V(\vec{\boldsymbol{r}})\times p) \tag{1.3}$$

The third term in Eq.(1.3) can be converted into Thomas form in spherical symmetry:

$$\frac{\hbar}{4m_0^2c^2}\boldsymbol{\sigma}\cdot(\nabla V(\vec{\boldsymbol{r}})\times p) = \frac{\hbar^2}{2m_0^2c^2}\frac{1}{\vec{r}}\frac{dV}{dr}(\vec{L}\cdot\vec{S}) \tag{1.4}$$

where $\boldsymbol{\sigma}$ is Pauli matrix, and

$$\left\langle \vec{L}\cdot\vec{S}\right\rangle = \frac{1}{2}\left\langle \vec{J}^2 - \vec{L}^2 - \vec{S}^2\right\rangle = \frac{1}{2}\left[j(j+1) - l(l+1) - s(s+1)\right] \tag{1.5}$$

where $\boldsymbol{L}$, (l) is the orbital angular momentum (and corresponding quantum number); $\boldsymbol{S}$, (s) spin angular momentum (spin quantum number, ±1/2); $\boldsymbol{J}=\boldsymbol{L}+\boldsymbol{S}$, ($j$) is total angular momentum (total angular momentum quantum number). To a first approximation, the spin-orbit interaction leaves the conduction bands unchanged (as the Thomas term is zero) whereas it lifts the degeneracy of the valence bands which at the zone centre are separated into a group of two double degenerate bands called heavy and light holes (HH, LH bands) and a third doubly degenerate "split-off" band (SO) repelled at a lower energy, characteristic of the spin-orbit interaction Δ_{SO}. This energy is considerable in the case of GaAs and corresponds to Δ_{SO} =341 meV [1].

The solution of Eq.(1.3) gives the system eigenenergies and eigenfunctions, and the results obtained at the zone centre are summarized in table 1.1 and given in the base {|S↑>, |S↓>, |X↑>, |X↓>, |Y↑>, |Y↓>,|Z↑>, |Z↓>}.

Eigenfunction u_i	'Atomic' notations	Eigenenergies
$u_1 = \|S,\uparrow\rangle$ $u_2 = \|S,\downarrow\rangle$	$\|1/2,1/2\rangle$ $\|1/2,-1/2\rangle$	$E_c = E_{c,0}$
$u_3 = \frac{1}{\sqrt{6}}\|(X+iY),\downarrow\rangle - \sqrt{\frac{3}{2}}\|Z,\uparrow\rangle$ $u_4 = -\frac{1}{\sqrt{6}}\|(X-iY),\uparrow\rangle - \sqrt{\frac{3}{2}}\|Z,\downarrow\rangle$	$\|3/2,1/2\rangle$ $\|3/2,-1/2\rangle$	$E_{lh} = E_{v,0} + \Delta/3$
$u_5 = \frac{1}{\sqrt{2}}\|(X+iY),\uparrow\rangle$ $u_6 = \frac{1}{\sqrt{2}}\|(X-iY),\downarrow\rangle$	$\|3/2,3/2\rangle$ $\|3/2,-3/2\rangle$	$E_{hh} = E_{v,0} + \Delta/3$
$u_7 = \frac{1}{\sqrt{3}}\|(X+iY),\downarrow\rangle + \frac{1}{\sqrt{3}}\|Z,\uparrow\rangle$ $u_8 = \frac{-1}{\sqrt{3}}\|(X-iY),\uparrow\rangle + \frac{1}{\sqrt{3}}\|Z,\downarrow\rangle$	$\|1/2,1/2\rangle$ $\|1/2,-1/2\rangle$	$E_{so} = E_{v,0} - 2\Delta/3$

Tab.1.1 – *Bloch eigenfunctions at the zone centre for a zinc-blende semiconductor*

u_1 and u_2 represents the conduction band eigenfunctions, whereas u_3,u_4 and u_5,u_6 are respectively the light and heavy holes eigenstates. Finally u_7,u_8 separated by an energy equal to Δ_{SO} from the HH and LH, are the "split-off' bands.

To calculate the band structure at $\boldsymbol{k}\neq 0$, the semi-empirical $k\cdot p$ method can be used. By substituting the Bloch function into Schrödinger equation, we obtain

$$\left(\frac{-\hbar^2}{2m_0}\Delta_r + \frac{\hbar\vec{k}\cdot\vec{p}}{m_0} + \frac{\hbar^2k^2}{2m_0} + V(\vec{r})\right)u_{n,k}(\vec{r}) = E_{n,k}u_{n,k}(\vec{r}) \tag{1.6}$$

where the energies $E_{n,k=0}$ are considered known. The $k\cdot p$ method consists in treating the $\frac{\hbar \boldsymbol{k}\cdot\boldsymbol{p}}{m_0}$ operator as a perturbation to the Hamiltonian and, by considering small variation of the $\boldsymbol{k}$ vector from the zone centre, the energy eigenvalues at $\boldsymbol{k}\neq 0$ ($E_{n,\mathbf{k}}$) can be calculated as :

$$E_{n,k} = E_{n,0} + \frac{\hbar^2k^2}{2m_0} + \frac{\hbar^2}{m_0^2}\sum_{n'\neq n}\frac{\left|\left\langle u_{n,0}\middle|\vec{k}\cdot\vec{p}\middle|u_{n',0}\right\rangle\right|^2}{E_{n,0}-E_{n',0}} \tag{1.7}$$

From Eq.(1.7), we can see that in first approximation the evolution of the eigenenergy $E_{n,\mathbf{k}}$ as a function of the wave vector $\boldsymbol{k}$ can be considered parabolic and that a conduction band "effective mass" can be defined as:

$$\frac{1}{m_e} = \frac{1}{m_0} + \frac{2}{m_0^2k^2}\sum_{n'\neq n}\frac{\left|\left\langle u_{n,0}\middle|\vec{k}\cdot\vec{p}\middle|u_{n',0}\right\rangle\right|^2}{E_{n,0}-E_{n',0}} \tag{1.8}$$

The band structure of zinc blende semiconductors near Γ-point calculated according to the $k\cdot p$ method in first approximation is presented in Fig.1.2.

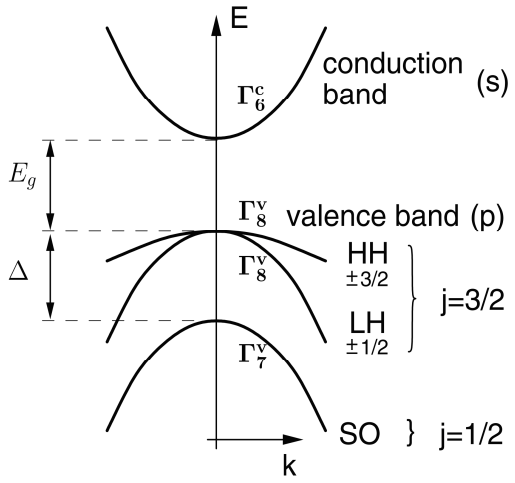

Fig.1.2 - *Band structure of zinc blende structure bulk material near Γ-point*

In order to correctly describe degenerate bands, as in the case of the HH and LH, the Kohn-Luttinger Hamiltonian is used, which is expressed in terms of the Kohn-Luttinger parameters γ_1, γ_2 and γ_3 as:

$$H_L = \frac{\hbar^2}{2m_0}\left[(\boldsymbol{\gamma}_1 + \frac{5}{2}\boldsymbol{\gamma}_2)\nabla^2 - 2\boldsymbol{\gamma}_2(\nabla\cdot\boldsymbol{J})^2 + 2(\boldsymbol{\gamma}_3 - \boldsymbol{\gamma}_2)(\nabla_x^2\cdot\boldsymbol{J}_x^2 + c.p.)\right] \quad (1.9)$$

where $\boldsymbol{J}=(J_x,J_y,J_z)$ is an total angular momentum operator and *c.p.* stands for cyclic permutations[2]. The eigenenergies of Eq.(1.9) are obtained in terms of the Kohn-Luttinger parameter,

$$E = E_{v,0} + \frac{\hbar^2}{2m_0}\left[\gamma_1 k^2 \pm 2\sqrt{\gamma_2(k_x^4+k_y^4+k_z^4) + 3(\gamma_3^2-\gamma_2^2)(k_x^2k_y^2+k_y^2k_z^2+k_z^2k_x^2)}\right] \quad (1.10)$$

and show that HH (positive sign) and LH (negative sign) valence bands, degenerate at $\boldsymbol{k}$=0, split for $\boldsymbol{k}\neq$0 into two bands characterised by different curvatures (thus different effective masses) which justify the previously introduced terminology of "heavy" and "light" hole bands. The relation between the HH and LH effective masses of in the (100) equivalent directions can be expressed by Luttinger parameters as:

$$\frac{m_0}{m_{HH}} = -\gamma_1 + 2\gamma_2 \qquad \frac{m_0}{m_{LH}} = -\gamma_1 - 2\gamma_2 \quad (1.11)$$

For GaAs, the values of the Luttinger parameters are γ_1=7.0, γ_2 =2.25 and γ_3 =2.9. [2, 3]

The remaining HH-LH degeneracy at *k*=0 can be lifted due to the strain caused by the lattice parameter mismatch between the epilayer and the host matrix if the epilayer does not relax the elastic energy, i.e. if the epilayer thickness is below the critical thickness (This value is several tens of nanometres for the N concentrations ([N]) lower than 3% in GaAsN grown on GaAs). In the case of GaAsN grown on GaAs, the biaxial tensile strain raises at *k*=0 the LH band above the HH one ≈24 meV for [N]=2%.

1.1.2 Semiconductor heterostructures

Starting from the 1970s, the development of Molecular Beam Epitaxy and related growth techniques, has allowed for a spectacular progress in the field of semiconductor physics and device applications. The sophistication offered by these growth techniques makes possible the control of the epilayer thickness down to a monolayer precision, allowing the growth of heterostructures of dimensions comparable to the carriers' wavelength (typically a few nanometres) thus showing

quantum confinement effects. The potential discontinuity obtained by the controlled juxtaposition of semiconductors of different energy gaps (called heterostructures) can confine the movement of carriers in one, two or three dimensions and we correspondingly speak of quantum wells, wires or dots. In this work we are concerned with quantum wells only and we will present their main properties in the following section.

More precisely, the term "heterostructures" is used to define a semiconductor structure whose chemical composition changes with position. The central feature of heterojunction is that the bandgap of the participating semiconductors are usually different. Often, the potential discontinuities are present in both the conduction and valence band. As the composition changes with grown direction (z), we can add a supplementary "confining" potential term V_0 into the crystal Hamiltonian:

$$\left(\frac{\boldsymbol{p}^2}{2m^*(\vec{r})} + V(\vec{r}) + V_0 + W_{SO} \right) \Phi_{n,k}(\vec{r}) = E_{n,k} \Phi_{n,k}(\vec{r}) \tag{1.12}$$

The wavefunction Φ is no longer in Bloch form due to the lack of the potential periodicity in the growth direction. As the confinement potential is along one only direction (z), it is assumed that the carriers can move freely in the "in plane" directions (x-y plane) and can still be described in term of a Bloch wave:

$$\Phi_n(\vec{r}, k_{//}) = \exp\{i(k_x x + k_y y)\} \chi_n(z) \tag{1.13}$$

characterised by an energy dispersion relation:

$$E_n(k_{//}) = E_n + \frac{\hbar^2 (k_x^2 + k_y^2)}{2m_e} \tag{1.14}$$

$k_{//}$ is the wavevector in the x-y plane, $\chi_n(z)$ is the wavefunction component describing the behaviour in the z-direction. The enveloped function $\chi_n(z)$ with quantization energy E_n can be obtained as the solution of a one-dimension problem.

1.1.3 Quantum Wells

In this section we will discuss the quantum effects arising from the mono-dimensional confinement of an electron and a hole along the z-direction. In chapter III, we have studied the spin dynamics in GaAsN/GaAs quantum wells.

Quantum wells (QW) are formed in semiconductors by sandwiching a material of lower band gap in between two layers of a material with a larger band gap. A quasi two dimensional electron system can be realized, if the motion of the carriers is strongly confined in one dimension by a suitable potential difference on a length scale comparable to or smaller than the de Broglie wavelength of these particles.

Choosing z as the confinement direction with origin (z=0) at the well centre, and *L* as the well width, we describe the potential as being zero at the bottom of the well and V_0 in barrier. The electrons are characterised by their respective effective mass in the well (m_A^*) and in the barrier (m_B^*). The solution of the Schrödinger equation is carried out in the usual way for |z| > *L*/2, the barrier region and |z| < *L*/2, the well region. Due to the symmetry of the potential, the wave functions can have even or odd parity. The solution of Eq(1.12), using the Eq.(1.13) as the ansatz we obtain the following expressions:

$$\chi_n(z) = \begin{cases} Be^{\beta z} & for \quad z < -L/2 \\ A\begin{Bmatrix}\cos\\ \sin\end{Bmatrix}(\alpha z) & for \quad |z| < L/2 \\ Be^{-\beta z} & for \quad z > L/2 \end{cases} \tag{1.15}$$

$$\alpha = \sqrt{\frac{2m_A^*}{\hbar^2}E_n - (k_x^2 + k_y^2)}$$

$$\beta = \sqrt{\frac{2m_B^*}{\hbar^2}(V_0 - E_n) + (k_x^2 + k_y^2)}$$

where *A* and *B* as normalisation constants. The corresponding energy eigenvalues are then:

$$E_n(k_x, k_y) = \frac{\hbar^2}{2m_A^*}\left[\left(\frac{n\pi}{L}\right)^2 + k_x^2 + k_y^2\right] \qquad n=1,\ 2,\ 3\ldots \tag{1.16}$$

The wavefunction alternates between the cosine- and sine-type function in the well following the parity of *n*, whereas it has an evanescent character in the barrier.

As for the bulk materials, the valence band is of more complicated treatment than the conduction band. The approach is to add a confinement potential to the Kohn-Luttinger Hamiltonian. We can rebuild electron Hamiltonian in the QW with referring to Eq.(1.9): Firstly, the confinement potential term *V(z)* should be added into Hamiltonian; And the cubic term in Eq.(1.10), which proportional to $(\gamma_3^2 - \gamma_2^2)$, is rather small in most zinc blende semiconductors that we can omit it;

Finally we assume the Luttinger parameters are identical in QW and barriers. With those simplifications, the Hamiltonian of holes in QW becomes:

$$H_{QW} = \frac{\hbar^2}{2m_0}\left[(\gamma_1 + \frac{5}{2}\gamma_2)\nabla^2 - 2\gamma_2(\nabla \cdot \boldsymbol{J})^2\right] + V(z) \tag{1.17}$$

With the assumption that Schrödinger function is separable in the direction of quantization from the in-plane movement, the Hamiltonian for motion in z-direction can be simplified into the form:

$$H_z = \frac{\hbar^2}{2m_0}\left[(\gamma_1 + \frac{5}{2}\gamma_2) - 2\gamma_2 J_z^2\right]\left(\frac{\partial}{\partial z}\right)^2 + V(z) \tag{1.18}$$

Since the confinement energy is inversely proportional to the effective mass (1.16), the HH sub-band will be raised above the LH at the zone centre (if we neglect strain effects), as shown in Fig.1.3(a).

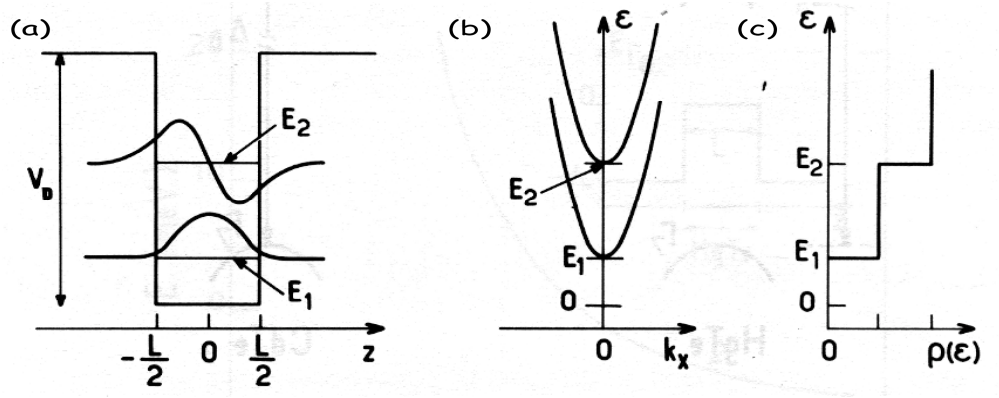

Fig.1.3 - *(a) The electron wavefunction (n=1, 2) in the confining potential of a quantum well; (b) the corresponding energy dispersion and (c) the density of states.*[1]

1.2 Optical orientation in zinc blende structures

We describe in this section the optical orientation process which is the fundamental mechanism used in this work for the investigation of the spin properties of conduction band electron in dilute nitride semiconductors.

1.2.1 Optical interband transition

When an electromagnetic wave interacts with a semiconductor whose band gap is inferior to the photon energy, the process of photon absorption obeys the energy and momentum conservations: a photon will transfer both its energy and its angular momentum to the photogenerated carriers. Therefore, upon absorption, by properly choosing the incident light polarisation (i.e. the photon angular momentum), the photogenerated carriers will be selected according to the value of their total angular momentum (***J***). This process, known under the name of optical orientation of carriers, is ruled by the optical selection rules in semiconductors, which will be detailed in the following. In the inverse process, the photon emission, the photon will have symmetrically imprinted in its polarisation state, the information of the angular momentum of the carriers which created it upon recombination.

For direct band-gap semiconductors such as GaAs, InAs, etc..., the lowest energy point in CB and highest point in VB share the same momentum (***k***), at the Γ-point (***k*** =0). Thus during the optical transition, the momentum conservation can be fulfilled without the participation of phonon, hence called direct interband transition.

Optical transition can be mathematically treated as a perturbation in quantum mechanics. In the single electron approximation, the Hamiltonian of an electron (H_{eR}) in the electromagnetic field can be written as:

$$H_{eR} = \frac{1}{m_0}\left[\boldsymbol{P} + \frac{eA(\boldsymbol{r},t)}{c}\right]^2 \tag{1.19}$$

where m_0 is electron mass, $\boldsymbol{P}$ is the momentum of the electron, e is electron charge, c is the speed of light and $A(\boldsymbol{r},t)$ is the electromagnetic wave vector. The latter can be written as

$$A(\boldsymbol{r},t) = A_0 a_0 \left\{\exp\left[i(\boldsymbol{q}\cdot\boldsymbol{r} - \omega t)\right] + \exp\left[-i(\boldsymbol{q}\cdot\boldsymbol{r} - \omega t)\right]\right\} \tag{1.20}$$

where $A_0 = \sqrt{\frac{\hbar}{2\varepsilon_0 \eta^2 V \omega}}$, η is the refractive index of the semiconductor, ε_0 is the dielectric constant, V is the volume, a_0 is polarisation vector, $\boldsymbol{q}$ is the wavevector of electromagnetic field. For direct interband transition, the limitation of the perturbation treatment to the first order is sufficient, allowing for the development of the interaction Hamiltonian to:

$$H_{eR} = \frac{e}{m_0 c} \boldsymbol{A} \cdot \boldsymbol{P} + \frac{e^2}{2 m_0 c} \boldsymbol{A}^2 \approx \frac{e}{m_0 c} \boldsymbol{A} \cdot \boldsymbol{P} \tag{1.21}$$

Moreover, the absorption and emission process can be respectively detailed as :

$$H_{eR} = H_{eR}^{+} + H_{eR}^{-} = \frac{eA_0}{m_0} \exp\left[-i(\boldsymbol{q} \cdot \boldsymbol{r} - \omega t)\right] a_0 \cdot \boldsymbol{p} + \frac{eA_0}{m_0} \exp\left[i(\boldsymbol{q} \cdot \boldsymbol{r} - \omega t)\right] a_0 \cdot \boldsymbol{p} \tag{1.22}$$

For the case considered here, we are concerned with the promotion of an electron from the valence band to the conduction band. By denoting the initial Bloch state of the electron as $\left|\psi_v\right\rangle$, and its final state as $\left|\psi_c\right\rangle$, and using the Fermi Golden rule, the transition probability reads

$$W_{v \to c} = \frac{2\pi}{\hbar} \left| \left\langle \psi_c \left| H_{eR}^{+} \right| \psi_v \right\rangle \right|^2 \delta(E_c - E_v - \hbar\omega) \tag{1.23}$$

Here

$$M_{cv} = \left\langle \boldsymbol{\psi}_c \left| H_{eR}^{+} \right| \boldsymbol{\psi}_v \right\rangle \tag{1.24}$$

is denoted the transition matrix element and its value, which takes into account the transition allowed by the symmetry of the wave functions and their relatives intensities, defines the optical selection rules. The Dirac δ function is responsible for assuring the energy conservation in the process.

1.2.2 Optical selection rules

The polarisation state of the incident light propagating along the z direction can be characterised by the polarisation vector $\boldsymbol{e}$. We can define the state of the incident light as being circularly polarised right or left if $e^{+} = \frac{1}{\sqrt{2}}(1, i, 0)$ or $e^{-} = \frac{1}{\sqrt{2}}(1, -i, 0)$ respectively. If the polarisation state is linear (along x for instance), it will be described by $e^{X} = (1,0,0)$. In a semiconductor, in the dipolar approximation, the optical matrix element M_{cv} for a transition between a valence band state and a conduction band state can be put in the form

$$M_{\mathrm{cv}} = \frac{1}{\sqrt{\Omega}} \left\langle u_{c,0} \left| \boldsymbol{e} \cdot \boldsymbol{p} \right| u_{v,0} \right\rangle \delta_{k,q} \tag{1.25}$$

where Ω represents the volume of the unit cell, ***e*** the polarisation vector of the incident electromagnetic wave, ***q*** is the wavevector of photon and ***p*** is the momentum operator. By introducing the Kane matrix

$$\Pi = \langle S|p_x|X\rangle = \langle S|p_y|Y\rangle = \langle S|p_z|Z\rangle \tag{1.26}$$

the matrix elements for the different polarisation states are calculated as:

$$\begin{aligned} M_{cv} &= \frac{1}{\sqrt{2}}\left\langle S\downarrow \left|P_x + iP_y\right|\Phi_{\frac{3}{2},-\frac{3}{2}}\right\rangle = \frac{1}{\sqrt{2}}\left\langle S\downarrow \left|P_x + iP_y\right|\frac{1}{\sqrt{2}}(X - iY)\downarrow\right\rangle \\ &= \frac{1}{\sqrt{2}}\left\langle S\left|P_x + iP_y\right|\frac{1}{\sqrt{2}}(X - iY)\right\rangle\langle\downarrow|\downarrow\rangle = \frac{1}{\sqrt{2}}\Pi \end{aligned} \tag{1.27}$$

and summarized in table 1.2.

	$\mathbf{e}//\mathrm{Ox}$	$\mathbf{e}//\mathrm{Oy}$	$\mathbf{e}//\mathrm{Oz}$
$\mathbf{q}//\mathrm{Oz}$	$\Pi/\sqrt{2}$	$\Pi/\sqrt{2}$	impossible
$\mathbf{q}//\mathrm{Ox}$	impossible	$\Pi/\sqrt{2}$	0
$\mathbf{q}//\mathrm{Oy}$	$\Pi/\sqrt{2}$	impossible	0
$\mathbf{q}//\mathrm{Oz}$	$\Pi/\sqrt{6}$	$\Pi/\sqrt{6}$	impossible
$\mathbf{q}//\mathrm{Ox}$	impossible	$\Pi/\sqrt{6}$	$\Pi\sqrt{2/3}$
$\mathbf{q}//\mathrm{Oy}$	$\Pi/\sqrt{2}$	impossible	$\Pi\sqrt{2/3}$

Table.1.2 - *The transition matrix elements for an electron excited from HH, LH or SO bands to the conduction band by the interaction with an electromagnetic wave of polarisation* ***e*** *and wavevector* ***q****.*[1]

In all the experiments described in the following chapters, the light propagates parallel to the growth direction of the samples (***q*** ||(O_z)). By taking into account the angular momentum conservation, the allowed optical transitions induced by a right (Σ^+) or left (Σ^-) circularly polarised light can be summarised as presented in Fig.1.4 for a direct gap zinc blende semiconductor such as GaAs at the zone centre. It is clear from Fig.1.4 that the excitation of the semiconductor with a circularly right polarised photon of energy $\hbar\omega = E_g$, selectively promotes 3 electrons of spin -1/2 for

an electron of spin +1/2 from the valence band to the conduction band. The electron polarisation degree, defined as $P_e=(n_+ - n_-)/(n_+ + n_-)$, is then at most P_e =50%. However, if the energy of the incident photon increases such that $\hbar\omega > E_g+\Delta_{so}$, transitions from split-off are allowed, and the total CB electron spin polarisation drops to zero. The creation of a spin polarised electron population in zinc blende semiconductor imposes a limit to the energy of the exciting photon:

$$E_g < \hbar\omega < E_g+\Delta_{so} . \qquad (1.28)$$

As previously noted, Δ_{so}= 341 meV in GaAs[1]. The selection rules apply symmetrically to the reverse process as well, i.e. the radiative recombination of the electron from the CB to the VB.

The determination of the selection rules in the case of 2D Quantum Wells structures can be carried out in a similar manner starting from the wavefunctions defined in the framework of the envelope function approximation. The results lead to the same transition probabilities as presented in table 1.2. However, the lift of the degeneracy at the zone centre ($k_{||}$=0) between the HH and LH bands, allows for the selective excitation of only +1/2 or -1/2 CB electron spin, thus increasing the electron spin polarisation up to P_e =100%.

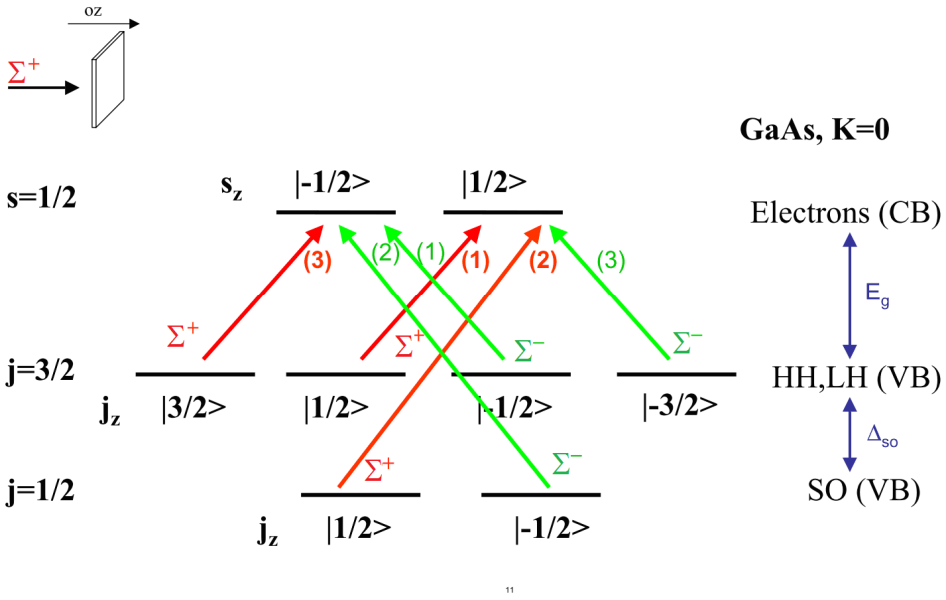

Fig.1.4 - *Optical selection rule in direct gap unstrained bulk III-V semiconductors*

1.3 Main spin relaxation mechanisms

To conclude this chapter, we will synthetically present the main spin relaxation mechanisms of carriers in semiconductors. The spin relaxation is the process that brings back an imbalanced non-equilibrium spin population to the initial equilibrium condition. It is the central issue in the spin physics of semiconductors.

1.3.1 Elliott-Yafet mechanism

Elliot first suggested[4] that electron spin relaxation occurs via momentum scattering. The mechanism is linked to the fact that via the spin-orbit interaction the electron wavefunctions are not pure spin states for $\boldsymbol{k}\neq 0$. Therefore, upon a scattering event which charges the electron momentum from k to k' can lead as well to a spin relaxation [5]. The scattering induced spin relaxation process is schematically shown in fig.1.5. The mechanism is dominant in small-gap semiconductors with large spin-orbit splitting. [5]

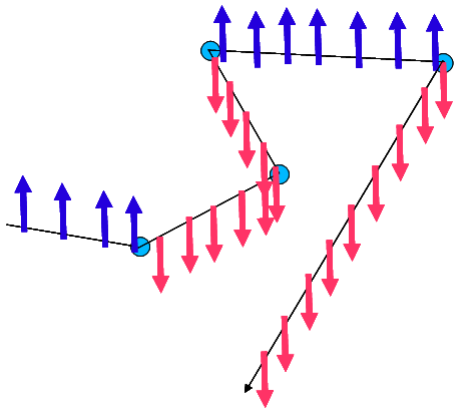

Fig.1.5 - *Spin relaxation by scattering in Elliott-Yafet mechanism*

1.3.2 D'yakonov-Perel mechanism

In non centro-symmetric semiconductors (such as GaAs), the spin orbit interaction lifts the conduction band spin degeneracy. This spin-orbit related effect was firstly proposed by Dresselhaus[9], which pointed out that the Hamiltonian associated to the interaction can be cast in the form

$$H_{DP} = \frac{\hbar}{2}\boldsymbol{\sigma}\cdot\boldsymbol{\Omega}(\boldsymbol{k}) \tag{1.29}$$

which is formally identical to the to the expression of the interaction of an electron spin with a magnetic field (an "effective" field) present in the crystal. The spin vector precesses therefore at the frequency $\boldsymbol{\Omega}(\mathbf{k})$ which is a function of the electron momentum. At each collision, the crystal momentum ***k*** change causes the variation of the effective magnetic field strength and therefore of the precession frequency $\boldsymbol{\Omega}(\mathbf{k})$. The spin relaxation time τ_s between two collisions is found to be proportional to[7]:

$$\frac{\mathbf{1}}{\boldsymbol{\tau}_{\mathbf{S}}} \propto \boldsymbol{\Omega}^2 \boldsymbol{\tau}_p \tag{1.30}$$

Contrary to the Elliott-Yafet mechanism, an increased scattering rate decreases the effectiveness of the spin relaxation rate. This process is schematically shown in Fig.1.6.

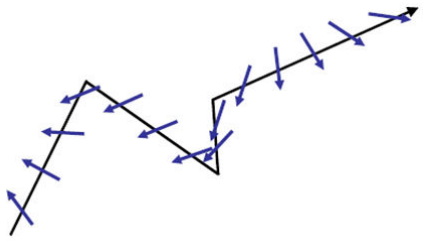

Fig.1.6 - *Spin relaxation process in D'yakonov-Perel mechanism*

The Elliott-Yafet and D'yakonov-Perel mechanisms usually coexist in systems lacking inversion symmetry, their relative strengths depending on many factors. In general, the D'yakonov-Perel mechanism becomes more relevant with increasing band-gap and temperature. This mechanism often dominates in III-V semiconductors and 2D structures.

1.3.3 Bir-Aronov-Pikus Mechanism

Bir et al. (1975)[6] proposed first this spin relaxation mechanism in p-type semiconductors. This phenomenon appears during scattering processes including an electron and a hole. The two particles can in this case simultaneously relax their spin via the exchange interaction. The efficiency of this mechanism directly depends on the probability of electron-hole scattering and is becomes dominant in heavily p-doped semiconductors at low temperatures.[5, 7]

1.3.4 Hyperfine-interaction Mechanism

The Hyperfine spin relaxation mechanism finds its origin from the interaction between the magnetic momentum of nuclei and electrons. The electron spin can interact with the spins of the lattice nuclei, which being normally randomly oriented, provide a randomly varying effective magnetic field interacting on the electron spin. Usually the corresponding relaxation rate is rather weak compared to other mechanism, but it may become important for localized electrons, when other mechanisms associated with electron motion are quenched. In semiconductor heterostructures, this mechanism is also responsible for spin dephasing of localized or confined electron spins [5, 7, 8].

References:

[1]. G. Bastard, *Wave mechanics applied to semiconductor heterostructures* (1990).

[2]. P. Yu and M. Cardona, *Fundamentals of semiconductors*, Springer (1995).

[3]. Q. H. F. Vrehen, *Interband magneto-optical absorption in gallium arsenide*, J Phys Chem Solids, **29**: 129-141, (1968).

[4]. R. J. Elliott, *Theory of the effect of spin-orbit coupling on magnetic resonance in some semiconductors*, Physical Review, **96**: 266, (1954).

[5]. I. Zutic, J. Fabian and S. Das Sarma, *Spintronics: Fundamentals and applications*, Reviews of Modern Physics, **76**: 323-410, (2004).

[6]. G. L. Bir, A. G. Aronov and G. E. Pikus, *Spin relaxation of electrons scattered by holes*, Zhurnal Eksperimentalnoi I Teoreticheskoi Fiziki*,* **69**: 1382-1397, (1975).

[7]. M. I. Dyakonov, *Introduction to spin physics in semiconductors*, Physica E-Low-Dimensional Systems & Nanostructures, **35**: 246-250, (2006).

[8]. M. I. Dyakonov, *Spin physics in semiconductors*, Springer (2008).

[9]. G. Dresselhaus, *Spin-Orbit Coupling Effects in Zinc Blende Structures*, Phys. Rev., **100**: 580 (1955).

Chapter 2

Experimental set-ups and samples

This chapter is devoted to the description of the experimental devices and the semiconductor samples used in this work.

In the first part we will present the principles of the Polarisation- and Time-Resolved Photoluminescence with a description of the experimental set-up including the excitation laser source, the ultra fast detector (Streak Camera) and the cryogenic system. A description of the set-up used for time integrated photoluminescence will follow.

In the second part we will give a brief introduction to the photoconductivity technique used to demonstrate the spin dependent conductivity effect in dilute nitride semiconductors as described in chapter 4.

Finally, we will describe the Optically Detected Magnetic Resonance set-up used in the framework of our collaboration with the group of Prof. W. Chen of the Linköping University, Sweden.

A description of the sample structures used in this work will follow in the end of this chapter.

2.1 Time resolved photoluminescence spectroscopy

The principle of Time Resolved Photoluminescence (TRPL) experimental setup is shown in Fig.2.1. The light from a mode-locked Ti-Sapphire laser, whose polarisation can be controlled by optical waveplate elements, is used to excite the samples. The luminescence signal emitted by the sample is then collimated, and focussed onto the entrance slits of the monochromator with its corresponding polarisation being screened out. The light, spectrally dispersed by the monochromator grating, is then sent to the ultrafast detector (Streak Camera), synchronised with the laser pulse, and is finally recorded by a CCD camera. The different elements composing the experimental set-up will be detailed below.

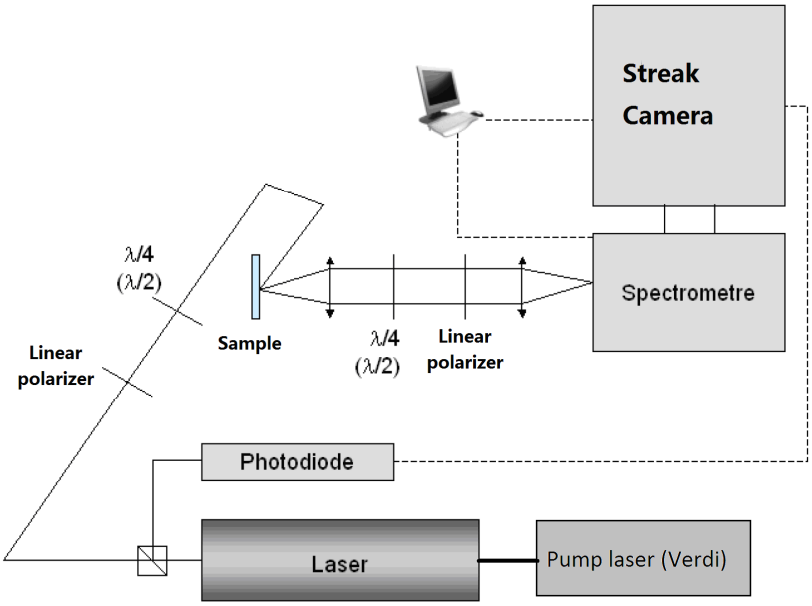

Fig 2.1 - *Time Resolved Photoluminescence measurement set-up*

2.1.1 Excitation source

The main excitation source is a mode-locked Titanium-Sapphire (Ti:Sa) laser pumped by a solid-state, single-frequency, continuous wave 532 nm laser with power levels up to 10W (VERDI-V10). The pump laser uses a Nd:YVO_4 (Neodymium Doped Yttrium Orthvanadate crystal) as amplifying medium, characterised by an emission wavelength of 1064 nm. The Nd:YVO_4 is in turn itself optically pumped by two semiconductor lasers and placed in a mono-mode ring cavity containing an LBO doubling crystal which produces the 532 nm wavelength radiation used to pump

the Ti:Sa Laser. The stability of the VERDI output power is then guaranteed by feedback circuitry on the measured crystal temperature and output power.

The Ti:Sa laser active medium is a Titanium ion doped sapphire crystal (Ti:Al_2O_3). This laser has the characteristics of both being wavelength tuneable and working under pulsed operation. The pulsing operation, achieved by a mode-locking technique (see below), can produce two different pulse widths at a frequency of 80 MHz: (1) In femtosecond mode, it generates a 100 fs wide pulse; (2) In picosecond mode, the duration of each pulse is about 1.5 ps. We have chosen to use the picosecond operation for this work as the time resolution offered by this mode is sufficient to the analysis of the dynamical phenomenon studied.

The mode-locking technique, used to achieved pulse operation, exploits the Kerr effect in the Ti:Sa crystal[1]. Owing to the Kerr effect, when a strong beam passes through the Ti:Sa crystal, it experiences a variation in index of refraction which is proportional to the local irradiance of the light making the crystal act like a converging lens. This refractive index variation is responsible for the nonlinear optical effects of self-focusing and self-phase modulation. The result is a "locking" of the modes of the cavity which favours the pulsed operation. In order to start the pulsed operation, an acoustic-optical modulator synchronised with the laser pulsed is placed in the cavity. As the beam travel along the cavity, the dispersion of the group velocity needs to be compensated to preserve the desired pulsed operation. This compensation is obtained by a Gires–Tournois etalon[2] which provide the necessary wavelength dispersion variation to "re-phase" the different modes composing the laser pulse. Furthermore, the lasing wavelength is selected by acting on a tuneable narrow bandpass birefringence optical filter (Lyot-filter). The main characteristics of the Ti:Sa laser are summarised in table 2.1.

Repetition Frequency	***Spectral range***	***Average power***	***Pulse energy***	***Pulse duration***	***Spectral width***
80 MHz	680-990 nm	0.4-2 W	5-25 nJ	1.2-1.8 ps	≈1.2 meV

Table 2.1 - *Ti:Sa laser main characteristics*

2.1.2 Streak camera detection

The ultrafast detection required to temporally resolve the sample photoluminescence is obtained by the use of a Streak Camera. Its operating principle is sketched in figure 2.2. The light

signal, spectrally dispersed by the monochromator and focussed on the camera entrance slit, is imaged onto the camera photocathode by a system of lenses. The light incident onto the photocathode is proportionally converted into a photocurrent which is then accelerated and amplified respectively by a pair of electrodes and a Micro Channel Plate (MCP) photomultiplier to finally hit a phosphorous screen whose luminescence is recorded by a Charge Coupled Device (CCD) camera. The signal passing through the accelerating tube experiences also a vertical deflection proportional to the arrival time of the light onto the photocathode. This deflection is assured by a high electrical tension applied by the sweep electrodes synchronised with laser pulse by mean of a fast photodiode. The image on the phosphor screen shows therefore the earlier pulse at the upper area, and the latter pulses in the lower area. During all the process, the intensity of the pulse is proportionally amplified, and wavelength of signal is aligned horizontally. The image retrieved by the CCD camera contains therefore the information on the spectral and temporal distribution of the light signal (respectively represented by the vertical and horizontal axis) as well as its intensity encoded in a colour scale as shown as in Fig.2.3.

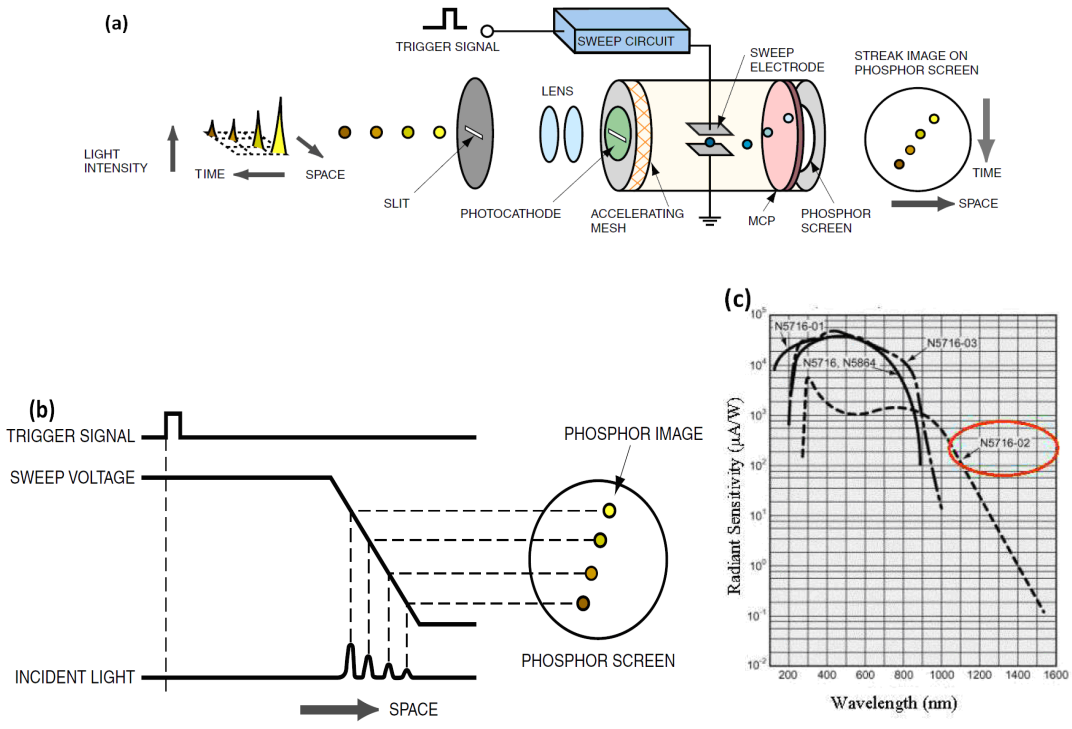

Fig.2.2 - *Operating Principle of the Streak Tube (a) and sketch of the sweeping mechanism responsible for the time resolution (b); The spectral sensitivity of the S1 photocathode is reported in (c).*

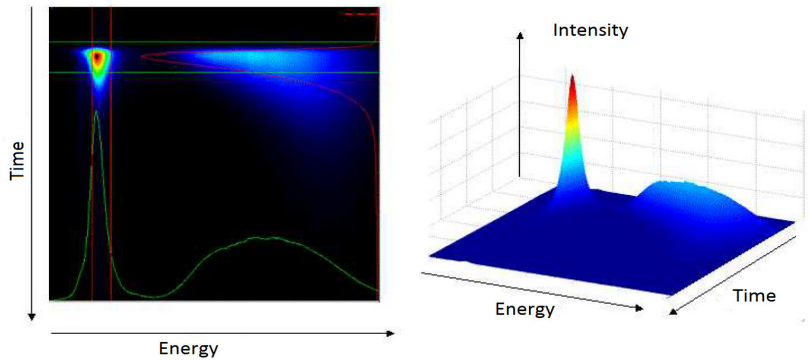

Fig.2.3 - *Example of a streak camera image on time range 4 and 80 grooves/mm grating*

2.1.3 Spectral and temporal resolution

The spectral resolution is obtained by a Jobin-Yvon Triax 320 monochromator, placed before the streak camera, and equipped with 3 gratings. Their characteristics are presented in the Table 2.2.

Grating (grooves/mm)	***Blazing Wavelength (nm)***	***Spectral width(nm)***	***Dispersion(nm/mm)***	***Resolution (nm)***
80	870	188.0	39.6	0.6
300	1000	46.2	10.56	0.3
600	400-1300	22.2	5.28	0.1

Table.2.2 - *The characteristics of the Jobin-Yvon Triax 320 monochromator. The spectral resolution values are given for a 200 µm and 80 µm width of the entrance and exit slit respectively.*

The intrinsic time resolution of streak camera is about 2ps. However, the effective time resolution depends on the wavelength dispersion of monochromator. A larger dispersion will produce a larger optical path difference between the portion of light travelling respectively on the side and on the central optical axis of the grating. This difference generates therefore a temporal dispersion which can be minimised by placing a vertical slit inside the monochromator to reduce the lateral dimension of the beam.

The streak camera can be operated in 4 different time ranges, whose characteristics are presented in Table 2.3.

Time range index	Temporal span (ps)	Time resolution (ps) using the 80 grooves/mm grating
1	157	5
2	809	8
3	1542	12
4	2263	17

Table 2.3 - *Temporal mode of streak camera*

2.1.4 Polarisation resolution

In optical orientation experiments, the analysis of the PL polarisation allows for the determination of the spin polarisation of the photogenerated carriers after the sample has been excited with a definite light polarisation. The exciting light polarisation state can be adjusted from linear (Σ^X or Σ^Y) to elliptical and circular (Σ^+ or Σ^-) by using a Glan-Taylor polarising cube followed by a quarter wave plate whose neutral axis direction can be rotated with respect to Glan-Taylor exit linear polarisation axis. The incident laser beam is then focussed onto the sample surface with ≈100 µm diameter spot. The polarisation analysis of the PL emitted by the sample is realised by the interposition of a quarter wave plate (for circular polarisation) or a half wave plate (for linear polarisation) followed by a Glan-Taylor polarising cube on the collimated beam in the optical collection system. By choosing the appropriate orientation of the birefringent the co- and counter-polarised components of the PL with respect to excitation light polarisation can be filtered and focused onto the entrance slit of the monochromator for the detection.

The circular polarisation degree is then defined as:

$$P_C = \frac{I^+ - I^-}{I^+ + I^-} \tag{2.1}$$

where I^+ (I^-) represents the PL intensity co-polarised (counter-polarised) with respect to the circular polarisation of excitation. The linear polarisation degree is likewise defined using the linearly polarised components of the PL.

2.2 Time integrated photoluminescence spectroscopy

One of the main feature of the Spin Dependent Recombination (see chapter 3), is the much stronger total PL emission under circularly polarised light excitation with respect to a linear one. No PL time or polarisation resolution is needed for this measurement. In order to speed-up the data acquisition the detection ensemble (Monochromator and Streak Camera) has been replaced by a silicon photodiode (Thorlabs FDS1010) coupled to a long pass filter in order to suppress all contribution from both the laser scattered light and the substrate/buffer layer luminescence. The excitation light is mechanically chopped and the photodiode signal synchronously detected with a lock-in amplifier (SRS 5208).

2.3 Photoconductivity measurements

The scheme of photoconductivity measurement is presented in Fig.2.4 (a). A source meter supplies a constant voltage in the range 0<V<12 Volts between the sample electrodes and a 10 kΩ resistor (R_s) placed in series with the sample. R_s is chosen several orders of magnitude smaller than sample resistance to assure a negligible influence of the voltage drop across its terminals. The excitation light, focussed in between two Ag electrodes (see Fig.2.4 b) is provided by the Ti:Sa laser used either in the CW operation or in the mode-locked regime. As for the time integrated PL, the excitation laser light is modulated by a mechanical chopper and the sample photocurrent change as a function of the excitation light polarisation is synchronously detected by a lock-in amplifier by measuring the voltage drop at the R_s terminals. The alternation of polarisation of excitation is obtained by manually turning the quarter plate in front of the Glan-Taylor in the excitation light path. The use of a light modulation technique has moreover the advantage of suppressing the persistent photoconductivity[3] which does not participate to the SDR process. A sketch of the sample is reported in Fig.2.4(b). Two silver electrodes lay approximately 1 mm apart on the sample surface. We have carefully masked the electrodes in order to avoid any contact related to photovoltaic effects.

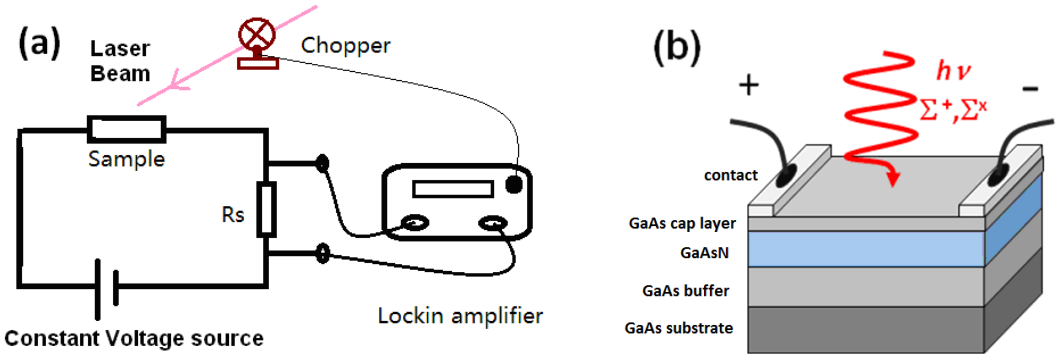

Fig.2.4 - *(a) Photoconductivity measurement setup with lock-in amplifier; (b) Schematic view of the GaAsN structure used for the Spin Dependent Photo Conductivity (SDPC) measurement.*

2.4 Cryogenics and magnetic field

2.4.1 Cryogenics

Although most of the measurements presented here were performed at room temperature, some measurement required the cooling down of the sample to explore the temperature effects on the SDR phenomenon. It has been possible to adjust the sample temperature from 10K to 300K by placing it on the cold finger of a closed cycle Helium Cryogenerator.

2.4.2 Magnetic field

Some of the experimental presented here needed the use of magnetic field in Voigt geometry (magnetic field parallel to the sample plane and perpendicular to the excitation light wave vector). To produce a quasi-homogeneous magnetic field in the range of 200mT to 1T, we have used two permanent magnets ≈650mT each in Helmholtz configuration. The mutual distance of the magnets can be varied in order to tailor the magnetic field strength applied to the sample. For smaller magnetic field (0mT to 100mT), a self-made electromagnet is used allowing for the continuous variation of the applied magnetic field by varying the current intensity flowing into it.

2.5 Optically Detected Magnetic Resonance

The Optically Detected Magnetic Resonance (ODMR)[4] is a technique combining optical measurements (fluorescence, phosphorescence, absorption) with electron spin resonance spectroscopy (ESR). The information obtained is essentially the same as ESR whereas the essential

difference is related to the detection mechanism: the modification of the PL emitted by the sample under magnetic field and microwave radiation (the ESR radiation) is probed by optical detection, PL in our case. The particular value of the radiation frequency or magnetic field under which a PL modification is noticed (resonance conditions), are used to trace the nature of the atomic system to whom the electron are bound (impurity, defect, etc…). The interest of the ODMR (and ESR) technique resides on the fact that the resonance condition depends not only on the chemical nature of the atom under consideration but also on its mass (isotope) and environment (type of defect for example). This technique has been employed in this work in collaboration with Weimin Chen (University of Linköping, Sweden) to probe the nature of the paramagnetic centres responsible for the SDR effect (see chapter 3). A brief description of the ODMR principles follows hereafter.

In quantum mechanical description, the angular momentum of the electron spin is quantized along the externally applied magnetic field, giving rise to two possible quantum states characterised by the spin quantum number *s*= -1/2, +1/2. This splits the originally degenerate energy level into two sublevels, the Zeeman levels, whose energy separation is proportional to field strength. If the energy of microwave photon sent to the sample coincides with the Zeeman energy separation, a spin resonance transition can occur (ESR transition). The spin Hamiltonian of the atom plus electron system is written as:

$$H = \mu_B g \boldsymbol{B} \cdot \boldsymbol{S} + A \boldsymbol{S} \cdot \boldsymbol{I} \tag{2.2}$$

Here μ_B is the Bohr Magneton, $\boldsymbol{S}$ is the electronic spin, $\boldsymbol{I}$ represent nuclear spin, g is the Landé *g*-factor and A is the hyperfine parameter. The first term of the Hamiltonian describes the Zeeman energy splitting of a single electron whereas the second term is hyperfine interaction energy between electron spins and nuclear spins. The nuclear Zeeman term and other higher order effect are omitted in the description. Fig.2.5 displays a simple system in which S=1/2 and I=1/2. By sweeping the magnetic field under a microwave radiation of constant frequency, it is possible to identify the resonances in the microwave spectrum (in the ESR case) which are characteristics of the atomic species considered and its environment.

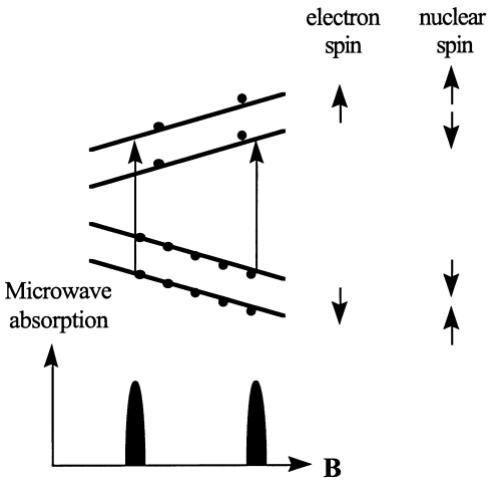

Fig.2.5 - *Sketch of the ERS resonances due to the Zeeman term and the Hyperfine structure in the case S=1/2, I=1/2. (Cited from reference[4])*

In the case of ODMR, the microwave transition will open up otherwise closed recombination paths on the atomic defect for the conduction band electrons. This will appear as a drop on the band to band luminescence intensity used as the optical detection of the ESR resonances.

The basic scheme of the ODMR set-up used in this work is shown in Fig.2.6. A microwave cavity is placed in between the pole of a variable magnet. A modulated microwave source connected with the cavity provides the electromagnetic energy used to produce the electron resonance transitions. The corresponding modulation of the PL induced by a laser excitation is synchronously detected with by a cooled Ge detector with a proper selection of optical filters and connected to a lock-in amplifier.

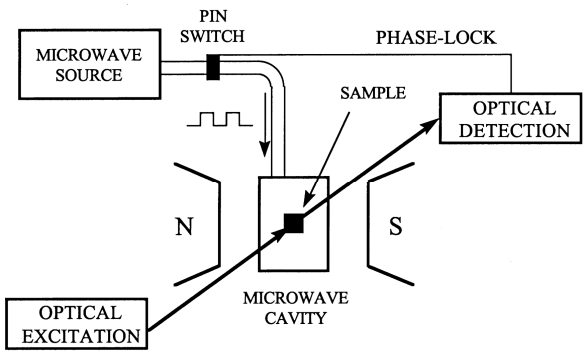

Fig.2.6 - *A simple scheme of the ODMR set-up. (Cited from reference[4])*

2.6 Sample description

2.6.1 GaAsN epilayers

The samples under study (Table.2.4) consist of nominally undoped dilute nitride GaAsN semiconductor epilayers of different N content and thickness, grown by molecular beam epitaxy on a (001) semi-insulating GaAs substrate, after a 400nm GaAs buffer layers. The growth is then terminated with a 10nm GaAs cap layer. A series of Si doped samples with different doping concentrations has been as well grown specifically for the photoconductivity experiments.

Sample whose number begins with "7AM" are grown in exactly the same conditions sequentially by J.C. Harmand at the Laboratory of Photonics and Nanostructure (LPN), Paris, France. To avoid poor structural quality caused by large strain, thinner layer thickness is adopted for higher N content samples. Sample 3026 was provided by the A.F.Ioffe Physico-Technical Institute of St.Petersburg, Russia. Differently for the other samples, sample 3026 has undergone a post-growth rapid thermal annealing (RTA) at 700-720 °C for 3 minutes.

2.6.2 GaAsN quantum wells

We have also studied a series of GaAsN/GaAs multiple quantum wells samples (7 wells per sample) with 3,5,7,9 nm well width respectively with constant nitrogen content N=1.6%. All the quantum wells were grown by molecular beam Epitaxy (MBE) on a (001)-oriented semi-insulating or n^+ GaAs substrate, and were capped by a 250 nm thick GaAs layer. The quantum wells are sandwiched between 20.2 nm GaAs barriers. These samples are provided by Prof C.W.Tu from department of Electrical and Computer Engineering in university of California,USA.

Name of Samples	Thickness of GaAsN layer(μm)	N%	Si doping
Series '7AM'			
7AM66	0.1	0.05	None
7AM67	0.1	0.15	None
7AM68	0.1	0.74	None
7AM69	0.05	1.43	None
7AM70	0.1	1.03	None
7AM71	0.05	2.6	None
7AM72	0.05	5.1	None
7AM73	0.05	1.9	None
7AM74	0.05	3.5	None
7AM75	0.05	2	1.00E+17
7AM76	0.05	2	5.00E+17
7AM77	0.05	2.1	2.00E+18
others			
79M29	*0.1*	*0.76*	*None*
3026 (RTA)	*0.1*	*2.1*	*None*

Table 2.4 - *Description of epilayer samples used in this work*

References:

[1]. C.Rullière, *Femtosecond Laser Pulses*, Principle and Experiments. Springer, (1998).

[2]. F. Gyres, P. Tournoi, *Interféromètre utilisable d'impulsions lumineuses modulés en fréquence*. C. R. Acad. Sc. Paris, 6112, (1964).

[3]. X. Z. Dang, C. D. Wang, E. T. Yu, K. S. Boutros and J. M. Redwing. *Persistent photoconductivity and defect levels in n-type AlGaN/GaN heterostructures*. Applied Physics Letters, **72**: 2745-2747, (1998).

[4]. W. M. Chen. *Applications of optically detected magnetic resonance in semiconductor layered structures.* Thin Solid Films, **364**: 45-52, (2000)

Chapter 3

Spin dependent recombination in GaAsN: Photoluminescence measurements

The dilute III-V nitride semiconductors, have stimulated a lot of interests after the discovery of their remarkable properties[1]. The incorporation of even a tiny fraction of nitrogen into GaAs or InGaAs matrix dramatically perturbs the band structure. Due to their widely adjustable band-gap, the dilute nitride semiconductors are potentially interesting for a wide range of applications, such as infrared lasers[2-7] , detectors[8] or high efficiency solar cells[9-11], etc.

However, the incorporation of N atoms as well as the low growth temperature also induces the creation of lots of defects in the lattice. Many applications are thus limited by the low quantum efficiency of (In)GaAsN structures caused by the efficient nonradiative recombination through defects. In the work presented here, we show that the control of these defects can be an advantage for potential spintronic applications. In particular, we demonstrate that dilute nitride structures can be used as efficient spin filters at room temperature.

In this chapter, we first present the experimental results related to the band gap variation as a function of N content and temperature. We also give a review on the prevalent band structure theories for GaAsN. Then, we present our experimental results demonstrating the spin dependent recombination in GaAsN investigated by photoluminescence spectroscopy. The model used to describe these properties will be afterwards discussed in detail. In conclusion, the nature of the defects responsible for the spin dependent recombination effect is revealed and analyzed by Optically Detected Magnetic Resonance (ODMR) experiments.

3.1 GaAsN Band Structure

In this part, we briefly review the experimental results on the GaAsN band gap variation as a function of nitrogen content and sample temperature, and the band structure theory used to explain the experimental results.

3.1.1 Band gap variation as a function of nitrogen content

Although the band gap of GaN is quite large, it's well known that the incorporation of a small quantity of nitrogen in GaAs largely reduces the band gap energy, see Fig.3.1(a,b). Experimentally, the band gap shrinks ≈100-200 meV by every 1% nitrogen introduced, see Fig.3.1(b). This makes dilute III-V nitride material good candidates for 900 – 1500 nm optical telecommunication applications[12, 13].

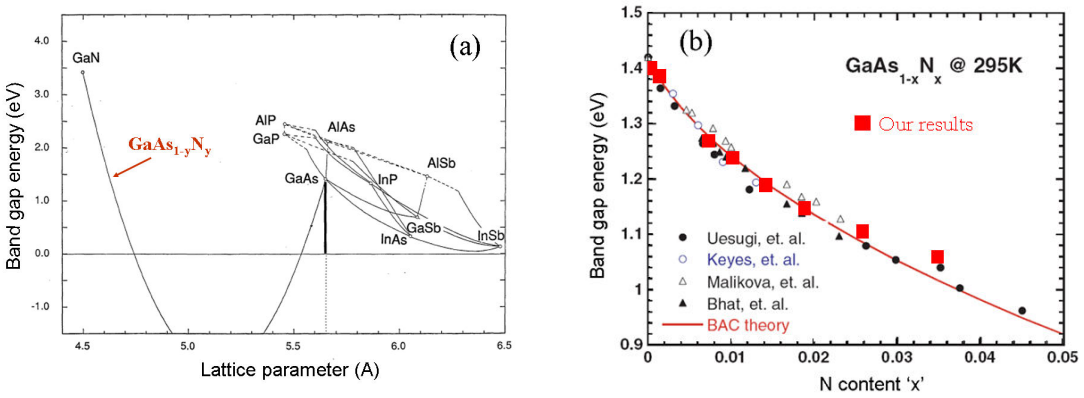

Fig.3.1 - *(a) Band gap evolution as a function of lattice parameter for main binary and ternary III-V group semiconductors. (According to Kondow et al.[12]) (b) $GaAs_{1-x}N_x$ band gap variation as a function of N content (x) in $GaAs_{1-x}N_x$. The red squares are our results extracted from photoluminescence. The red curve corresponds to a fit using the Band Anti-Crossing (BAC) model[14] .*

3.1.2 Band gap variation as a function of temperature

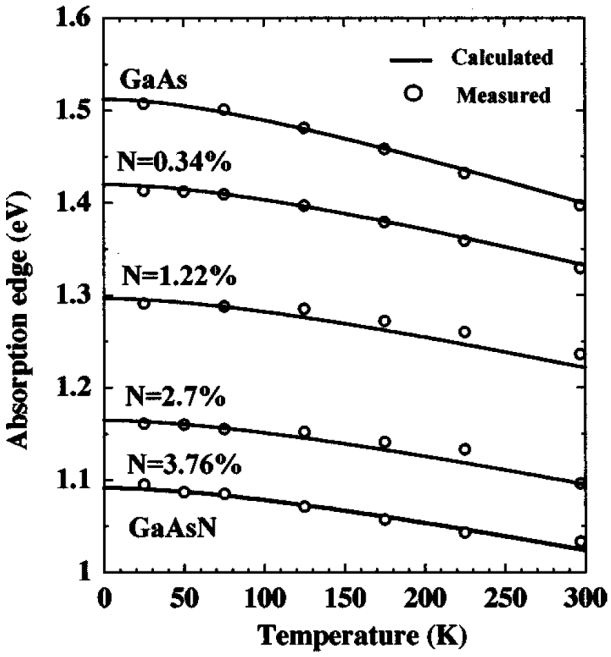

Fig.3.2 - *Temperature dependence of the absorption edge of GaAs and GaAsN alloys measured for different N compositions. The open circles are experimental values and solid lines are the result of the calculation based on two-level BAC model for the respective N compositions.*[15]

Fig.3.2 shows the temperature dependence of the absorption edges of GaAs and several $GaAs_{1-x}N_x$ samples with different N compositions [N] = 0.34%, 1.22%, 2.7%, and 3.76%. Compared to GaAs, GaAsN shows red-shift as the temperature increases and the red-shift decreases when the N content increases. [15]

3.1.3 Conduction band states of GaAsN

In GaAs structures, the introduction of a small percentage of nitrogen, strongly modifies the conduction band (CB) whereas the valence band is almost unmodified[14]. Recently, several models were proposed for describing the remarkable properties of dilute nitride semiconductors. In 1999, Shan *et al.* proposed the Band Anti-Crossing (BAC) model[14]. According to this model, as the N incorporation of a few N into GaAs introduces a localized level (E_N) in the CB, the interaction between E_N and the extended CB states causes band repulsion, which leads to a splitting of conduction band into two subbands E_+ and E_- , resulting in the shrinkage of the band gap as schematically shown in Fig.3.3 [16].

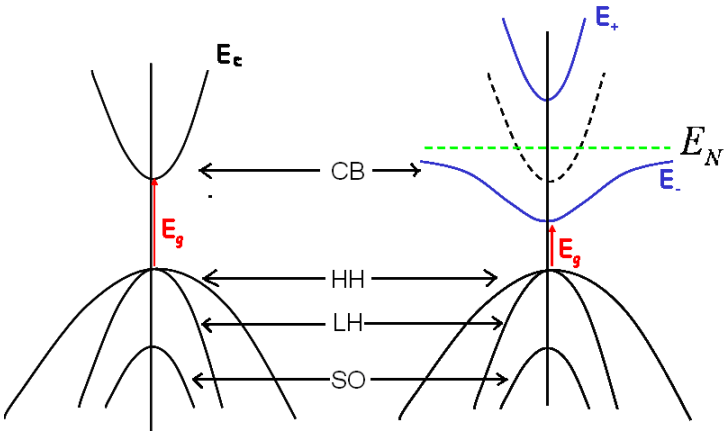

Fig.3.3 - *Schematic diagram of the band gap reduction according to the Band Anti-Crossing model*[16]. *The diagram on the left-hand side is a sketch of the band structure of undoped GaAs, where* E_g *represents the band gap; On the right-hand side, the band structure of dilute nitride GaAsN is presented, where* E_N *(green dashed line) are the localized states induced by N incorporation.*

In the BAC theory, the interaction between localized level and CB is treated in the framework of a strong coupling effect, and the eigenvalues of the energy level of CB can be obtained by solving [17]:

$$\begin{vmatrix} E_N - E & V_{Nc} \\ V_{Nc} & E_c + \dfrac{\hbar^2 k^2}{2m_c^*} - E \end{vmatrix} = 0 \qquad (3.1)$$

where E_c is the energy of the GaAs conduction band relative to the top of the valence band, V_{Nc} is the potential of the interaction between E_N and E_c (see Fig.3.3), m_c^* is the electron effective mass. By solving Eq(3.1), the new energy eigenvalues can be calculated:

$$E_{\pm} = \frac{E_N + E_c}{2} \pm \sqrt{\left(\frac{E_N - E_c}{2}\right)^2 + V_{Nc}^2} \qquad (3.2)$$

E_- yields now the new band gap energy. V_{Nc} is dependent on nitrogen content (x) and can be empirically expressed as[18]:

$$V_{Nc} = Cx^{1/2} \qquad (3.3)$$

where C is a constant.

The calculation results based on Eq(3.2) are shown in Fig.3.4(a). The tendency of a decrease of E_- as x increases is clear. Fig.3.4 (b) shows the CB dispersion calculated using the two-level BAC model,

the band-anticrossing interaction not only reduces the energy gap but also leads to an increased electron effective mass at the conduction band minimum, and to a strongly nonparabolic CB dispersion. Likewise, the E_N level has a weaker dependence on temperature than the GaAs E_c level, which explains the weaker temperature dependence of GaAsN compared to GaAs[15], in agreement with the experimental result presented in Fig.3.2.

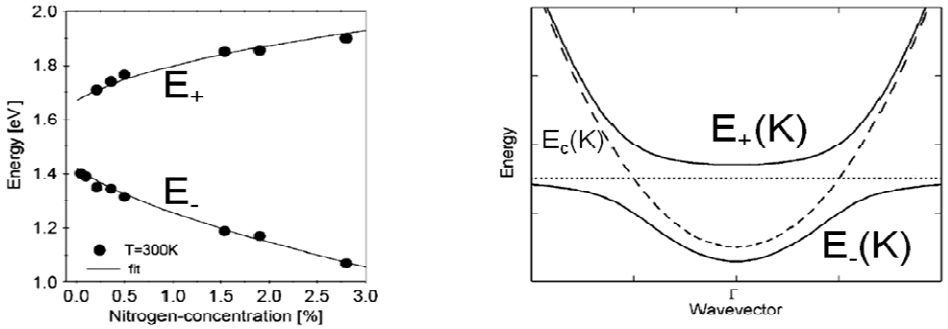

Fig.3.4 - *(a) The E_- and E_+ data obtained by fitting the photoreflectivity spectra of $GaAs_{1-x}N_x$. The solid lines are a fit to the two-level BAC model of Eq(3.2) [19]. (b) Conduction band dispersion calculated using the two-level Band-AntiCrossing model (solid line). Dashed line: host matrix conduction band dispersion; Dotted line: N resonant defect energy level.*

Although the BAC model is simple and empirical, this model gives a good agreement with the giant bowing of band gap as a function of N content (see Fig.3.1(b)), the increase of effective mass of electrons in the centre of Brillouin zone[20, 21], and the band gap energy dependence on temperature[15] (see Fig.3.2). But the two-level BAC model also has some limitations: (1) It significantly underestimates the effective mass in $GaAs_{1-x}N_x$ for x>1%[21-24]; And (2) it fails to explain the unexpected large gyromagnetic ratio and its non-monotonic variation in $GaAs_{1-x}N_x$ with x [25]; (3) The two-level BAC model has one further significant failing, giving an uncorrect dispersion for the lower (E_-) band at large wavevector k.

More recent models (Anderson many-impurity model[26], empirical pseudopotential model[27, 28] and tight-binding calculations[29]) tried more microscopic approaches which are the key to the improved predictions and to understanding of the details of the band structure of dilute nitride semiconductors. Fig.3.5 shows, for instance, the band structure obtained by "Linear Combination of Isolated Nitrogen States (LCINS)" calculation which is close to the many-impurity Anderson model which includes the coupling between different energy bands.

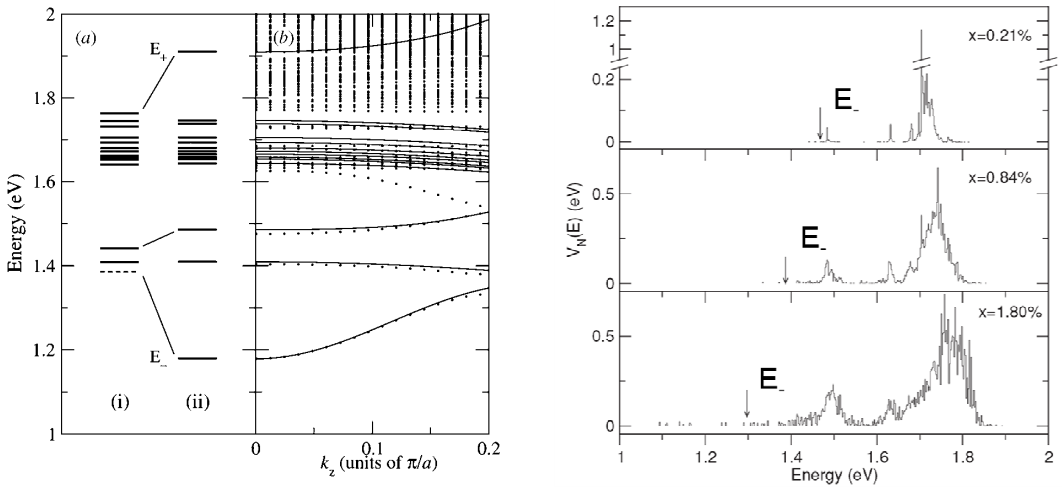

Fig.3.5 - *(a) Calculated N cluster-state energies E_N and CB-edge energy in a $GaAs_{0.974}N_{0.026}$ supercell (i) before and (ii) after inclusion of the interaction with the CB-edge. (b) Band dispersion obtained by tight-banding (dots) and LCINS methods (solid lines).(c) Calculated distribution of N cluster state energies, weighted by their interactions, with the conduction band edge state for three bulk $GaAs_{1-x}N_x$ compositions, with x = 0.21%, 0.84% and 1.80%, respectively. The vertical downward arrow in each panel shows the calculated position of the $GaAs_{1-x}N_x$ CB-edge E_-* [30].

3.1.4 Valence band states in GaAsN

Due to the lattice mismatch, the growth of GaAsN on a GaAs substrate introduces a biaxial tensile strain, which lifts the degeneracy at the centre of the Brillouin zone between Heavy-Holes (HH) and Light-Holes (LH) in the valence band, raising the LH band above the HH one as proved by optical orientation PL experiments[31].

Fig.3.6(a) presents the time-integrated PL spectrum co-polarised (I^+) and counter-polarised (I^-) with the excitation laser at room temperature (RT) obtained from Sample 3026. The excitation laser energy (E_{exc}=1.392 eV) corresponds to the photogeneration of carriers in the GaAsN epilayer, slightly below the GaAs gap. Very similar results are obtained for excitation energy above GaAs. We clearly see that the circular polarisation P_c is negative (opposite to the helicity of the excitation laser) in the low energy part of the spectrum (long wavelength) whereas it is positive on the high energy part. This effect is due to the thermal population at RT of both the heavy-hole and light-hole bands in GaAsN: the splitting of the heavy-hole and light-hole bands due to the biaxial tension is about 24 meV, which is close to thermal activation energy (k_BT) at room temperature [31]. The positive

(negative) circular polarisation on the high (low) energy part of the spectrum comes respectively from the recombination of conduction electrons with heavy (light) holes as expected by the well-known selection rules in III–V semiconductors[32].

In Fig.3.6(b), the time-integrated PL spectra of Sample 3026 and the corresponding circular polarisation are displayed for two temperatures: T = 12 K and T = 300 K. The laser excitation energy is 1.44 eV. At 12 K only the CB-LH transition is observed due to a population of mainly LH valence band states. The polarisation is therefore counter-polarised with respect to the exciting beam.

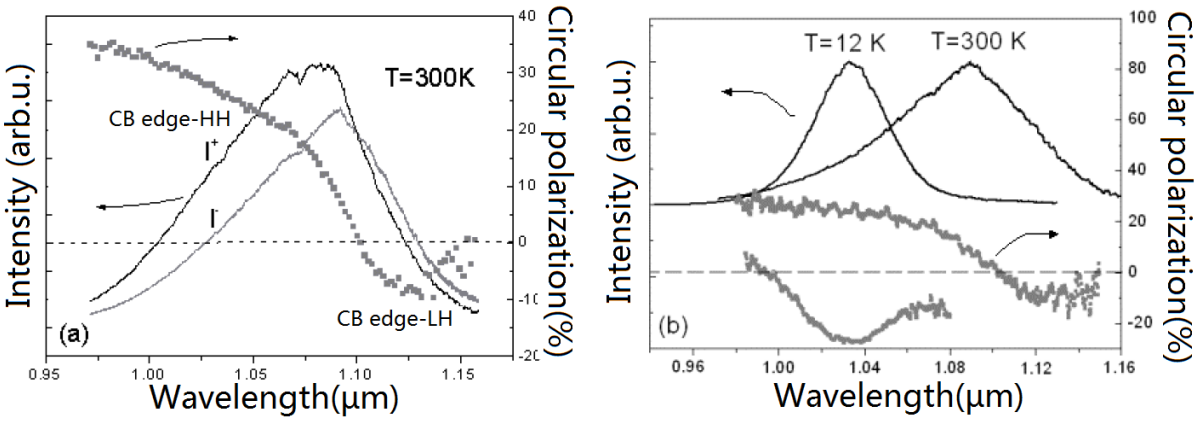

Fig.3.6 - *Sample 3026. (a) T=300K. Time-integrated PL spectra of $GaAs_{1-x}N_x$ epilayer (x = 2.1%) co-polarised (I^+) and counter-polarised (I^-) with the circularly-polarised (Σ^+) excitation laser. The dots display the corresponding circular polarisation. (b) Total PL intensity spectra ($I^+ + I^-$) for two temperatures T=12K and T=300K. The dots display the PL circular polarisation; the PL intensity spectra have been normalized for clarity.*[33]

3.1.5 PL emission variation with different nitrogen content in GaAsN

Fig.3.7 represents the PL spectra of T=300K of samples with different N content (table.2.4) grown in the same conditions. The photon energy of laser beam is set to 1.47 eV (λ_{exc} =843 nm) for all the samples, under pulsed excitation at 300K. As the BAC theory predicts, the band gap variation of $GaAs_{1-x}N_x$ with *x* obtained from the PL spectra follows a parabolic tendency (Fig.3.7(a), see Eq.(3.2)). When the N fraction is quite low ($x \leq 0.15\%$), it is difficult to differentiate the PL signal of GaAsN from the signal coming from GaAs due to their spectral overlapping, therefore we don't include these results from sample 7AM66 and 7AM67 in Fig.3.7. The peak intensities of $GaAs_{1-x}N_x$ are reduced by a factor of 130 when *x* increases from 0.74% to 5.1%, showing the poorer quality of higher N-containing alloys. The full width at half maximum (FWHM) of these epilayer varies strongly with

nitrogen content, which is explained by an increased presence of N expands potential fluctuation [16]. Moreover, Si doped samples 7AM75, 7AM76 show the same emission energies as non Si doped sample at RT.

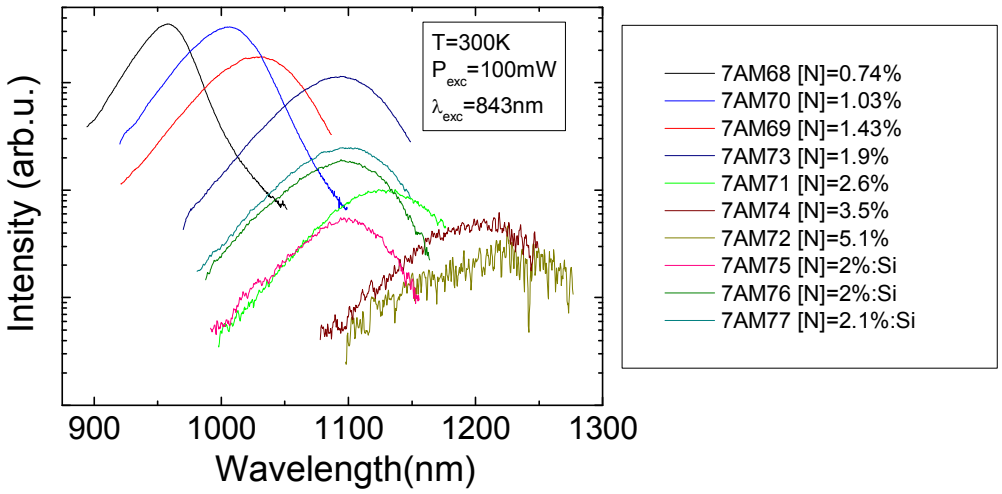

Fig.3.7 - *PL emission spectra of GaAsN samples with different N contents, excited by 100 mW pulsed laser excitation (E_{exc}=1.47eV, λ_{exc}=843nm, T=300K).*

3.2 Spin dynamics in GaAsN

3.2.1 Manifestation of Spin Dependent Recombination (SDR) in GaAsN

Owing to their widely adjustable band gap, dilute nitride (In)$GaAs_{1-x}N_x$ materials have been considered for the realization of devices for the telecommunication spectral windows (λ ≈ 1.3 and 1.55 µm)[12, 13]. However, the presence of N induced defects and clusters largely decrease the mobility of CB electrons, and the CB electron population is largely affected by the efficient capture of N-induced defects. The presence of deep level defects is in general a great disadvantage for optoelectronic applications of dilute nitride semiconductors. In this section, we present now the special properties and functionality of these deep recombination centres in GaAsN can be exploited to evident new effects.

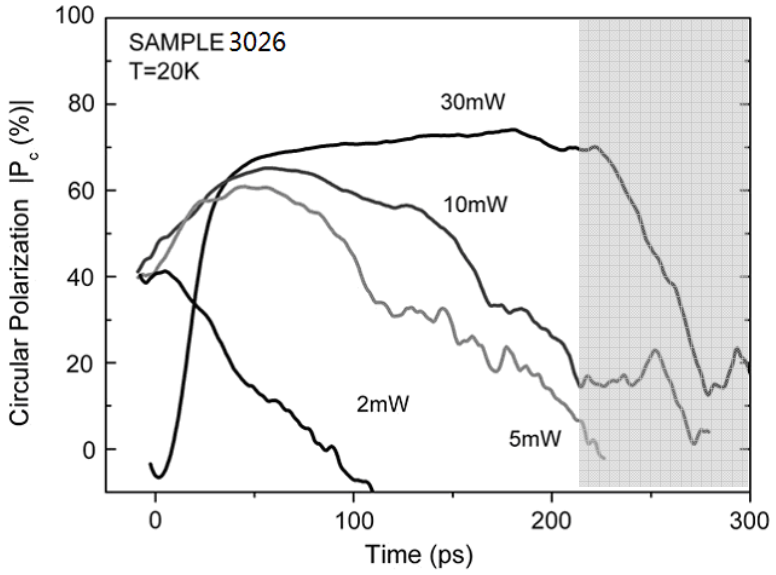

Fig.3.8 - *Time evolution of the absolute value of the PL circular polarisation at T = 20 K for sample 3026 ([N]=2.1%), detected at the CB-LH transition for different excitation powers. (The gray part of the graph represents the region where the signal-to-noise ratio is greatly reduced due to the very weak photoluminescence intensity. Those data therefore do not reflect a real physical effect). The laser excitation energy E_{exc} = 1.392 eV (λ_{exc} =890nm) corresponds to the photogeneration of carriers directly in the tensile strained GaAsN epilayer. Similar results were obtained for excitation energy above the GaAs bandgap.* (*Cited from [34]*)

In Fig.3.8, the low temperature (T = 20 K) dynamics of the absolute value of the PL circular polarisation (P_c) detected at the electron–light hole transition, after a Σ^+ polarised optical excitation on sample 3026 ([N] =2.1%) is presented. The excitation energy is 1.392 eV (λ_{exc}=890 nm), which corresponds to the optically-generated carriers directly in the tensile strained GaAsN epilayer. Due to the biaxial tensile strain, Light-Hole (LH) band is raised above Heavy Hole (HH) one as proved by optical orientation PL experiments[33] (see Fig.3.6). At low temperature (T = 20 K), the main contribution to the photoluminescence signal corresponds to the CB Edge-LH recombination as the thermal energy k_BT is much smaller than the separation $E_{LH} - E_{HH} \approx$ 24 meV for [N]=2.1%. The detected P_c is counter-polarised with respect to the laser which is in agreement with optical selection rule [35] . We measure in Fig.3.8, at low excitation powers (P_{exc} < 5mW), the P_c decay time (τ_s) ≈ 100 ps. This value is in good agreement with the measured of the electron spin relaxation time in GaAs and other III–V compounds[36, 37]. For P_{exc} > 5 mW we can note the progressive appearance of a striking feature: the P_c decay time gradually lengthens as the excitation power is increased. For excitation powers P_{exc} >30 mW, we observe the building up of a strong and stable maximum degree of circular

polarisation $P_c \approx$ 70% which is greater than both its initial value $P_c(t=0)$ and the maximum attainable value in bulk material by optical pumping (50%) according to the optical selection rules[32]. The polarisation of the PL directly reflects the conduction band electron spin polarisation degree as the hole spin relaxation time is very short (<1 ps)[35] (the introduction of N does not significantly modify the valence bands). This surprising result indicates that, in this compound, under sufficient excitation power, the 'apparent' electron spin lifetime τ_s can be much longer than the radiative lifetime ($\tau_R \approx$ 100 ps). It is not possible to account for this power effect by simply considering a suppression of the D'yakonov–Perel mechanism or the quenching of the classical (exciton) spin relaxation mechanisms due to a strong localization of the electron wave-function on N-related defects. The apparent increase of τ_s is instead due to a Spin-Dependent Recombination process (SDR) demonstrated in the next section.

Another experimental evidence of this SDR mechanism is shown in Fig.3.9 for Sample 3026, where we have recorded the total luminescence intensity ($I^+ + I^-$) as a function of time for a circularly-polarised (Σ^+) or linearly-polarised (Σ^x) excitation laser. The laser excitation energy is E_{exc}=1.44eV (i.e. above the GaAs barriers); very similar results are again observed for an excitation energy below the GaAs gap. The remarkable feature in Fig.3.9 is that the total PL intensity decay time is four times shorter for a linearly-polarised excitation compared to a circularly-polarised one. We measure a luminescence decay time ≈20 ps and ≈ 85 ps respectively. We present here the data at RT but we have observed this effect from T = 10 K to 350 K[33].

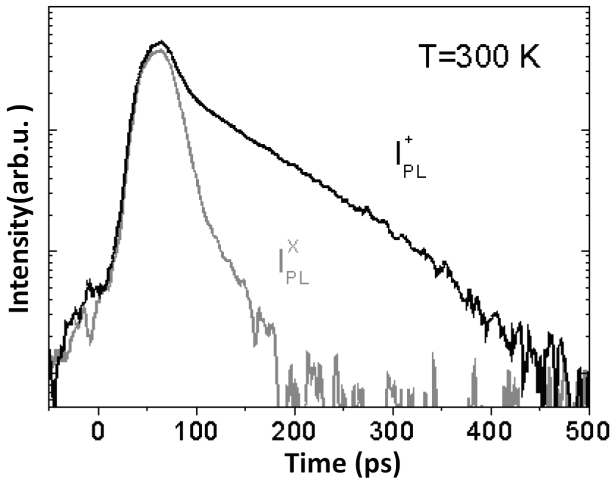

Fig.3.9 - *Sample 3026, T = 300 K. Total PL intensity dynamics under circular (Σ^+) and linear (Σ^x) polarised excitation*[33].

3.2.2 The Spin Dependent Recombination mechanism in GaAsN

It turns out that the very long conduction electron spin polarisation decay time measured in GaAsN is strongly linked to the special features of the recombination processes of free electrons. We demonstrate in this section that both the giant value of the circular polarisation observed at RT and its long persistence can be explained by the spin dependent capture of photogenerated conduction electrons on deep paramagnetic centres.

It is well known that (i) the introduction of nitrogen in GaAs yields the formation of a large density of non-radiative defects[38] and (ii) the PL intensity decay time is not controlled by the intrinsic radiative recombination time but by the non-radiative recombination time on these defects[39, 40]. The data in Fig.3.9 show that this capture time depends on the spin polarisation of the photogenerated free electrons. This effect, called Spin Dependent Recombination (SDR), has been observed over 30 years ago in Si, GaAs and AlGaAs at low temperatures[41-44].

The SDR mechanism is due to the well known Pauli principle which states that two electrons cannot have the same spin orientation in the same orbital state. The key point in SDR is the existence of deep centres which possess an unpaired electron before trapping a conduction electron: these centres are thus paramagnetic. As a consequence, if the photogenerated electron in the CB and the resident electron on the deep centre have the same spin, the photogenerated electron cannot be captured by the centre (it is generally assumed that the triplet levels are not bound). On the contrary, when the photogenerated electron and the resident electron on the deep centre have antiparallel spins, the capture will be efficient. In other words, the recombination time of photocreated electrons depends on the relative spin orientation of the free electron and of the unpaired electron resident on the centre.

In the SDR model developed initially by Weisbuch and Lampel in AlGaAs[42], the electrons resident on the deep centres are assumed to be unpolarised in the absence of light; they become polarised after the photogeneration of free spin-polarised electrons in the CB. The mechanism is the following (Fig.3.10):

(1) The centre can only capture a photogenerated electron from the CB with a spin antiparallel to the spin of the electron already present;

(2) When two electrons of opposite spins occupy a centre, one of them (of either spin) can recombine with a photogenerated hole in the VB, leaving the centre again with a single resident

electron (if this recombination is radiative, we do not detect it since it occurs at much lower energy than the detected interband PL [44]);

(3) Since the capture on the centre is spin-dependent but the recombination process of the electrons trapped on the centre does not depend on the spin, this leads to a dynamic polarisation of the centres: after a few recombination cycles, they become spin-polarised.

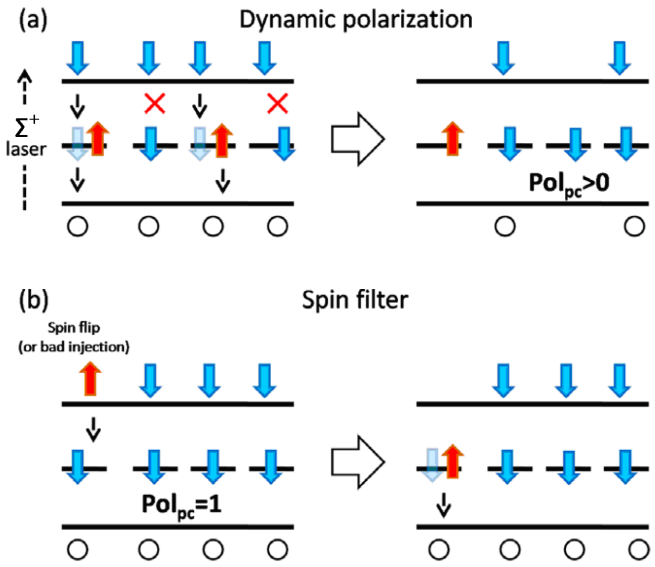

Fig.3.10 - *Sketch of the dynamical deep centre polarisation and spin filter process. (a) At t = 0, after a Σ^+ laser pulse, the photogenerated spin-polarised conduction band electrons polarise the deep centres through a few cycles of non-radiative recombination. For simplicity we have assumed that the laser pulse creates 100% electron spin polarisation. (b) After being polarised, the deep centres act as a spin filter. If a CB electron suffered a spin-flipping mechanism, the polarised deep centres can readily capture the CB electrons of opposite spin. A high value of CB spin polarisation is thus maintained. For illustration purposes we have assumed that the deep centres are fully spin-polarised.*

This mechanism is schematically presented in Fig.3.10(a). At each Σ^+ laser pulse, the spin-polarised photogenerated electrons very rapidly dynamically spin-polarise the deep centres through a few non-radiative recombination cycles. For simplicity, we have assumed that the laser pulse created 100% CB electron spin polarisation. Due to the Pauli principle, the CB electron capture is dependent on the relative spin orientation of the free and deep centre resident electrons. After the capture, the deep centres can annihilate one of the electrons through a recombination with an unpolarised valence band hole. Once polarised, the centres can now act as an effective non-radiative centre only for conduction band electrons of opposite spin, provided that the centres keep their spin

orientation for a time (τ_{sc}) superior to the radiative lifetime (τ_{PL}) and CB electron spin relaxation time (τ_s) ($\tau_{sc} > \tau_{PL}, \tau_s$). The SDR effect not only can control the PL decay time but it can be exploited as a CB electron spin filter to maintain CB electron spin polarisation. If a CB electron flips its spin (Fig.3.10b), it will be immediately captured by the spin-polarised deep centres. A strong spin polarisation of the CB electrons can therefore be maintained as experimentally observed in Fig.3.8, only the total PL intensity being affected.

3.2.3 The SDR ratio (R_{SDR}) as a function of excitation power

In order to observe a sizable spin filtering effect it is necessary that the density of the CB photogenerated electrons (n) relative to the deep paramagnetic centres (N_c) satisfies $n/N_c > 1$: it would be otherwise impossible to achieve full deep centre spin polarisation. The remaining unpolarised centres will act as spin-insensitive non-radiative traps for the CB electrons. The strong power dependence of the P_c reported in Fig.3.8 is well interpreted in terms of the ratio n/N_c . As long as $n/N_c < 1$ ($P_{exc} < 5$ mW) we recover the 'real' electron spin relaxation time τ_s as measured in GaAs. As the photogenerated carrier density increases, the spin filter regime is progressively reached and the maximum P_c (theoretically 100%) is attained.

The presence of a strong power-dependent SDR effect in this sample is experimentally confirmed as shown in Fig.3.11. Fig.3.11(a) presents the time-integrated PL spectra under circularly (Σ^+) and linearly (Σ^X) polarised excitation as a function of the emission wavelength together with the respective ratio ($R_{SDR} = I^+/I^X$, open circles). As a consequence of the SDR effect, we observe a larger PL intensity for Σ^+ excitation compared to the one measured for Σ^x (for a fixed excitation power). This ratio is significantly higher than the corresponding value $R_{SDR} \approx 180\%$ obtained at RT [33]. Fig.3.11(b) displays the SDR ratios for different excitation powers showing that an optimum spin-dependent effect is reached for P_{opt} = 30 mW. This is consistent with the effect observed in Fig.3.8. Considering a 100 µm excitation diameter spot, the GaAsN absorption length and its reflection coefficient, we can estimate P_{opt} corresponding to the photogeneration of an electron density $\approx 10^{17}$ cm^3. The region below 30 mW in Fig.3.11(b) corresponds to a number of photogenerated electrons insufficient to spin-polarise all the deep centres. The slight decrease of the SDR ratio above P_{opt} simply reflects the condition of excess of photogenerated CB electrons which can no more be filtered by an insufficient density of paramagnetic traps ($n/N_c >> 1$).

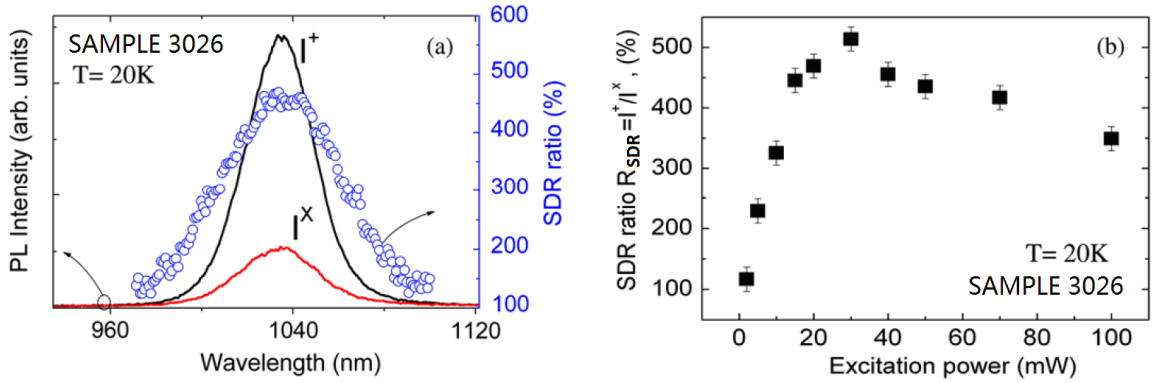

Fig.3.11 - *Sample 3026: (a) Time-integrated PL intensity and the corresponding ratio $R_{SDR} = I^{+} / I^{X}$ under circular (Σ^{+}) and linear (Σ^{X}) excitations as a function of the emission wavelength for sample 3026. The excitation power and wavelength are P_{exc} = 40 mW and λ_{exc} = 890 nm (E_{exc} = 1.39 eV), respectively, and T = 20 K. (b) Power dependence of the maximum SDR ratio under the same conditions.*

3.2.4 Direct observation of spin filtering effect

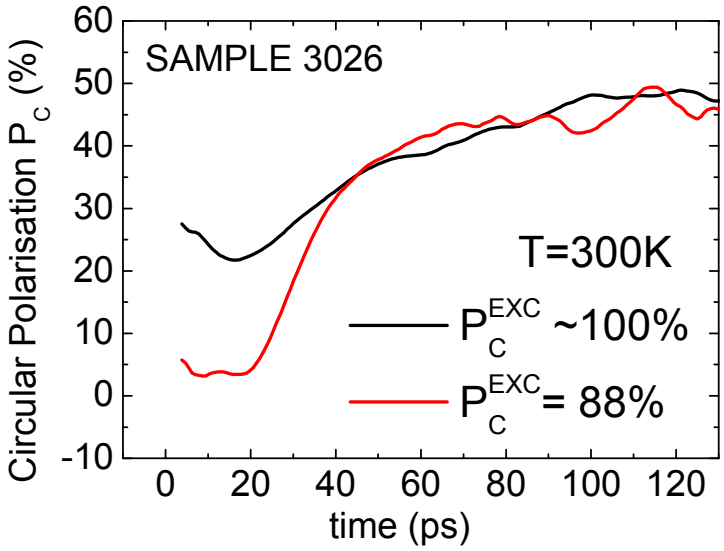

Fig.3.12 - *Sample 3026, T = 300 K, E_{exc} = 1.39eV: Room temperature time evolution of the PL circular polarisation (P_c) under laser excitations with different degrees of circular polarisation.*

The efficiency of the spin filter effect at RT under the optimum excitation power P_{opt} is shown in Fig.3.12, where the P_c dynamics for sample 3026 are presented for laser excitations with different degrees of circular polarisation. A linearly polarised excitation creates no spin polarisation in CB, as an equal number of spin-up and spin-down electrons are created. A decrease of the circular polarisation degree of the excitation light can thus produce the initialization of the system in a state of a lower value of spin polarisation. After the first several picoseconds a strong P_c is recovered, whatever the initial degree of the excitation polarisation is: the SDR-driven spin filter is effective as long as the system conserves a minimum initial imbalance of the spin-up and spin-down electron population and can be switched on by controlling the excitation intensity (i.e. $P_{exc} > P_{opt}$).

It is worth noting that the rise time which characterizes the increase of the circular polarisation in the first tens of picoseconds cannot be simply related to the dynamical polarisation of the deep paramagnetic centres. This rise time is linked to the polarisation of deep centres through a nonlinear system of coupled dynamical equations (see next section). According to the model developed by V.Kalevich et al[45] the circular polarisation rise time is mainly given by the hole recombination time $\tau_h^{-1} = \gamma_h \mathrm{N}_{\uparrow\downarrow}$, where $N_{\uparrow\downarrow}$ is the concentration of paramagnetic centres with two electrons (centres captured one CB electron and thus form a singlet), and γ_h is the hole recombination rate. By decreasing the electron spin polarisation we increase the CB electron trapping probability, thus increasing $N_{\uparrow\downarrow}$. The resulting effect is a decrease of the hole recombination time which controls the deep centres polarisation build-up, leading to a faster photoluminescence polarisation increase.

3.2.5 Spin Dependent Recombination process modelling

In order to obtain quantitative information on the SDR-active defect and its effect on conduction electron via SDR, we carried out a detailed study of the R_{SDR} dependence on excitation light intensity (thus the number of photo-generated free carriers). Representative results were analyzed by the following coupled nonlinear rate equations developed in collaboration with V.Kalevich and E.L.Ivchenko from the IOFFE Institute (Russia)[33, 46], see Fig.3.13(c):

$$
\begin{aligned}
&\frac{dn_{\pm}}{dt} = -\gamma_e n_{\pm} N_{\mp} - \frac{n_{\pm} - n_{\mp}}{2\tau_s} + G_{\pm} - \frac{n_{\pm}}{\tau_r} && (a)\\
&\frac{dN_{\pm}}{dt} = -\gamma_e n_{\mp} N_{\pm} - \frac{N_{\pm} - N_{\mp}}{2\tau_{sc}} + \frac{1}{2}\gamma_h p N_{\uparrow\downarrow} && (b)\\
&N_c = N_{\uparrow\downarrow} + N_+ + N_- && (c)\\
&\frac{dp}{dt} = -\gamma_h p N_{\uparrow\downarrow} + G_+ + G_- - \frac{n_+ + n_-}{\tau_r} && (d)
\end{aligned}
\qquad (3.4)
$$

Here $G_{\pm}$ is the photogeneration rate of free carriers and $n_{\pm}$ ($N_{\pm}$) the density of free electrons (localized electrons at the SDR defect), where the "+" and "-" signs refer to the spin orientations S_z =±1/2, respectively. N_c is the concentration of paramagnetic defect. $N_{\uparrow\downarrow}$ corresponds to the concentration of the defect with two spin-paired electrons. The density of free holes is denoted by p. τ_r, τ_s and τ_{sc} are the radiative recombination time and the spin relaxation times of free and localized electrons, respectively. $\gamma_e(\gamma_h)$ is the free electrons (free holes) recombination coefficient by deep centres. In the analysis we have used the time constants that were obtained in independent experiments or reported in the literature[33, 46], i.e. τ_r = 10 ns, τ_{sc} = 1.5 ns and τ_s = 150 ps. Here, we assume that τ_r is governed by the radiative time of the band-to-band photoluminescence transition. The analysis is not sensitive to τ_r as long as it is much longer than the electron capture and recombination time via the spin-filtering defects, that is, $\tau_r >> (\gamma_e N_{\pm})^{-1}$ and $\tau_r >> (\gamma_h N_{\uparrow\downarrow})^{-1}$. The analysis is also insensitive to τ_{sc}, as long as τ_{sc} >1.5 ns. This leaves only γ_e/γ_h and $\gamma_h N_c$ as fitting parameters. As the absolute values of γ_e and defect concentration N_c cannot be determined independently here, we used a combined fitting parameter $\gamma_e N_c$ which is proportional to the capture rate of free electrons by the defects and can also be used to compare relative defect concentrations in different samples. All these parameters corresponding to each process is schematically shown in Fig.3.13 (a).

In Fig.3.13 (b) we report the time evolution of the PL circular polarisation at P_{exc}=100 mW, the solid line represent the experimental data, while the red dashed line is the result of the simulation. The time evolution of the circular polarisation is well reproduced by the simulation.

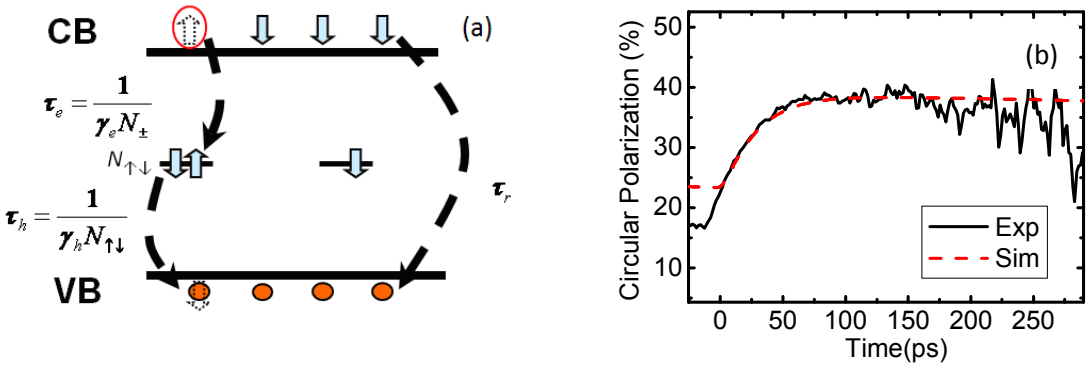

Fig.3.13 - *Sample 7AM73([N]=1.9%), T=300K: (a) The schematic demonstration of the processes considered in the model of Eqs(3.4); (b) The PL polarisation at the saturation regime of R_{SDR}. (* λ_{exc} =843 nm*, E_{exc}=1.47 eV, P_{exc}=100 mW). The dotted lines are the results of the simulations (fitting parameters: γ_e/γ_h=4 and $\gamma_h N_c$=1/35 ps^{-1});*

Although the above model well reproduces the spin filtering effect of conduction electrons (the time evolution of PL circular polarisation), it fails to reproduce the power dependence of the SDR ratio for samples of different N fractions. If only paramagnetic centres are considered, the simulation tends to give the same maximal SDR ratio for each sample whereas only the optimum powers are different (corresponds to density of paramagnetic centres), which is not in agreement with the experimental data. To better reproduce the measurements, we have added to the model the contribution of non-paramagnetic centres giving rise to a spin independent recombination which competes with the Spin Dependent Recombination channel. We therefore obtain Eqs(3.5):

$$
\begin{aligned}
&\frac{\partial n_\pm}{\partial t} = \frac{n_\mp - n_\pm}{2\tau_s} - \gamma_e n_\pm N_\mp - \gamma_r n_\pm p + \gamma_a n_\pm (N_i - N_3) + G_\pm, \quad (a)\\
&\frac{\partial p}{\partial t} = -\gamma_h p N_{\uparrow\downarrow} - \gamma_r (n_+ + n_-) p + \gamma_b p N_3 + G_+ + G_-, \quad (b)\\
&\frac{\partial N_\pm}{\partial t} = \frac{N_\mp - N_\pm}{2\tau_{sc}} - \gamma_e n_\mp N_\pm + \frac{\gamma_h p N_{\uparrow\downarrow}}{2}, \quad (c)\\
&\frac{\partial N_{\uparrow\downarrow}}{\partial t} = \gamma_e (n_+ N_- + n_- N_+) - \gamma_h p N_{\uparrow\downarrow}, \quad (d)\\
&\frac{\partial N_3}{\partial t} = \gamma_a (N_i - N_3) - \gamma_b p N_3, \quad (e)
\end{aligned}
\qquad (3.5)
$$

Here N_i and N_3 are the number of total and occupied non-paramagnetic centres respectively; γ_a is the recombination rate of conduction band electrons to non paramagnetic centres and γ_b is the recombination rate of non-paramagnetic centres to valence band, shown in Fig.3.14(a).

Assuming that the non paramagnetic centres have the same recombination rates as paramagnetic centres (i.e. $\gamma_a / \gamma_e \approx 1$ and $\gamma_b / \gamma_h \approx 1$), the main adjustable parameter of our model is the total number of non paramagnetic centres (shown in Fig.3.14(a)). The role of non-paramagnetic centres is clearly evidenced in Fig.3.14(b). In this graph we present a series of R_{SDR} vs power curves for various rates of paramagnetic to non-paramagnetic centres N_c/N_i keeping constant the total density of defects. As N_c/N_i increases the maximum R_{SDR} decreases and moves to lower irradiance values. As the number of non-paramagnetic centres is increased, their effective recombination time $1/\gamma_a N_i$ (see Eqs.(3.5) and ref[34]) is shortened making this mechanism more likely at lower laser irradiance. At the same time the maximum SDR ratio is reduced as a consequence of the increasing transit of non polarized electrons through the non-paramagnetic centres [55]. The new model (with the inclusion of the non paramagnetic centres) also very well reproduces the monotonous decrease of the SDR ratio observed at incidence powers greater than the optimum value. The best agreement with the experimental results for sample 7AM73 (Fig.3.14(b)) is achieved with $N_i = N_c/10$ where the total paramagnetic centre density N_c is kept constant.

For sample 7AM73 ([N]=1.9%) at RT, the fitting curves of R_{SDR} power dependence is displayed by the dotted lines in Fig.3.14(b), showing a reasonably good agreement with the experimental results. The results clearly show that while photogenerated free electrons is lower than the density of the SDR-active defect, the R_{SDR} is close to 100%, but R_{SDR} increases with increasing excitation intensity of circularly polarised light (thus the concentration of the photogenerated free electrons). With a further increase in the excitation density, R_{SDR} saturates and even slightly decreases because the minority spins of the excess free electrons can no longer be depleted by the SDR via defects. The excitation density at the saturation level of SDR ratio should thus scale with the defect concentration ($\sim 10^{16}$ - 10^{17} cm^{-3}).

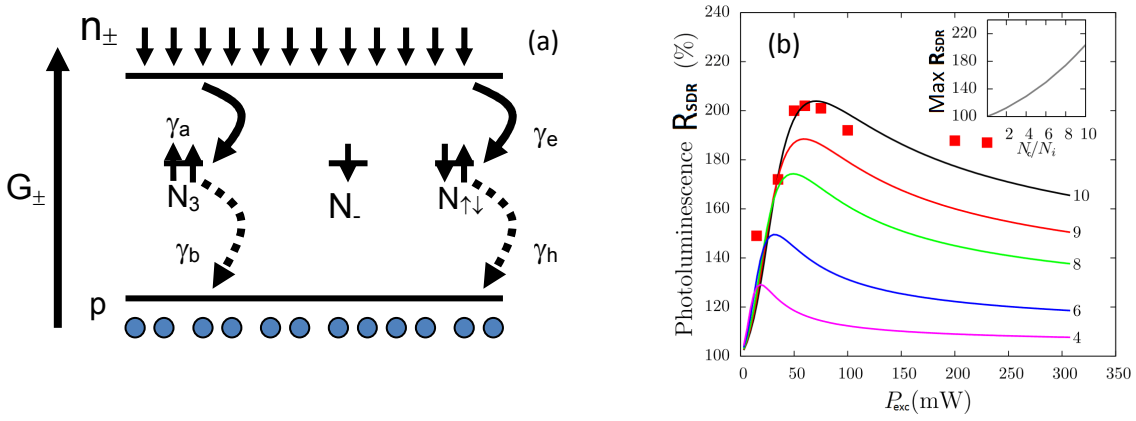

Fig.3.14 - (a) Schematic showing of the model with the consideration of non-paramagnetic centres; (b) Photoluminescence SDR ratio vs excitation power (P_{exc}) for ratios of the paramagnetic to non-paramagnetic centre of N_c/N_i = 4 (purple), 6 (blue), 8 (green), 9 (red) and 10 (black). The (red) squares indicate the experimental results. The dependence of the maximum SDR ratio as a function of N_c/N_i is shown in the inset.

3.2.6 Identification of the paramagnetic centres: ODMR studies

The nature of paramagnetic centre is essential to clarify the SDR mechanism. To identify the exact chemical nature of the spin-filtering defects, we carried out a detailed study by Optically Detected Magnetic Resonance (ODMR; for a review on ODMR, see chapter 2, or ref[47]) in collaboration with Prof W.M.Chen from University of Linköping (Sweden).

ODMR is ideally suited here because it monitors both the conduction electron concentration (via the intensity of the band-to-band photoluminescence) and the spin polarisation of the electrons at the spin-filtering defects (via the electron spin resonance (ESR) intensity that is proportional to $|N_+\text{-}N_-|$), as well as the link between them (the change in the intensity of the band-to-band photoluminescence induced by the ESR transitions).

Under linear polarised excitation (Σ^x), an equal number of spin-up and spin-down conduction electrons are created. If the capture and annihilation of the electrons by the defects dominates over spin relaxation of both conduction and localized electrons, no population difference between the two spin states of the defects is expected, that is, $|N_+ - N_-| = 0$, rendering a vanishing ODMR signal. Under $\Sigma^{\pm}$ excitation, on the other hand, the dynamic spin polarisation of the electrons at the defects

leads to a sizable $|N_+ - N_-|$ and thus a measureable ESR signal. The ESR-induced spin flips of the spin-polarised defect electrons will open up an otherwise spin-forbidden recombination channel (see Fig.3.15(a)). This will lead to a reduction of the free carrier concentration and thus of the corresponding band-to-band photoluminescence intensity, giving rise to a so-called ODMR signal.

The ODMR experiments were first performed on sample 3026 in a range of temperature between 2.5 K and 300 K with a modified ESR spectrometer working at the X-band (~9.3 GHz). Photoluminescence was excited by a Ti:Sa laser at a wavelength of 850 nm. The ODMR signals were detected as spin-resonance-induced changes of the photoluminescence intensity monitored by a cooled Ge detector with a proper selection of optical filters. As examples, we show in Fig.3.15(b) typical ODMR spectra from GaAsN. As expected, a vanishingly weak ODMR signal was observed under Σ^x excitation, whereas rather strong ODMR signals were observed under $\Sigma^{\pm}$ excitation. These findings clearly show that a sizable spin polarisation of the defect electrons was generated under $\Sigma^{\pm}$ excitation, and that a slight change of this polarisation by the ESR directly affects the free carrier concentration, proving the role of the defects in spin filtering.

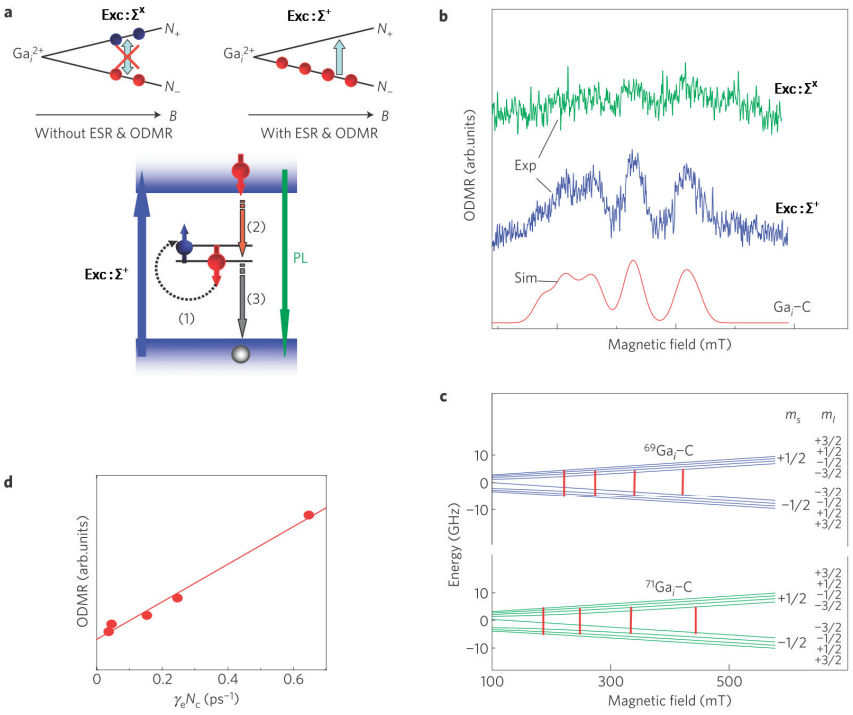

Fig.3.15 - *Identification of the spin-filtering defects by ODMR. (a) Schematic diagrams of the expected ESR transitions under Σ^x and Σ^+ excitation. In the former case, an equal population of the two electron spin states of the* Ga_i^{2+} *defects results in vanishing ESR and ODMR signals as the ESR and ODMR intensity is proportional to the population difference $|N_+ - N_-|$. Under Σ^+ excitation, on the contrary, a sizable $|N_+ - N_-|$ induced by dynamical electron spin polarisation leads to a detectable ESR transition between the two spin states. The ESR transition opens the otherwise spin-forbidden carrier capture and recombination channel, leading to a reduced number of free carriers available for the band-to-band photoluminescence transition—an ODMR signal. The numbers in the parentheses indicate the sequence of events. (b) Typical ODMR spectra obtained by monitoring the total intensity of the band-to-band photoluminescence from sample 3026, obtained at 3K under Σ^x and Σ^+ excitation at 850 nm. The microwave frequency used is 9.2823 GHz. A simulated ODMR spectrum of the identified Ga_i defect (denoted by Ga_i -C) is also shown. (c) Calculated energy levels associated with the electronic and nuclear spin states of the* Ga_i^{2+} *defect. The allowed ESR transitions ($\Delta m_S = \pm 1$ and $\Delta m_I = 0$) occur when the electron spin splitting matches the microwave photon energy, and are marked by the vertical lines. The calculations and simulation were done with the aid of Eq.(3.6) by using the spin Hamiltonian parameters given in the text. (d) ODMR intensities from the identified Ga_i defects as a function of $\gamma_e N_c$ from the result of several samples with different [N] contents. $\gamma_e N_c$ are determined from the rate equation analyses (Eq.(3.4)). The line is a guide to the eye.*

From the analysis of the ODMR data, Ga_i self-interstitial is identified as the core of the spin-filtering defects. This conclusion is based on the following experimental facts. First, the observed multiple ODMR lines arise from a hyperfine structure derived from a strong interaction between an unpaired localized electron spin (S = 1/2) and the nuclear spin of an atom that has two isotopes with a nuclear spin I =3/2 and a 60/40 ratio of natural abundance. This gives rise to four magnetic-dipole-allowed ODMR transitions (Δm_S =±1 and Δm_I =0) for each Ga isotope with an intensity ratio of 60/40 (see Fig.3.15(c)). Ga is the only atom with such unique properties, that is, two naturally abundant isotopes, ^{69}Ga (60.4% abundant) and ^{71}Ga (39.6% abundant), and I = 3/2 for both isotopes. Second, the ODMR spectra are isotropic with a rotation of magnetic field B with respect to the crystallographic axes. This finding reveals that the electron wave-function at the defects should be s-like. This is consistent with the observed strong hyperfine interaction, as the s-like electron wave-function results in a strong Fermi contact term. The involved defects should then be in the Ga^{2+} charge state occupied by a single unpaired electron with an electronic state of A_1 symmetry, as the alternative Ga_{As} antisite was predicted to possess a T_2-symmetry state[48, 49]. To quantitatively confirm this identification, we have carried out a detailed analysis of the ODMR results by a spin Hamiltonian:

$$H=\mu_B g\boldsymbol{B}\cdot\boldsymbol{S}+A\boldsymbol{S}\cdot\boldsymbol{I} \tag{3.6}$$

Here, μ_B is the Bohr magneton, g is the electronic g–factor and A is the hyperfine parameter. g = 2.000, $A(^{69}Ga)$ = 620 × 10^{-4} cm^{-1} and $A(^{71}Ga)$ = 788 × 10^{-4} cm^{-1} are obtained from a best fit to the experimental data for the Ga_i defects in sample 3026. The ratio $A(^{71}Ga)/A(^{69}Ga)$ is in excellent agreement with that of their nuclear magnetic moments $\mu(^{71}Ga)/\mu(^{69}Ga)$ = 1.27. An ODMR spectrum simulated by Eq(3.6) using the obtained parameters is shown as Ga_i-C in Fig.3.15 (b), showing excellent agreement with the experimental data. By using a one electron linear combination of atomic orbital scheme[50] and the charge density of the 4s electron $|\psi_{4s}(0)|^2$ = 72.7 × 10^{24} cm^3 for a free neutral Ga atom[49, 51], the localization of the electron wavefunctions at the Ga_i-C defects is estimated to be 16% (sample 3026). The rather strong localization shows that they are deep-level defects, a prerequisite for efficient carrier recombination.

To further quantitatively confirm that the identified Ga_i defects are indeed responsible for the spin filtering, we examined their ODMR intensity as a function of the spin-filtering defect concentrations deduced by Eq.(3.4), i.e for samples containing different N concentrations. The excellent correlation, shown in Fig.3.15(d), provides further support for the predominant role of these Ga_i defects in spin filtering that has led to the observed strong conduction electron spin polarisation (P_e) at room temperature.

Further improvements in the efficiency of the defect-engineered spin-filtering can be predicted by (1) increasing the ratio between the capture rate of conduction electrons by the Ga_i defects ($\gamma_e N_c$) and the spin relaxation rate of conduction electrons ($1/\tau_s$) and (2) increasing the ratio between $\gamma_e N_c$ and the spin-independent carrier recombination rate ($1/\tau_r$) via other defects. Indeed, the spin relaxation of conduction electrons tends to drive P_e towards zero value at thermal equilibrium (B = 0). Spin-independent carrier recombination via other defects equally depletes conduction electrons of both spins, competing with spin filtering. The maximum P_e value is expected to approach 100% when $\gamma_e N_c >> 1/\tau_s$ and $1/\tau_r$, independent of initial spin polarisation of the incoming electrons before being spin filtered.

3.2.7 Electron spin Filtering by thin GaAsN/GaAs multi-quantum wells

It is well known that modern semiconductor electronic and optoelectronic devices are nearly exclusively based on thin layered and quantum structures grown by epitaxial techniques. An important question to ask is, thus, how effective the spin-filtering functionality will become in thin GaAsN quantum structures. The aim of this section is to address this issue by investigating spin-filtering properties in GaAsN/GaAs quantum wells (QWs) with a width (L_z) in the range of 3-9 nm. In the previous sections we only studied GaAsN epilayer with thickness in the range 50-100nm. This work has again been done in collaboration with the group of Prof W.M.Chen from the University of Linkoping (Sweden).

The studied QWs were grown by molecular beam epitaxy (MBE) on a (001)-oriented semi-insulating or n^+ GaAs substrate, and were capped by a 250-nm thick GaAs layer. All structures contain 7-periods of GaAsN/GaAs QWs with [N] = 1.6%. The GaAsN QW widths are L_z = 3, 5, 7 and 9 nm, sandwiched between 20.2-nm GaAs barriers. Both CW and time-resolved optical orientation techniques were employed at RT. A laser beam propagating parallel to the growth axis, from a CW Ti-sapphire laser or a mode-locked Ti:sa laser (with a pulse width of 1.5 ps and a repetition frequency of 80 MHz), was used as an excitation source. Typical excitation power was up to 300 mW (CW laser) and 100 mW (pulsed laser), focused on a spot of approximately 0.1-1 mm. The excitation wavelengths of 832 nm (CW) and 790 nm (pulsed) were chosen to induce Band to Band (BB) absorption involving HH and LH in GaAs, but not spin-orbit split holes, such that a preferential spin orientation of CB electrons can be created with a maximum value of P_e = 50%[32]. Under such excitation conditions, most of the carriers participating in the BB recombination in the GaAsN QWs were injected from the GaAs barriers and the cap layer. Resulting PL was detected in a back-scattering geometry by a CCD camera in CW experiments or a streak camera. Circular-polarisation of excitation light was provided and that of PL was analyzed by using a

quarter-wave plate together with a linear polariser. ODMR experiments were also done at 9.14 GHz and 4K, by detecting spin-flip induced changes of the BB PL emission.

The spin-filtering effect is distinctly evident from (i) a stronger BB PL intensity under Σ^+ excitation than under Σ^x excitation, and (ii) stronger Σ^+-polarised PL component (I^+) as compared with Σ^- polarised component (I^-) under Σ^+ excitation. A summary of the results from the QWs with different widths is given in Fig.3.16. To quantify the spin-blockade effect, the results are presented in terms of SDR ratio. The spin-filtering effect and the resulting CB electron spin polarisation is assessed from PL circular polarisation $P_c=(I^+ - I^-)/(I^+ + I^-)$. A monotonous increase of the SDR ratio from 1.3 to 1.66 was clearly observed with increasing L_z from 3 nm to 9 nm. This spin-blockade effect is closely correlated with the spin-filtering effect, evident from an increase of P_c from 8 % to 18 %. It should be pointed out that $P_c=-P_e$ (or $P_c=+P_e$) (P_e is the electron spin polarisation) when only the e-HH (or e-LH) emission is monitored and there is no HH-LH mixing. The measured P_c values were obtained by monitoring the shorter wavelength side of the BB PL emission, which is dominated by the e-HH emission, to minimize the spectral overlap with the longer-wavelength e-LH emission and resulting compensation in optical polarisation. However, at such higher detection energies, HH-LH mixing becomes stronger and could in principle lead to an underestimate of P_e by up to 50%[52]. The measured P_c values thus represent the low bound for P_e. Nevertheless, the trend of increasing P_e with increasing L_z is apparent. Different from P_e, the SDR ratio does not suffer from such complications because it monitors the total BB PL intensity (i.e. both $I^+ + I^-$) and no compensation in optical polarisation occurs in this case.

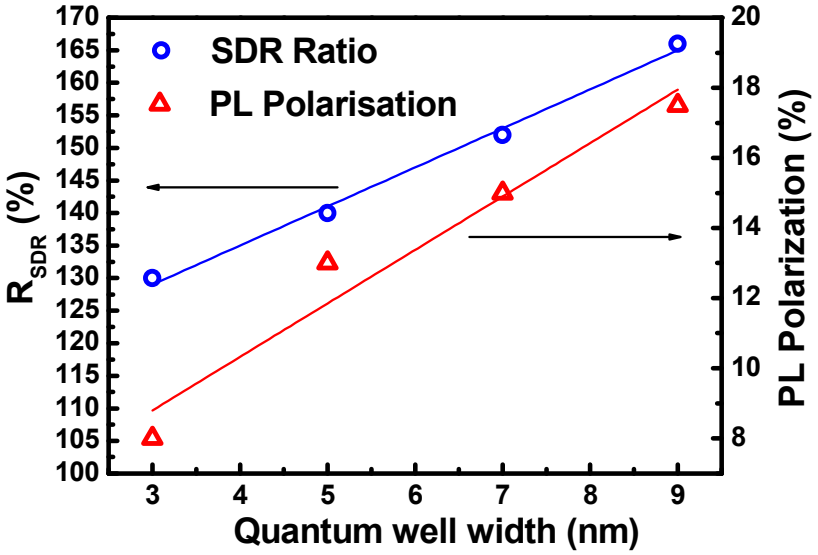

Fig.3.16 - *T=300K, sample [N]=1.6%, CW excitation. Values of SDR ratio (a) and PL polarisation (b) as a function of QW width, obtained at RT under the same excitation power. They represent the maximum values measured over the spectral range of the BB PL emission. The circles are experimental data and the lines are guides to the eye.*

The observed increases in the SDR ratio and P_e with increasing L_z reveal stronger effects of spin filtering in the wider QWs. In principle, several factors can contribute to the trend. Firstly, spin relaxation of CB electrons may vary with L_z [53, 54]. If spin relaxation rate becomes comparable with or exceeds the capture rate of CB electrons by the defects, the latter will no longer be able to catch up with spin relaxation and to deplete spin-flipped CB electrons leading to a reduction in spin-filtering efficiency. Secondly, if the unit-volume density of the defects remains the same in all QWs, which is determined by the identical growth conditions, the sheet concentration of the spin-filtering defects increases with increasing L_z. Thus, 2D CB electrons in the wider QWs are more probable to be spin-filtered by the defects than that in the narrower QWs.

To examine relative importance of the aforementioned mechanisms, we employed time-resolved optical orientation experiments at RT. The results from the QWs with L_z = 3 and 9 nm under linear and circular excitation are shown in Fig.3.17a-b. The observed decay in the 9-nm QWs is overall faster than that in the 3-nm QWs. This finding is consistent with the assumption that the recombination is dominated by the SDR process via the defects, if spin-filtering should be effective [55]. In this case, the PL decay is controlled by capture and recombination of photo-excited carriers via the

defects. The radiative recombination of the BB transition is much less efficient as compared with the SDR process, and therefore its modification by quantum confinement cannot be the reason for the observed change in spin filtering between the QWs with different L_z.

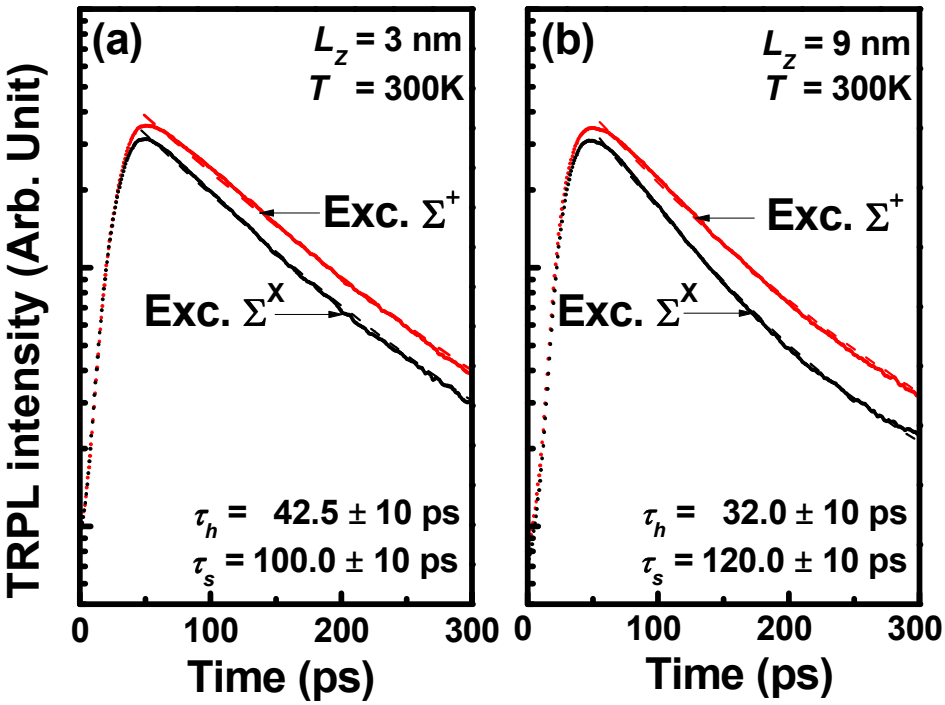

Fig.3.17 - *PL decays of the GaAsN/GaAs QWs with L_z = 3 (a) and 9 nm (b), obtained at RT under circularly and linearly polarised excitation. The dashed lines are the fitting curves with the specified time constants.*

As we discussed before, the observed transient behaviour of the BB PL under circular excitation can be characterized by two decay components [45], distinctive to the physical processes involved in the SDR. Immediately after the laser pulses, photo-excited electrons were quickly captured by the paramagnetic defects, which is too fast to be resolved within our instrument limit of 8 ps. The subsequent capture of holes by the defects, after each of the defects has been occupied by two electrons following the capture of a photo-excited electron, gives rise to the observable fast PL decay component ($\propto \exp(-2t/\tau_h)$ [45], shown in Fig.3.17. During the processes, dynamic spin polarisation takes place for the defect electrons leading to spin blockade of further carrier capture and

recombination via the defects. After that, carriers can only be captured by the defects upon spin flips of CB electrons, characterized by a spin relaxation time τ_s, which corresponds to the slower PL decay component ($\propto \exp(-2t/\tau_s)$ [45]) in Fig.3.17. Whereas the fast PL decay process occurs under both circular and linear excitation, the spin relaxation process is only important under the condition of SDR, explaining the difference between the PL decays under circular and linear excitation. From a best fit of the experimental data, τ_s = 100±10 ps and 120±10 ps were obtained for the QWs with L_z = 3 and 9 nm, respectively. The difference is close to the error bar of the fitting, indicating only a minor effect of QW width in spin relaxation. In any case, a change from τ_s = 120 ps to 100 ps can only decrease the SDR ratio from 1.66 to 1.5 estimated from a rate equation analysis [33, 55]. This cannot account for a SDR ratio reduction from 1.66 to 1.3 observed in our experiments (Fig.3.17), excluding a change in spin relaxation of CB electrons as the dominant mechanism for the observed change in the spin-filtering efficiency of the QWs.

As the BB radiative recombination and CB electron spin relaxation are both insufficient to explain our experimental findings, a change in the sheet concentration of the spin-filtering defects could be the most likely cause. This is in fact indicated by the fitting parameters of τ_h = 42.5±4 ps and 32.0±4 ps for the QWs with L_z = 3 and 9 nm, respectively. As $\tau_h = 1/\gamma_h N_{\uparrow\downarrow}$ [33, 45], where γ_h is the hole recombination coefficient and $N_{\uparrow\downarrow}$ the concentration of the defects occupied by two electrons, the shorter τ_h in the wider QWs evidences a higher defect concentration that can lead to stronger spin-filtering effect. A rate equation analysis supports that the measured difference in τ_h is sufficient to account for the difference in the SDR ratio between the two QWs. This conclusion was further confirmed by our ODMR results, which show that ODMR intensities of the spin-filtering defects[55],1 increase with increasing L_z (Fig.3.18). As the ODMR intensity scales with the carrier caption and recombination rate via the defects [47, 55], which is proportional to the defect concentration, the observed increase of the ODMR intensities signifies a corresponding increase in the concentrations of the active defects with increasing L_z.

---

[1] In the as-grown samples, there are two kinds of Ga_i interstitial defects which contribute to the SDR which are denoted Ga_i-A and Ga_i-B. The essential difference between them is their different environments, which causes different hyperfine interaction terms and different contribution to the SDR. Ga_i-A results as the main contributor for SDR, whereas Ga_i-B gives rise to a much weaker contribution.

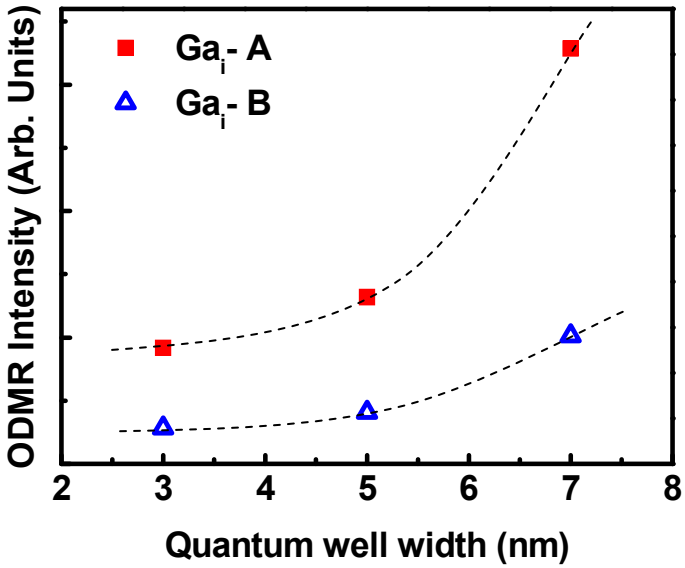

Fig.3.18 - *ODMR intensities of the spin-filtering Ga_i interstitial defects as a function of QW width. The Ga_i interstitial defect denoted by Ga_i-A is characterized by its spin Hamiltonian parameters g=2.005, $A(^{69}Ga)=750\times10^{-4}$ cm^{-1} and $A(^{71}Ga)= 952.5\times10^{-4}$ cm^{-1}, whereas the corresponding parameters for Ga_i-B are g=2.000, $A(^{69}Ga)=1230\times10^{-4}$ cm^{-1} and $A(^{71}Ga)=1562\times10^{-4}$ cm^{-1}. These parameters are obtained from a best fit of the spin Hamiltonian (see Eq.(3.6)) with the experimental ODMR data, as described in Ref*[55]. *The dashed lines are guides to the eyes.*

In conclusion, the defect-engineered spin-filtering effect has been shown to be effective even in GaAsN QWs as narrow as 3 nm. The effect becomes stronger in the wider QWs and is shown to be mainly due to an increase in the sheet concentrations of the spin-filtering defects. Effects of quantum confinement on spin-filtering caused by changes of rates in BB carrier recombination and in CB electron spin relaxation are shown to play a less important role. The results provide a useful guideline for improving spin-filtering efficiency in quantum and nanostructures by means of increasing the concentration of the spin-filtering defects.

3.3 Conclusion

The introduction of a few percent of N in GaAs leads to a radical modification of the electron spin dynamics, which is well explained in terms of the spin-dependent recombination through paramagnetic centres. This leads to high values of the SDR ratio and opens up the possibility of using dilute nitride semiconductors as an effective spin filter for conduction band electrons even at room

temperature. The spin filtering effect is shown to be active as long as the system possesses an initial minimum spin polarisation and can be activated by adjusting the excitation power. We have shown that the spin-filtering effect is efficient in GaAsN epilayers, as well as in GaAsN Quantum wells. ODMR measurements allowed us to identify the character of paramagnetic centres which leads to SDR.

References:

[1]. A. Erol, *Dilute III-V Nitride Semiconductors and Material Systems*. Springer, (2008).

[2]. D. Gollub, M. Fischer and A. Forchel. *Towards high performance GaInAsN/GaAsN laser diodes in 1.5 µm range*. Electronics Letters, **38**: 1183-1184, (2002).

[3]. J. Y. Yeh, L. J. Mawst and N. Tansu. *Characteristics of InGaAsN/GaAsN quantum well lasers emitting in the 1.4-µm regime*. Journal of Crystal Growth, **272**: 719-725, (2004).

[4]. J. Y. Yeh, N. Tansu and L. J. Mawst. *Long wavelength MOCVD grown InGaAsN-GaAsN quantum well lasers emitting at 1.378-1.41 µm*. Electronics Letters, **40**: 739-741, (2004).

[5]. D. S. Kim and D. S. Citrin. *Dynamics of electric field screening in photoconductive THz sources with spatially patterned excitation*. GaAs 2005: 13th European Gallium Arsenide and Other Compound Semiconductors Application Symposium, Conference Proceedings, **708**:417-420, (2005).

[6]. C. R. Lu, H. L. Liu, J. R. Lee, C. H. Wu, H. H. Lin and L. W. Sung. *Optical characterization of InGaAsN/GaAsN/GaAS quantum wells with InGaP cladding layers*. Journal of Physics and Chemistry of Solids, **66**: 2082-2085, (2005).

[7]. S. Bonnefont, B. Messant, M. Boutillier, O. Gauthier-Lafaye, F. Lozes-Dupuy, A. Martinez, V. Sallet, K. Merghem, L. Ferlazzo, J. C. Harmand, A. Ramdane, J. G. Provost, B. Dagens, J. Landreau, O. Le Gouezigou and X. Marie. *Optimization and characterization of InGaAsN/GaAs quantum-well ridge laser diodes for high frequency operation*. Optical and Quantum Electronics, **38**: 313-324, (2006).

[8]. B. Sciana, I. Zborowska-Lindert, D. Pucicki, B. Boratynski, D. Radziewicz, M. Tlaczala, J. Serafinczuki, P. Poloczek, G. Sek and J. Misiewicz. *Technology and characterisation of GaAsN/GaAs heterostructures for photodetector applications*. Opto-Electronics Review, **16**: 1-7, (2008).

[9]. P. H. Wu, Y. K. Su, I. L. Chen, C. H. Chiou, J. T. Hsu and W. R. Chen. *Strain-compensated GaAsN/InGaAs superlattice structure solar cells*. Japanese Journal of Applied Physics, **45**: L647-L649, (2006).

[10]. A. Freundlich, A. Fotkatzikis, L. Bhusal, L. Williams, A. Alemu, W. Zhu, J. A. H. Coaquira, A. Feltrin and G. Radhakrishnan. *Chemical beam epitaxy of GaAsN/GaAs multiquantum well solar cell*. Journal of Vacuum Science and Technology B, **25**: 987-990, (2007).

[11]. P. H. Wu, Y. K. Su, Y. C. Tzeng, H. F. Hong, K. Y. Chu and Y. R. Chen. *A novel GaAsN/lnGaAs strain-compensated multi-quantum wells solar cell*. Semiconductor Science and Technology, **22**: 549-552, (2007).

[12]. M. Kondow, K. Uomi, A. Niwa, T. Kitatani, S. Watahiki and Y. Yazawa. *GaInNAs: A novel material for long-wavelength-range laser diodes with excellent high-temperature performance*. Japanese Journal of Applied Physics, **35**: 1273-1275, (1996).

[13]. M. Kondow, T. Kitatani, K. Nakahara and T. Tanaka. *A 1.3-μm GaInNAs laser diode with a lifetime of over 1000 hours*. Japanese Journal of Applied Physics, **38**: L1355-L1356, (1999).

[14]. W. Shan, W. Walukiewicz, J. W. Ager, E. E. Haller, J. F. Geisz, D. J. Friedman, J. M. Olson and S. R. Kurtz. *Band anticrossing in GaInNAs alloys*. Physical Review Letters, **82**: 1221-1224, (1999).

[15]. I. Suemune, K. Uesugi and W. Walukiewicz. *Role of nitrogen in the reduced temperature dependence of band-gap energy in GaNAs*. Applied Physics Letters, **77**: 3021-3023, (2000).

[16]. M. Gholami, H. Haratizadeh, M. Esmaeili, R. Amiri, P. O. Holtz and M. Hammar. *Alternation of band gap and localization of excitons in InGaNAs nanostructures with low nitrogen content*. Nanotechnology, **19**: 315705, (2008).

[17]. W. Shan, J. W. Ager, W. Walukiewicz, E. E. Haller, M. D. McCluskey, N. M. Johnson and D. P. Bour. *Pressure dependence of optical transitions in $In_{0.15}Ga_{0.85}N/GaN$ multiple quantum wells*. Physical Review B, **58**: R10191-R10194, (1998).

[18]. A. Lindsay and E. P. O'Reilly. *Theory of enhanced bandgap non-parabolicity in GaNxAs1-x and related alloys*. Solid State Communications, **112**: 443-447, (1999).

[19]. P. J. Klar, H. Gruning, W. Heimbrodt, J. Koch, F. Hohnsdorf, W. Stolz, P. M. A. Vicente and J. Camassel. *From N isoelectronic impurities to N-induced bands in the GaNxAs1-x alloy*. Applied Physics Letters, **76**: 3439-3441, (2000).

[20]. C. Skierbiszewski, P. Perlin, P. Wisniewski, W. Knap, T. Suski, W. Walukiewicz, W. Shan, K. M. Yu, J. W. Ager, E. E. Haller, J. F. Geisz and J. M. Olson. Large, *Nitrogen-induced increase of the electron effective mass in $In_yGa_{1-y}N_xAs_{1-x}$*. Applied Physics Letters, **76**: 2409-2411, (2000).

[21]. P. N. Hai, W. M. Chen, I. A. Buyanova, H. P. Xin and C. W. Tu. *Direct determination of electron effective mass in GaNAs/GaAs quantum wells*. Applied Physics Letters, **77**: 1843-1845, (2000).

[22]. F. Masia, G. Pettinari, A. Polimeni, M. Felici, A. Miriametro, M. Capizzi, A. Lindsay, S. B. Healy, E. P. O'Reilly, A. Cristofoli, G. Bais, M. Piccin, S. Rubini, F. Martelli, A. Franciosi, P. J. Klar, K. Volz and W. Stolz. *Interaction between conduction band edge and nitrogen states probed by carrier effective-mass measurements in* $GaAs_{1-x}N_x$. Physical Review B, **73**: 073201, (2006).

[23-24]. F. Masia, A. Polimeni, G. B. H. von Hogersthal, M. Bissiri, M. Capizzi, P. J. Klar and W. Stolz. *Early manifestation of localization effects in diluted GaAsN*. Applied Physics Letters, **82**: 4474-4476, (2003).

[25]. G. Pettinari, F. Masia, A. Polimeni, M. Felici, A. Frova, M. Capizzi, A. Lindsay, E. P. O'Reilly, P. J. Klar, W. Stolz, G. Bais, M. Piccin, S. Rubini, F. Martelli and A. Franciosi. *Influence of nitrogen-cluster states on the gyromagnetic factor of electrons in* $GaAs_{1-x}N_x$. Physical Review B, **74**: 245202, (2006).

[26]. M. P. Vaughan and B. K. Ridley. *Electron-nitrogen scattering in dilute nitrides*. Physical Review B, **75**: 195205, (2007).

[27]. P. R. C. Kent and A. Zunger. *Theory of electronic structure evolution in GaAsN and GaPN alloys*. Physical Review B, **64**: 115208, (2001).

[28]. P. R. C. Kent, L. Bellaiche and A. Zunger. *Pseudopotential theory of dilute III-V nitrides*. Semiconductor Science and Technology, **17**: 851-859, (2002).

[29]. A. Lindsay and E. P. O'Reilly. *A tight-binding-based analysis of the band anti-crossing model in* GaN_xAs_{1-x}. Physica E: Low-dimensional Systems and Nanostructures, **21**: 901-906, (2004).

[30]. E. P. O'Reilly, A. Lindsay, P. J. Klar, A. Polimeni and M. Capizzi. *Trends in the electronic structure of dilute nitride alloys*. Semiconductor Science and Technology, **24**: 033001, (2009).

[31]. A. Y. Egorov, V. K. Kalevich, M. M. Afanasiev, A. Y. Shiryaev, V. M. Ustinov, M. Ikezawa and Y. Masumoto. *Determination of strain-induced valence-band splitting in GaAsN thin films from circularly polarised photoluminescence*. Journal of Applied Physics, **98**: 013539, (2005).

[32]. F. Meier and B.P. Zakharchenya, *Optical orientation*. North-Holland, Amsterdam. (1984)

[33]. D. Lagarde, L. Lombez, X. Marie, A. Balocchi, T. Amand, V. K. Kalevich, A. Shiryaev, E. Ivchenko and A. Egorov. *Electron spin dynamics in GaAsN and InGaAsN structures*. Physica Status Solidi a-Applications and Materials Science, **204**: 208-220, (2007).

[34]. F. Zhao, A. Balocchi, G. Truong, T. Amand, X. Marie, X. J. Wang, I. A. Buyanova, W. M. Chen and J. C. Harmand. *Electron spin control in dilute nitride semiconductors*. Journal of Physics-Condensed Matter, **21**: 174211, (2009).

[35]. D. J. Hilton and C. L. Tang. *Optical orientation and femtosecond relaxation of spin-polarised holes in GaAs*. Physical Review Letters, **89**: 4, (2002).

[36]. A. Kimel, F. Bentivegna, V. N. Gridnev, V. V. Pavlov, R. V. Pisarev and T. Rasing. *Room-temperature ultrafast carrier and spin dynamics in GaAs probed by the photoinduced magneto-optical Kerr effect*. Physical Review B, **63**: 235201, (2001).

[37]. T. F. Boggess, J. T. Olesberg, C. Yu, M. E. Flatte and W. H. Lau. *Room-temperature electron spin relaxation in bulk InAs*. Applied Physics Letters, **77**: 1333-1335, (2000).

[38]. A. Erol, S. Mazzucato, M. C. Arikan, H. Carrere, A. Arnoult, E. Bedel and N. Balkan. *Photo-induced transient spectroscopy of defect levels in GaInNAs*. Semiconductor Science and Technology, **18**: 968-972, (2003).

[39]. A. Markus, A. Fiore, J. D. Ganiere, U. Oesterle, J. X. Chen, B. Deveaud, M. Ilegems and H. Riechert. *Comparison of radiative properties of InAs quantum dots and GaInNAs quantum wells emitting around 1.3 μm*. Applied Physics Letters, **80**: 911-913, (2002).

[40]. R. J. Potter, N. Balkan, X. Marie, M. Senes, H. Carrere, A. Arnoult and C. Fontaine. *Time resolved PL study of GaInNAs quantum wells*. Iee Proceedings-Optoelectronics, **150**: 75-76, (2003).

[41]. D. J. Lepine. *Spin-Dependent Recombination on Silicon Surface*. Physical Review B, **6**: 436, (1972).

[42]. C. Weisbuch and G. Lampel. *Spin-dependent recombination and optical spin orientation in semiconductors*. Solid State Communications, **14**: 141-144, (1974).

[43]. R. C. Miller, W. T. Tsang and W. A. Nordland. *Spin-dependent recombination in GaAs*. Physical Review B, **21**: 1569, (1980).

[44]. D. Paget. *Optical-pumping study of spin-dependent recombination in GaAs*. Physical Review B, **30**: 931, (1984).

[45]. V. K. Kalevich, A. Y. Shiryaev, E. L. Ivchenko, A. Y. Egorov, L. Lombez, D. Lagarde, X. Marie and T. Amand. *Spin-dependent electron dynamics and recombination in $GaAs_{1-x}N_x$ alloys at room temperature*. Jetp Letters, **85**: 174-178, (2007).

[46]. V. K. Kalevich, E. L. Ivchenko, M. M. Afanasiev, A. Y. Shiryaev, A. Y. Egorov, V. M. Ustinov, B. Pal and Y. Masumoto. *Spin-dependent recombination in GaAsN solid solutions*. Jetp Letters, **82**: 455-458, (2005).

[47]. W. M. Chen. *Applications of optically detected magnetic resonance in semiconductor layered structures.* Thin Solid Films, **364**: 45-52, (2000)

[48]. G. A. Baraff and M. Schluter. *Electronic-structure, total energies, and abundances of the elementary point-defects in GaAs*. Physical Review Letters, **55**: 1327-1330, (1985).

[49]. N. Q. Thinh, I. P. Vorona, I. A. Buyanova and W. M. Chen. *Properties of Ga-interstitial defects in* $Al_xGa_{1-x}N_yP_{1-y}$. Physical Review B, **71**: 125209, (2005).

[50]. G. D. a. C. Watkins, J.W. Defects in irradiated silicon. I. *Electron spin resonance of the Si-A center*. Phys. Rev, **121**: 1001-1014, (1961).

[51]. A. K. Koh and D. J. Miller. *Hyperfine coupling-constants and atomic parameters for electron-paramagnetic resonance data*. Atomic Data and Nuclear Data Tables, **33**: 235-253, (1985).

[52]. V. K. Kalevich, E. L. Ivchenko, A. Y. Shiryaev, M. M. Afanasiev, A. Y. Egorov, M. Ikezawa and Y. Masumoto. *The sign of electron g-factor in* $GaAs_{1-x}N_x$ *measured by using the Hanle effect*. Semiconductor Science and Technology, **23**: 114008, (2008).

[53]. A. Malinowski, R. S. Britton, T. Grevatt, R. T. Harley, D. A. Ritchie and M. Y. Simmons. *Spin relaxation in* $GaAs/Al_xGa_{1-x}As$ *quantum wells*. Physical Review B, **62**: 13034, (2000).

[54]. M. I. Dyakonov and V. Y. Kachorovskii. *Spin relaxation of two-dimensional electrons in noncentrosymmetric semiconductors*. Soviet Physics Semiconductors-Ussr, **20**: 110-112, (1986).

[55]. X. J. Wang, I. A. Buyanova, F. Zhao, D. Lagarde, A. Balocchi, X. Marie, C. W. Tu, J. C. Harmand and W. M. Chen. *Room-temperature defect-engineered spin filter based on a non-magnetic semiconductor*. Nature Materials, **8**: 198-202, (2009).

Chapter4

Spin-dependent photoconductivity in GaAsN

In chapter 3 we have introduced and systematically investigated the mechanism of Spin Dependent Recombination in GaAsN by photoluminescence experiments. These results clearly evidence that the conduction band electron density can be largely modulated by the polarisation of the incident excitation light as a result of the SDR mechanism. As photoluminescence and photoconductivity are both affected by the same conduction band electron density, a measurement of the sample photoconductivity should also exhibit a similarly large spin dependent modulation.

Driven by this idea, we present in this chapter the experiments carried out to reveal the Spin-Dependent Photoconductivity in dilute nitride GaAsN, preceded by a brief review of the electrical properties of dilute nitrides.

The very similar features evidenced in both photoconductivity and photoluminescence experiments, namely the dependence as a function of the excitation polarisation, power and external transverse magnetic field, demonstrate that both phenomena are underpinned by the same Spin Dependent Recombination mechanism.

We will conclude this chapter with the description of the non linear dynamical model used to quantitatively interpret the experimental results.

4.1 Introduction

The possibility of tailoring the electronic properties of III–V compounds offered by inclusion of N in the host matrix has stimulated proposals of novel devices for optical telecommunication or photovoltaic applications. However, this research still presents several challenges namely due to the detrimental effects on the electrical and optical properties of the N inclusion into the host matrix. Additionally, the peculiar growth conditions necessary to observe the SDR mechanism, namely a low growth temperature, $T_{growth} \cong 400°C$, and no post-growth annealing, contribute to sensibly lower the carriers' mobility and photoluminescence efficiency through non-radiative centres at even very small N concentration. As what concerns the electrical properties, the main scattering centres include, among others, N-atoms, N-N pairs and clusters. In the Linear Combination of Isolated Nitrogen States model (LCINS), Fahy and O'Reilly[1] were indeed able to describe with great accuracy the variation of the GaAsN electron mobility (μ_e) as a function of N concentration (see Fig.4.1) by including in their model the contribution to the scattering probability of N atoms, N-N pairs and N clusters (triangles).

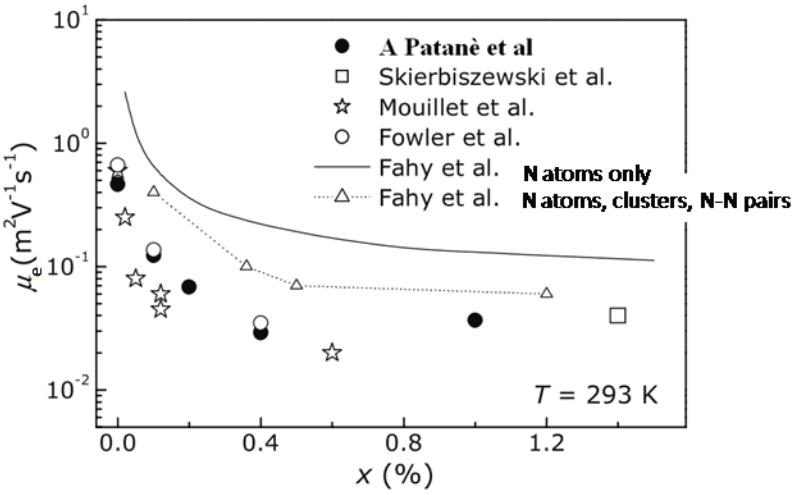

Fig.4.1 - *Dependence of the GaAsN electron mobility (μ) as a function of nitrogen concentration (x) at T = 293 K: comparison of experimental data with theory. Symbols and lines (dotted or solid) refer to experimental data and the results from the different models as cited in reference [2].*

It is apparent from Fig.4.1 that N-containing structures or heterostructures show a dramatic decrease of the mobility even for N concentration as low as 0.02%[3]. An also marked different behaviour of the mobility as a function of the temperature is observed between N-free and

N-containing samples. Figure 4.2[3] shows how, on one side, a decreased growth temperature of N-free heterostructures (REF-HT: T_{growth}=560°C; REF-LT: T_{growth}=450°C;) causes already a drop of the mobility ,conserving however an overall similar behaviour as a function of the temperature. On the other side, the inclusion of N worsens the mobility temperature dependence which strongly deviates from the N-free samples [3].

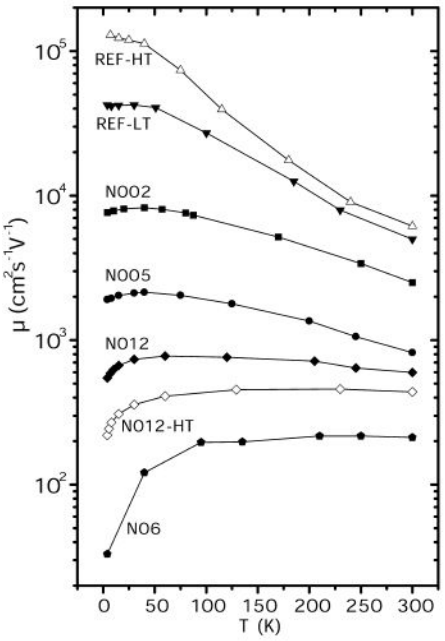

Fig.4.2 - *Hall mobility versus temperature. The sample labels refer to: REF-HT: [N] = 0%, grown at 560°C; REF-LT: [N] = 0%, grown at 450°C; N002: [N] = 0.02%, grown at 450°C; N005: [N] = 0.05%, grown at 520°C; N012: [N] = 0.12%, grown at 450°C; N012-HT: [N] = 0.12%, grown at 560°C; N06: [N] = 0.6%, grown 450°C. (Cited from reference [3]).*

Although the general electronic and optical properties of GaAs are readily hampered by even very small amount of N inclusion in the host matrix, the presence of the efficient deep paramagnetic trapping centres (Ga interstitial) can be turned into use for spin physics purposes as anticipated in chapter 3. We have shown by PL experiments how such an electron-spin-polarised defect can effectively deplete conduction electrons with an opposite spin orientation and can thus turn non-magnetic dilute nitrides semiconductors into an efficient spin filter operating at room temperature and no external magnetic field. The possibility of polarising conducting charges in the material by blocking those with a specific spin direction can also be exploited in transport

experiments albeit the non-ideal characteristics of such structures for electrical/transport measurements.

In this chapter we provide direct and unambiguous experimental proof that the same electron-spin-polarised defects (Ga interstitials), can be used to modulate the sample photoconductivity thus contributing to the research for an electrical spin filter/detector. Key issues for spintronic applications, i.e. the development of a simple, temperature insensitive, all-semiconductor approach for the conversion of the spin information carried by photons into an electrical signal, namely a spin photo detector, working at room temperature has as well been so far mainly unsuccessful [4-6]. Our results aim at proposing the use of materials characterised by the SDR mechanism as attractive alternatives to generate, amplify and electrically detect electron spin polarisation.

4.2 Spin-dependent photoconductivity in GaAsN

The approach to the spin photo-detection/spin-filtering problem proposed here is based on the SDR mechanism in dilute nitrides and leads to the observation of a sizeable spin-dependent photoconductivity change (SDPC) reaching up to $\Delta\sigma/\sigma = [\sigma^{+} - \sigma^{X}]/\sigma^{X} \approx 40\%$, at room temperature and without need of an external magnetic field or ferromagnetic layers. Here $\sigma^{+}(\sigma^{X})$ is the sample photoconductivity for a circular Σ^{+} (linear Σ^{X}) excitation light polarisation. We demonstrate that the electron conductivity, as it is for the PL intensity, can be simply modulated by controlling the spin orientation of the optically injected electrons, which reflects the polarisation state of the optical excitation.

We present in this chapter the results for two samples whose growth and structure characteristics are reminded here: sample 7AM77 is composed of a Si-doped ($2X10^{18}$ cm^{-3}) 50 nm thick $GaAs_{0.979}N_{0.021}$ layer. Sample 79M29 is a nominally undoped, 100 nm thick $GaAs_{0.993}N_{0.007}$. Both samples were grown under the same conditions by molecular beam epitaxy at T=410 °C on a (001) semi-insulating GaAs substrate. The growth was terminated with a 10 nm GaAs cap layer and no post growth rapid thermal annealing was performed. We have observed similar effects in other doped or undoped samples with N composition varying in the range 0.7% to 2.6%. The excitation light was provided by a Ti:Sa laser either in mode-locked regime, yielding the generation of 1.5 ps pulses at a repetition frequency of 80 MHz, or in continuous wave operation, at a wavelength λ_{exc} = 840 nm. The laser was focused into a 150µm diameter spot FWHM in between two Ag electrodes deposited onto the sample surface of variable distance (~1 mm apart, see Fig.2.4b). As the resistivity of the material is very high (see Fig.4.1), simple electrodes can be used. Additionally, the presence of the SPDC has

been likewise demonstrated on a specifically fabricated sample (identical to 79M29) presenting ohmic contacts of variable shape and dimension defined by lithographic techniques and contacted by ultrasound bonding.

The laser light used for the photo excitation is either circularly polarised (right Σ^+ or left Σ^-) or linearly (Σ^X or Σ^Y) polarised and modulated by a mechanical chopper in order to avoid the contribution of the persistent conductivity[7]. The sample conductivity was then measured synchronously using a lock-in amplifier from the voltage drop at the terminals of a 10kΩ load resistor placed in series with the sample (see Fig.2.4a). A constant voltage in the range 0<V<12 volts was applied between the sample electrodes. We have measured a quasi-linear dependence of the photoconductivity on the laser light intensity under $\Sigma^{X,Y}$ light in the investigated average intensity range 50 $W \cdot cm^{-2} < I < 750\ W \cdot cm^{-2}$.

4.2.1 Excitation polarisation dependence

In Fig.4.3(a) is reported the measured photoconductivity change $\Delta\sigma/\sigma$ as a function of the excitation light polarisation for sample 7AM77. The photoconductivity of the sample increases significantly when the excitation light is circularly polarised, i.e., when a population of spin-polarised electrons is photogenerated. We emphasise that no external magnetic field is applied here. Let us recall that the excitation with linearly polarised light leads to the photo-generation of an equal number of spin-down and spin-up electrons. In contrast, when the excitation light is circularly polarised, due to the optical selection rules, the relative concentration of optically generated spin-down to spin-up electrons is 3 to 1, leading to a maximum spin polarisation of photogenerated electrons P_e =50%[8] (holes, yet, are supposed to be completely unpolarised due to their fast spin relaxation mechanisms (~ 1 ps)[9]). As an example, grey circles in Fig.4.3(a) reproduce the same experiment performed on sample 79M29, containing a lower Nitrogen concentration; a much smaller $\Delta\sigma/\sigma$ is measured. Moreover, no spin-dependent photoconductivity change has been measured ($\Delta\sigma/\sigma$ = 0), within the experimental uncertainties, for a non-N-containing sample grown under the same conditions. This demonstrates that the effect observed in Fig.4.3(a) is related to the N incorporation into GaAs. We emphasise that the SDPC change observed here in GaAsN is more than two orders of magnitude larger than the values measured previously in other semiconductors. A photoconductivity modulation $\Delta\sigma/\sigma$ in the range 10^{-6}-10^{-3} was for instance previously reported in Silicon or Germanium [4, 5].

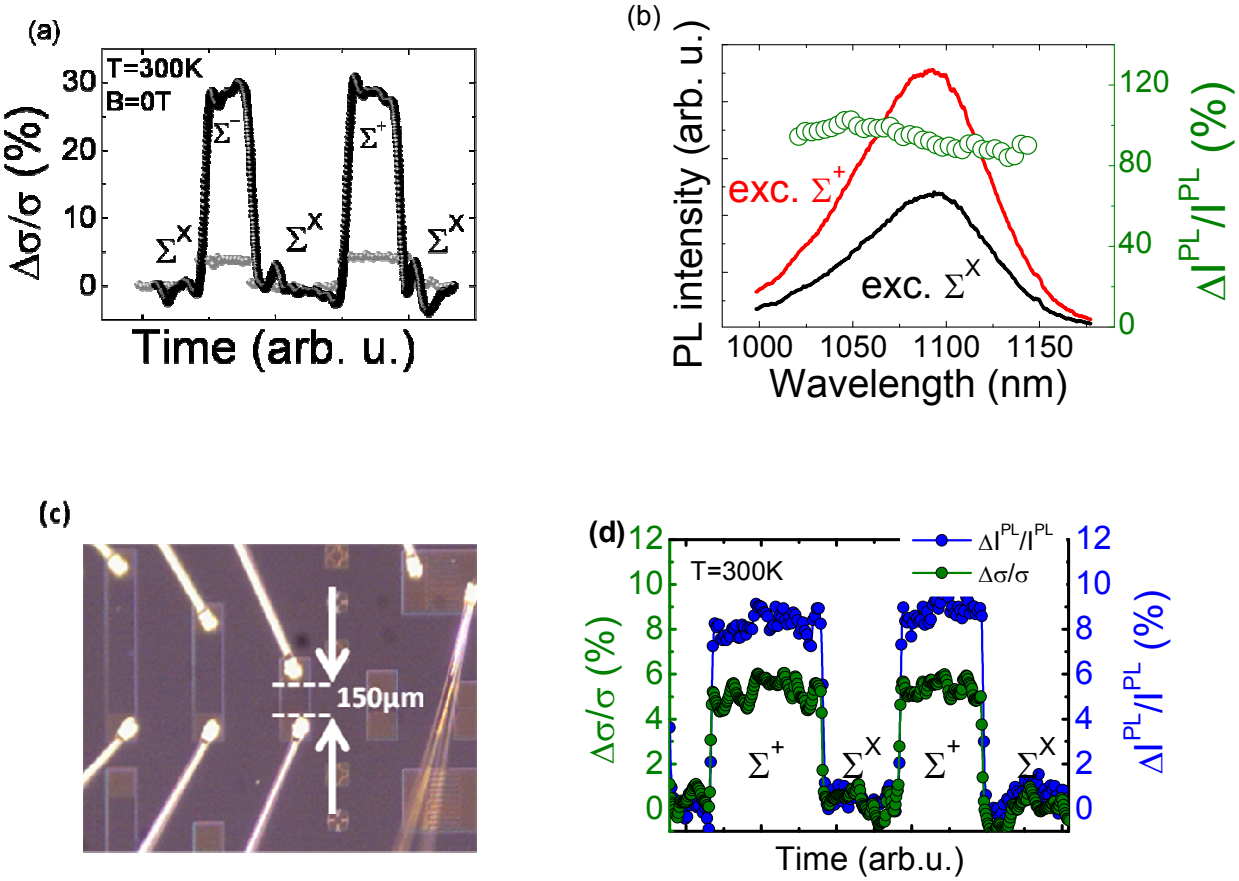

Fig 4.3 - *(a) The spin photoconductivity change (Δσ/σ) as measured on sample 7AM77 (black circles) and on 79M29 (grey circles), as a function of the polarisation state of the excitation light at room temperature. (b) Room temperature time integrated total PL intensity and the corresponding intensity change under circular (Σ^+) and linear (Σ^X) excitation as a function of the emission wavelength for sample 7AM77. The excitation wavelength and intensity are respectively λ_{exc}=840nm and I_{exc}=320W/cm^2. (c) A micro-photographic image of the lithographic sample used to measure simultaneously the spin-dependent PL and PC reported in (d). (d) The spin photoconductivity (green circles) and total photoluminescence (blue circles) intensity changes simultaneously measured on the lithographically prepared sample 79M29.*

The strong photoconductivity modulation observed in Fig.4.3(a) is, as expected, due to the very efficient Spin-Dependent Recombination effect on deep paramagnetic centres (Ga self-interstitials)[10]. To confirm our SDR-based interpretation, we performed simultaneous PL

spectroscopy experiments on the same samples. The SDR, responsible for the SDPC measured in Fig.4.3(a), is directly evidenced by recording the total PL intensity following a Σ^+ or Σ^X laser excitation of equal intensity as shown in Fig.4.3(b) for sample 7AM77. Similarly to the conductivity change, we define the PL intensity change as $\Delta I/I = (I^+ - I^X)/I^X$. The same simultaneous measurements have as well been performed on the lithographically prepared sample 79M29, by detecting the total PL integrated by a photodiode. As it is clear from Fig.4.3 (b,d), the PL intensity is much larger for a Σ^+ excitation compared to a Σ^X as already evidenced in chapter 3: a modulation of the excitation laser polarisation yields a corresponding modulation of the free carrier density (and thus of the conductivity) measured here by transport experiments. As expected from the previous explanation, we measure the same conductivity for a right (Σ^+) or left (Σ^-) circularly-polarised incident light. Very high photoconductivity (or PL intensity) modulation can thus be attained by a polarisation change of the excitation laser. This is the feature upon which relies on the principle of spin filtering: a spin-flipped electron is immediately captured by the spin-polarised deep centres. A strong spin polarisation of the CB electrons can therefore be maintained, only their total density is affected. This result could be exploited to generate spin polarised current at room temperature with nonmagnetic electrodes. Lastly, the strong dependence of the photoconductivity signal on the excitation light polarisation shows that the SDPC signal is governed by electrons as the unpolarised holes do not experience the spin-filtering SDR effect.

Precise information on the CB electron polarisation state (which proportionally translates the excitation light polarisation degree) is consequently possible by a measurement of the electrical current intensity flowing through an external circuit. This is more clearly visible in Fig.4.4 where the SDPC is plotted against a continuous variation of the excitation laser polarisation state from linear to circular, by continuously rotating the λ/4 retarder wave plate through which the linearly polarised laser passes. Like the electrical counterpart of an optical circular polarisation analyzer, the GaAsN layer exhibits a Malus-type law SDPC curve $\Delta\sigma(\theta)/\sigma = (\sigma(\theta)-\sigma^X)/\sigma^X = (\Delta\sigma/\sigma)\cdot\sin^2(2\theta)$, θ being the angle of the laser linear polarisation direction with respect to the λ/4 wave plate neutral axis.

By relying on this effect, dilute nitride GaAsN could be in principle exploited for the realisation of a very simple optoelectronic detector which can electrically trace the degree of polarisation of the incident light (or equivalently the optically induced electron spin population).

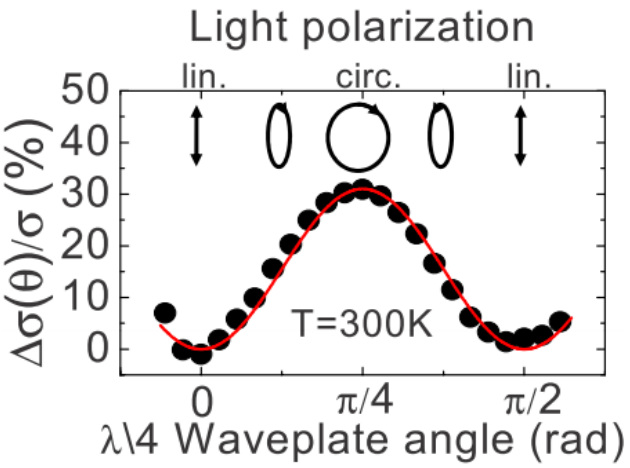

Fig.4.4 - *The SDPC angular dependence (Δσ(θ)/σ) (black circles) for sample 7AM77 as a function of the angle between the laser linear polarisation orientation and the quarter wave plate neutral axis, the latter taken as the origin of the angle axis. The solid red line is a fit to the data (see text).*

4.2.2 Excitation power dependence

The validity of the SDR-based interpretation is also remarkably confirmed by the observation of a very similar dependence of the SDPC on the laser excitation intensity. Fig.4.5(a,b) reports the Δσ/σ intensity dependence at two different temperatures (T=300 K and T=50 K respectively) for sample 7AM77 under pulsed and continuous excitation respectively. This intensity law is indeed well interpreted in terms of the SDR model since, as expected, the centres can be effectively polarised only if the photogenerated carrier density is of the order of the deep centre one.[11] This is exactly what we observe in Fig.4.5. At very low excitation intensities (I_{exc} ≤ 200 W·cm^{-2}) the SDPC can no more be modulated by a light polarisation change. The saturation and the slight decrease of $\Delta\sigma/\sigma$ observed for large excitation intensity (I_{exc} > 500 W·cm^{-2}) correspond to a regime where the photogenerated carrier density is much higher than the deep centre one. All these results clearly confirm that the variation of the photoconductivity as a function of the polarisation of the excitation light observed in Fig.4.5 is due to the change of the CB electron density (due the change of the recombination rate) and not to a spin-dependent change of the carrier mobility[4]. Similarly to the PL detected SDR [11], at lower temperature an overall larger $\Delta\sigma/\sigma$ is measured reaching ≈ 55%, most probably due to a smaller contribution of non-paramagnetic centres.

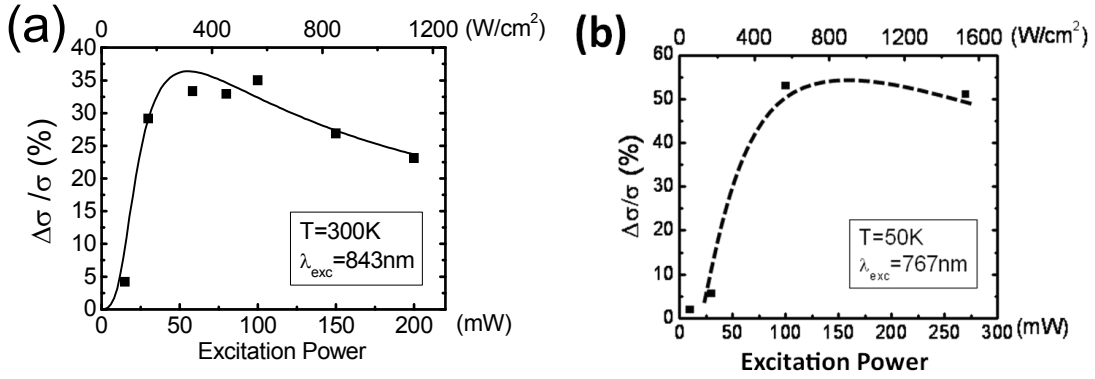

Fig.4.5 - *Sample 7AM77, $\Delta\sigma/\sigma$ power dependence: (a) T=300K, λ_{exc}=843nm, pulsed excitation. The solid line is the result of simulation (see section 4.3). (b) T=50K, λ_{exc}=767nm, CW excitation. Dotted lines are a guide to the eye.*

The same power dependence has been verified for sample 79M29. The low temperature (T=50K) power dependence of the SDPC ($\Delta\sigma/\sigma$) and PL ($\Delta I^{PL}/I^{PL}$) changes, carried out in the exactly same conditions at an excitation wavelength λ_{exc}=780 nm are reported in Fig.4.6, showing a maximum $\Delta\sigma/\sigma \approx 35\%$ [2].

For both samples, the very similar dependence of the SDPC and total PL intensity on the excitation intensity reinforces the interpretation that the observed photoconductivity and photoluminescence modulation phenomena are governed by the same SDR mechanism.

[2] Black squares in Fig.4.6 reports the data obtained under the application of an external transverse magnetic field (Voigt geometry), whose influence will be detailed in the next section.

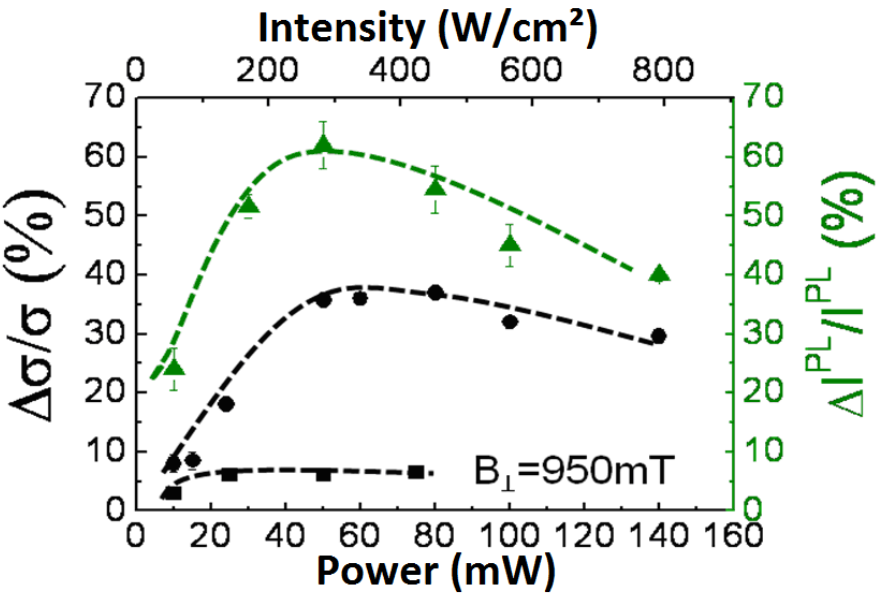

Fig.4.6 - *Low temperature power dependence of the total PL intensity (green triangles) change and of the SDPC changes a function of excitation power without (black circles) and with (black squares) an external in-plane magnetic field. The dashed lines are guides to the eyes. The experimental conditions are: T= 50 K, λ_{exc}=780 nm, bias = 4 V.*

4.2.3 Spin-dependent photoconductivity in a transverse magnetic field: Hanle effect

In order to get further insight and strengthen our physical interpretation of the spin-dependent photoconductivity, we have studied the Hanle effect, i.e the spin depolarisation of electrons in the presence of a magnetic field B in Voigt configuration (B field applied perpendicularly to the propagation direction of the excitation light). In the simplest situation of a single particle, due to the precession of the spin particle around the external magnetic field, the Hanle effect yields a

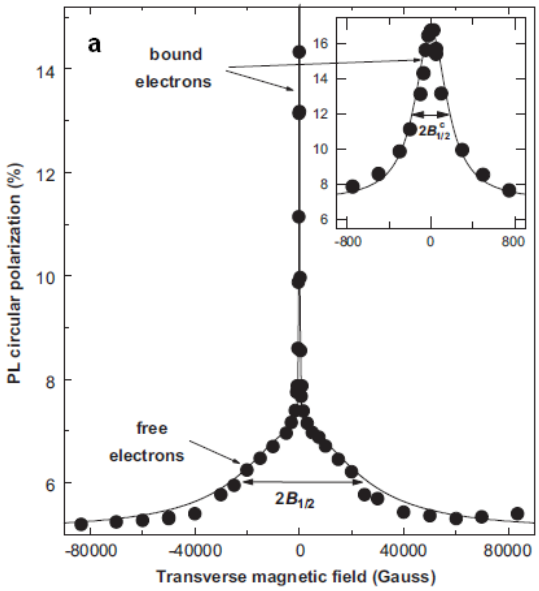

Fig.4.7 - *Typical circular PL intensity polarisation Hanle curve observed by Kalevich et al. in a* $GaAs_{0.979}N_{0.021}$ *sample measured near the PL band maximum at T=300K.* hv_{exc}*=1.312eV,* hv_{det}*=1.163eV. The inset shows the initial part of the Hanle curve in an extended scale* [12].

Lorentzian dependence for the spin polarisation described by:

$$\rho(B) = \frac{\rho(0)}{1+\left(B/B_{1/2}\right)^2} \tag{4.14}$$

where the $B_{1/2}$ is the half-width at half-maximum which can be related to the mean particle spin life time $1/T_s = 1/\tau + 1/\tau_s$ by $B_{1/2} = \hbar / g\mu_B T_s$, where τ (τ_s) is the electron lifetime (spin relaxation time), g is the electron Landé *g*-factor and μ_B is the Bohr magneton. In the case considered in this work, the transverse magnetic field has however the double effect of acting on both the conduction band and localised electrons (only the deep paramagnetic centres are of interest here). The Hanle curve has been previously observed and explained in the case of GaAsN by PL experiments by Kalevich *et al.*[13] (Fig.4.7). This effect is interpreted in terms of the difference in the precession rate (due to different effective Landé g-factor values) of CB electrons and deep centres electrons in the magnetic field. This difference destroys the electrons average spin polarisation, cancelling out the centres dynamical polarisation.

Kalevich *et al.* [12] reported that the Hanle curve of the PL intensity circular polarisation in GaAsN can be well reproduced by a superimposition of two Lorentzians curves (plus a residual polarisation ρ_{res} term): $\boldsymbol{\rho}(B) = \boldsymbol{\rho}_{0\,free}/[1+(B/B_{1/2})^2] + \boldsymbol{\rho}_{0\,centres}/[1+(B/B^c_{1/2})^2] + \boldsymbol{\rho}_{res}$, whose half-widths differ

by two orders of magnitude. They ascribed the larger and narrower Lorentzians to the depolarisation of the conduction band electrons and deep paramagnetic centres respectively, following considerations on their markedly different spin life times ($T_s \approx \tau$ <100ps, $T_{sc} \approx \tau_s \geq$ 2000ps)[3] and g factors.

4.2.3.1 Experimental results

We present in this section the results of the room temperature experimental results on the Hanle effect obtained on sample 7AM77 by both photoluminescence and photoconductivity measurement under the same experimental conditions. An adjustable magnetic field B produced by and electromagnet is applied along the GaAsN plane, i.e. perpendicular to the spin polarisation of electrons created by the light propagating normally to the sample surface (Voigt geometry). For this set of measurements, we have set the continuous wave circularly polarised excitation light to a wavelength λ_{exc}=841 nm and average power P_{exc}=50 mW, and applied a 1 V bias Voltage. The experimental results of both PL and PC measurements are reported in Fig.4.8 (a) and (b) respectively.

Due to the limited magnitude ($B_{max} \approx$ 100mT) of the available electromagnet we can only partially reconstruct the profile of the Hanle curve originating from the depolarisation of the bound electrons (the deep paramagnetic centres). However, as total CB electron density is not affected by free electron precession once the spin of bound electrons is already depolarised, a measurement of the SDR Hanle curve, contrary to a measurement of the PL circular polarisation, should yield only one Lorentzian depolarisation curve. This is indeed confirmed by the theoretical model described at the end of this chapter. From the Lorentzian fits according to the function $\Delta\sigma(B)/\sigma = \Delta\sigma(0)/\sigma\left[1+\left(B/B_{1/2}\right)^2\right]^{-1}$ for both PL and PC experimental data (red solid lines in Fig.4.8), we can extract the value $B_{1/2}^{PL}$ =35 mT and $B_{1/2}^{PC}$ =32.5 mT for the photoluminescence and photoconductivity SDR Hanle experiments. Taking into account a deep centre Landé g-factor g=2[10, 12, 15] these magnetic field values can be converted into the corresponding deep paramagnetic spin life time T_{sc}^{PL} = 162 ps and T_{sc}^{PC} = 175 ps. These results are consistent with the values corresponding a large excitation power previously obtained by PL experiments by Kalevich *et al*[13] . The very similar

[3] For free electrons, the spin life time (T_s) is dominated by the least of τ and τ_s. In GaAsN alloys under study, due to effective capture of free electrons by deep centres, $\tau << \tau_s$ [14] , therefore $T_s \approx \tau$. For small excitation power the bound electron lifetime $\tau_c \rightarrow \infty$ therefore their spin life time (T_{sc}) tends to approach their spin relaxation time (τ_{sc}).

values for $B_{1/2}$ extracted from PL and PC measurement, reflect the fact that in both cases the depolarisation originates from the same mechanism. This is consistent and further reinforces our interpretation that the spin-dependent photoconductivity arises from the same SDR mechanism. The SDPC signal can therefore be easily controlled at room temperature by the application of a transverse magnetic field.

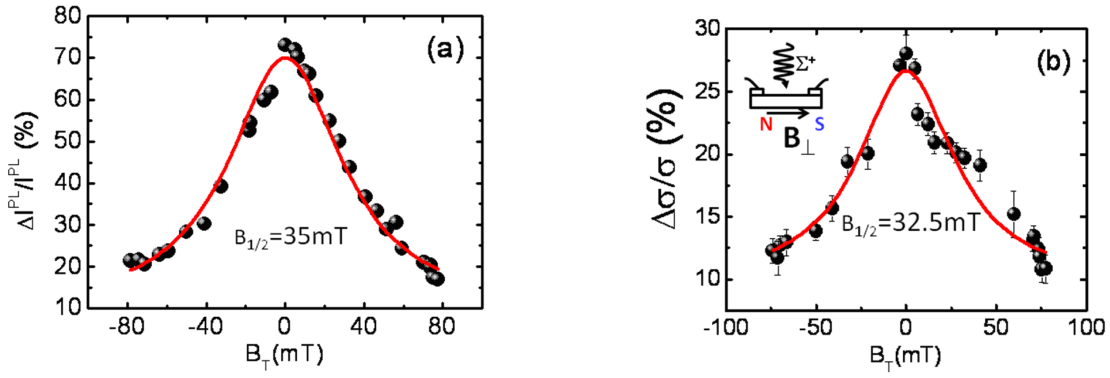

Fig.4.8 – *Room temperature PL (a) and PC (b) SDR variations as a function on en external magnetic field in Voigt geometry under a stationary Σ^+ laser excitation for sample 7AM77. The red curve is a Lorentzian fit (see text).*

Very different results are obtained under pulsed excitation. As observed in Fig.4.9 (blue dots), the strong $\Delta\sigma/\sigma$, observed for B=0, decreases when the amplitude of the magnetic field increases as expected from the previous discussion. However, the measured $B_{1/2}$ = 450 mT is more than one order of magnitude larger than the values measured under continuous wave excitation. The difference of $B_{1/2}$ is interpreted in term of the spin life time of bound electron (T_{sc}) being largely influenced by the different excitation power induced SDR-regime: under CW excitation, the T_{sc} approaches the spin relaxation time of bound electron (τ_{sc}) as the life time of bound electron (τ_c) is relatively longer; whereas under pulsed excitation, due to the much higher photogenerated carrier density, τ_c is greatly reduced causing the spin lifetime T_{sc} to approach τ_c . We observe also that the variation of the SDPC change ratio in the pulsed excitation Hanle experiment can not be related to one of the Lorentzian dependence measured in CW experiments. The detailed model (section 4.3) reproduces correctly the experimental data in pulsed operation (solid line in Fig.4.9).

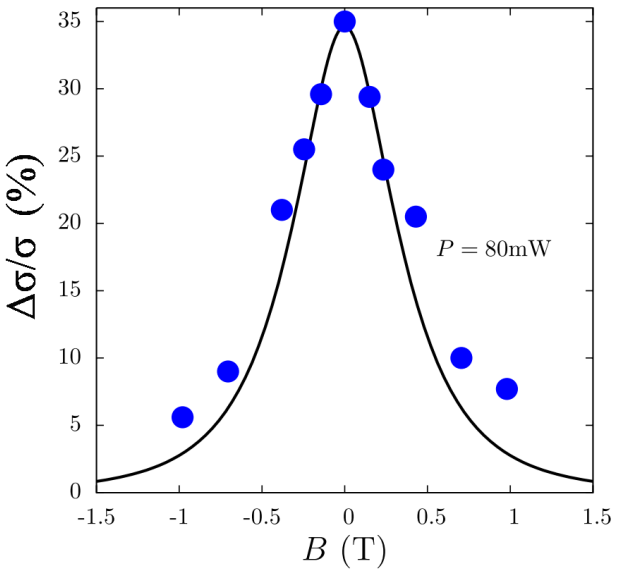

Fig.4.9 - *SDPC as a function of a transverse magnetic filed under pulsed excitation. Blue dots reproduce the experimental results, while the solid line is the results of the theoretical model presented in section 4.3.*

4.2.4 Spin-dependent photoconductivity as a function of the bias voltage

We have finally investigated the influence of the external voltage on the spin-dependent photoconductivity for a fixed excitation intensity (I= 530 W·cm^{-2}). The results of the SDPC together with the current measured under linear excitation are reported in Fig.4.10 for sample 7AM77. When the voltage (and hence the total current) increases, the photoconductivity change $\Delta\sigma/\sigma$ decreases. As expected, at low voltage, $\Delta\sigma/\sigma$ is maximum and reaches $\Delta\sigma/\sigma \approx 50\%$: the device operates here as a very efficient spin filter. For a large voltage (V>5 volts), we still observe a significant spin filtering effect of the current flowing between the electrodes though the number of unpolarised electrically injected CB electrons grows significantly thus reducing the spin filtering efficacy.

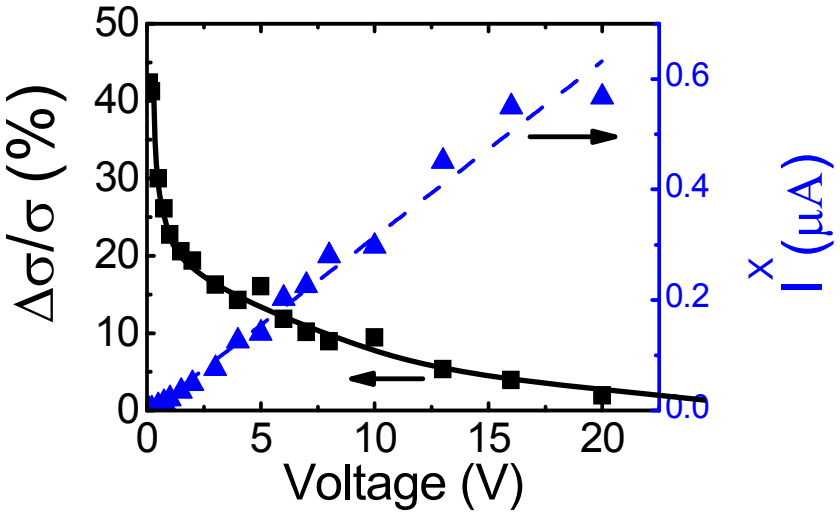

Fig.4.10 - *The I-V curve (black circles) and the corresponding SDPC signal (blue triangles) for sample 7AM77, at T=300K. The excitation wavelength and power are respectively* λ_{exc}*=831 nm and* P_{exc}=100 mW (I_{exc}*=530 W/cm*^{2}*). Lines are guides to the eyes.*

4.3 Theoretical model

4.3.1 Spin-dependent Photoconductivity

To describe the spin-dependent photoconductivity mechanism we have modified the non-linear rate equation model – Eq.(3.5) – originally developed by Kalevich *et al*[14] used to describe the SDR effect in photoluminescence and modified by considering the contribution of non-paramagnetic centres. In order to simulate the transport experiments, the following system of coupled equation has been proposed for spin polarised free electrons ($n_{\pm}$), trapped electrons ($N_{\pm}$), unpolarised holes (p) and centres occupied by an electron singlet ($N_{\uparrow\downarrow}$), total and occupied non-paramagnetic centres (N_i and N_3). This model has been developed in close collaboration with Alejandro Kunold from University of Mexico, who spent two years in LPCNO, Toulouse.

$$\frac{\partial n_{\pm}}{\partial t} - \mu_e E \frac{\partial n_{\pm}}{\partial x} = \frac{n_{\mp} - n_{\pm}}{2\tau_s} - \gamma_e n_{\pm} N_{\mp} + \gamma_a n_{\pm}\left(N_i - N_3\right) + G_{\pm}, \qquad (a)$$

$$\frac{\partial p}{\partial t} + \mu_h E \frac{\partial p}{\partial x} = -\gamma_h p N_{\uparrow\downarrow} + \gamma_b p N_3 + G_{\pm}, \qquad (b)$$

$$\frac{\partial N_{\pm}}{\partial t} = \frac{N_{\mp} - N_{\pm}}{2\tau_{sc}} - \gamma_e n_{\mp} N_{\pm} + \frac{\gamma_h p N_{\uparrow\downarrow}}{2}, \qquad (c)$$

$$\frac{\partial N_{\uparrow\downarrow}}{\partial t} = \gamma_e\left(n_+ N_- + n_- N_+\right) - \gamma_h p N_{\uparrow\downarrow}, \qquad (d) \qquad (4.1)$$

$$\frac{\partial N_3}{\partial t} = \gamma_a\left(N_i - N_3\right) - \gamma_b p N_3, \qquad (e)$$

$$\frac{\partial}{\partial t}(n_+ + n_- - p + N_{\uparrow\downarrow}) + \frac{\partial}{\partial x}(J_+ + J_- - J_p) = 0, \qquad (f)$$

$$N_+ + N_- + N_{\uparrow\downarrow} = N_c. \qquad (g)$$

A drift term for electron and hole has been added to the original set of equations and the diffusion phenomena are neglected in the local current density of electrons and holes since the estimated diffusion longitude for electrons is of a few micrometers compared to the laser spot size of the order of 100µm. The drift density current for electrons is $J_n = J_+ + J_-$ where $J_{\pm} = -e\mu_e E n_{\pm}$ correspond to spin-up and spin-down electrons. For holes, the drift density current is set $J_p = e\mu_h E p$. Here μ_e and μ_h are the electron and hole mobilities respectively. The charge neutrality equation in Eq.(3.4c) is replaced by the partial differential form of Eq.4.1(f). All the values of the different physical parameters (spin relaxation times, capture times, etc…) previously used for the simulation of the photoluminescence experiments are kept unchanged. The electron and hole mobility ratio are set to $\mu_e / \mu_h = 4$ [3]. The set of partial differential equations.4.1 (a)-(g) were solved using finite difference methods. Dirichlet boundary conditions were imposed separately on $n_{\pm}$ and p at the two ends of the sample given that electron and hole distributions build up at opposite sides depending on the bias electric field.

The solid line in Fig.4.11 displays the results of the calculated photoconductivity signal $\Delta\sigma/\sigma$ with the parameters presented above. Fig.4.11 (a) and (b) reproduce respectively the simulated $\Delta\sigma/\sigma$ as a function of the excitation light polarisation and power superposed to the experimental data obtained on sample 7AM77. In both cases, a very good agreement is found.

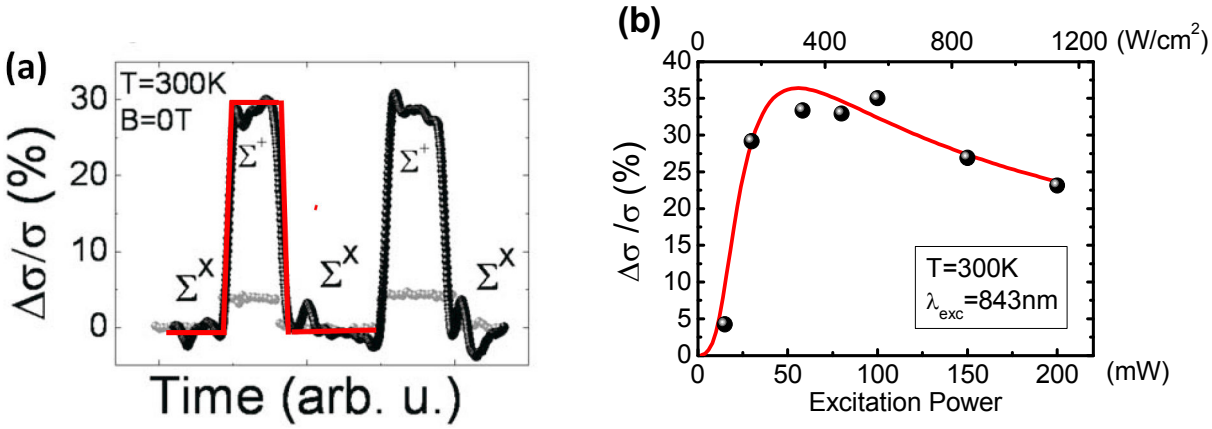

Fig.4.11 – *The $\Delta\sigma/\sigma$ variation as a function of the excitation light polarisation and power, calculated according to the model presented in the text, superposed to the experimental data reproduced from Fig.4.3 and Fig.4.5.*

4.3.2 Spin-dependent Photoconductivity in transverse magnetic field

In order to include magnetic field effects into the model, let us first recall the simple case of a spin 1/2 particle coupled to the magnetic field via the Zeeman Hamiltonian:

$$H = \hbar\boldsymbol{\omega}\cdot\hat{\boldsymbol{S}} \tag{4.2}$$

Where $\boldsymbol{\omega} = g\mu_B\hbar\boldsymbol{B}$, g is the g-factor of free electrons, μ_B is the Bohr magneton and $\hat{\boldsymbol{S}}$ is the dimensionless vector spin operator for the particle. We first focus on how to include the effect of a magnetic field in the rate equations. By solving the Von Neumann equation for the density matrix and averaging the spin vector, one finds that the Hamiltonian - Eq.(4.2) - yields the well known differential equations for the spin precession:

$$\frac{d\boldsymbol{S}}{dt} = \boldsymbol{\omega}\times\boldsymbol{S} \tag{4.3}$$

The spin component along the illumination direction can be identified with the number of spin-up and spin-down electrons through $S_z = (n_+ - n_-)/2$, in unit of $\hbar$ [16]. For the trapped electrons we can work out a similar dynamical equation given by

$$\frac{d\boldsymbol{S}_c}{dt} = \boldsymbol{\Omega}\times\boldsymbol{S}_c \tag{4.4}$$

where $\boldsymbol{\Omega} = g_c \mu_B \hbar \boldsymbol{B}$, with g_c is the g-factor for bound electrons and the spin component along the z axis is written $S_z = (n_+ - n_-)/2$. Hence subtracting the Eq.(4.1a) for spin-down to the same equation for spin-up electrons and adding the term - Eq.(4.3) - for spin precession we obtain:

$$\frac{dS_z}{dt} + \frac{\gamma_e}{2}(nN_1 - 4S_z S_{zc}) + \frac{1}{\tau_s} S_z + (S \times \omega)_z = \frac{G_+ - G_-}{2} \tag{4.5}$$

where $N_1 = N_+ + N_-$. Herein we have used the identity

$$n_+ N_- + n_- N_+ = \frac{1}{2}(nN_1 - 4S_z S_{zc}) \tag{4.6}$$

Adding Eq.(3.4a) for spin-up and spin-down electrons we obtain the rate equation for the total number of conduction band electrons. An analogous procedure can be carried out for the paramagnetic centre variables.

Finally the whole set of rate equations for the spin variables and total conduction band and trapped electrons for SDPC in the presence of an external field is given by:

$$\begin{aligned}
&\dot{\vec{S}} + \frac{\gamma_e}{2}(\vec{S}N_1 - \vec{S}_c n) + \frac{\gamma_a}{2} S(N_i - N_3) + \frac{1}{\tau_s}\vec{S} + \vec{S} \times \omega = \vec{G} + \mu_e E \frac{\partial S}{\partial x} && (a)\\
&\dot{\vec{S}}_c + \frac{\gamma_e}{2}(\vec{S}_c n - \vec{S}N_1) + \frac{1}{\tau_{sc}}\vec{S} + \vec{S} \times \vec{\Omega} = 0 && (b)\\
&\dot{n} + \frac{\gamma_e}{2}(nN_1 - 4\vec{S} \cdot \vec{S}_c) + \gamma_a n(N_i - N_3) = \vec{G} + \mu_e E \frac{\partial n}{\partial x} && (c)\\
&\dot{p} + \gamma_h N_{\uparrow\downarrow} p + \gamma_b p N_3 = G - \mu_h E \frac{\partial p}{\partial x} && (d)\\
&\dot{N}_1 + \frac{\gamma_e}{2}(nN_1 - 4\vec{S} \cdot \vec{S}_c) - \gamma_h N_{\uparrow\downarrow} p = 0 && (e)\\
&\dot{N}_{\uparrow\downarrow} - \frac{\gamma_e}{2}(nN_1 - 4\vec{S} \cdot \vec{S}_c) + \gamma_h N_{\uparrow\downarrow} p = 0 && (f)\\
&\dot{N}_3 = \gamma_a (N_i - N_3) n - \gamma_b p N_3 && (g)
\end{aligned} \tag{4.7}$$

where $\Delta\vec{G} = (G_+ - G_-) \cdot \vec{k}_z/2$ ($\vec{k}_z$ is the unit vector in z-direction). In an isotropic media the dynamical equations for the three axial spin components should be invariant under rotations, hence we rewrite $nN_1 - 4S_z S_{zc}$ to $nN_1 - 4\vec{S} \cdot \vec{S}_c$.

The results of the Hanle effect simulations are reported for pulsed excitations in Fig.4.9. In this case as well, a very good agreement between experimental data and simulation is achieved.

4.5 Conclusions

We have evidenced, in this chapter, a sizeable SDR-driven Spin-Dependent Photoconductivity effect in dilute nitride GaAsN at room temperature without the need of an external magnetic field. The SPDC has been systematically studied as a function of excitation power, polarisation of incident light, transverse magnetic field and electrical bias. The very similar experimental features observed by both photoconductivity and photoluminescence experiments lead us to conclude that the same Ga interstitial deep paramagnetic centres are at the origin of the spin-dependent photoconductivity through the SDR effect. This outcome has been further strengthened by the very good agreement between experimental data and the simulation results of the mathematical transport model developed.

Our results show that using a thin film of GaAsN semiconductor it would be possible to realise a very simple optoelectronic spin detector which can electrically trace the optically induced electron spin population. We also believe that these results show the potential of these dilute nitride materials to generate spin-polarised current at room temperature with nonmagnetic electrodes.

References:

[1]. S. Fahy and E. P. O'Reilly. *Intrinsic limits on electron mobility in dilute nitride semiconductors*. Applied Physics Letters, **83**: 3731-3733, (2003).

[2]. A. Patane, G. Allison, L. Eaves, M. Hopkinson, G. Hill and A. Ignatov. *Tailoring the electrical conductivity of GaAs by nitrogen incorporation*. Journal of Physics-Condensed Matter, **21**: 174209, (2009).

[3]. R. Mouillet, L. A. de Vaulchier, E. Deleporte, Y. Guldner, L. Travers and J. C. Harmand. *Role of nitrogen in the mobility drop of electrons in modulation-doped GaAsN/AlGaAs heterostructures*. Solid State Communications, **126**: 333-337, (2003).

[4]. D. J. Lepine. *Spin-Dependent Recombination on Silicon Surface*. Physical Review B, **6**: 436, (1972).

[5]. H. Dersch, L. Schweitzer and J. Stuke. *Recombination processes in a-Si:H spin dependent photoconductivity*. Physical Review B, **28**: 4678-4684, (1983).

[6]. S. Hovel, N. C. Gerhardt, M. R. Hofmann, F.-Y. Lo, D. Reuter, A. D. Wieck, E. Schuster, W. Keune, H. Wende, O. Petracic and K. Westerholt. *Electrical detection of photoinduced spins both at room temperature and in remanence*. Applied Physics Letters, **92**: 242102, (2008).

[7]. R. M. Jock, *Effect of N interstitials on the electronic properties of GaAsN alloy films*. Dissertation of University of Michigan, (2009).

[8]. F. Meier and B.P. Zakharchenya, *Optical orientation*. North-Holland, Amsterdam, (1984).

[9]. D. J. Hilton and C. L. Tang. *Optical orientation and femtosecond relaxation of spin-polarized holes in GaAs*. Physical Review Letters, **89**: 146601, (2002).

[10]. X. J. Wang, I. A. Buyanova, F. Zhao, D. Lagarde, A. Balocchi, X. Marie, C. W. Tu, J. C. Harmand and W. M. Chen, in *Nature Materials*, **8**: 198-202, (2009).

[11]. F. Zhao, A. Balocchi, G. Truong, T. Amand, X. Marie, X. J. Wang, I. A. Buyanova, W. M. Chen and J. C. Harmand. *Electron spin control in dilute nitride semiconductors*. Journal of Physics-Condensed Matter, **21**: 174211, (2009).

[12]. V. K. Kalevich, E. L. Ivchenko, A. Y. Shiryaev, M. M. Afanasiev, A. Y. Egorov, M. Ikezawa and Y. Masumoto. *The sign of electron g-factor in GaAs1-xNx measured by using the Hanle effect*. Semicond. Sci. Technol, **23**: 114008, (2008).

[13]. A. Y. S. V.K. Kalevich, E.L. Ivchenko, M.M. Afanasiev, A.Yu. Egorov, V.M. Ustinov and Y. Masumoto, *Hanle effect and spin-dependent recombination at deep centers in GaAsN.* Physica B: Condensed Matter, **404**: 4929-4932, (2009).

[14]. V. K. Kalevich, A. Y. Shiryaev, E. L. Ivchenko, A. Y. Egorov, L. Lombez, D. Lagarde, X. Marie and T. Amand. *Spin-dependent electron dynamics and recombination in GaAs1-xNx alloys at room temperature*. Jetp Letters, **85**: 174-178, (2007).

[15]. L. Lombez, P. F. Braun, H. Carrere, B. Urbaszek, P. Renucci, T. Amand, X. Marie, J. C. Harmand and V. K. Kalevich. *Spin dynamics in dilute nitride semiconductors at room temperature*. Applied Physics Letters, **87:** 252115, (2005).

[16]. V. K. Kalevich, E. L. Ivchenko, A. Y. Shiryaev, A. Y. Egorov, L. Lombez, D. Lagarde, X. Marie and T. Amand. *Spin dynamics controlled by spin-dependent recombination in GaAsN alloys at room temperature*. Aip Conf Proc, **893**: 1309-1310, (2007).

Conclusion and perspectives

This work has been centred on the remarkable spin properties of dilute nitride GaAsN, which take origin from the Spin Dependent Recombination (SDR) mechanism of conduction band electrons on deep paramagnetic centres. This feature leads to a spin filtering effect which allows for the maintaining of a very high average spin polarisation of free electrons (>50%) at room temperature and without the need of an external magnetic field. Under the SDR regime no time decay of the photoluminescence circular polarisation is observed.

By exploiting this spin filtering effects we have built and tested an electrical detector of the light polarisation simply based on the variation of the photoconductivity. This Spin Dependent Photoconductivity can achieve values in excess of 40% at room temperature. This shows the potential of these dilute nitride materials to generate spin polarised current at room temperature with nonmagnetic electrodes.

The ODMR experiments have led to the identification of the deep paramagnetic centres responsible for the SDR mechanism: contrary to the most plausible expectations pointing toward defects directly linked to the N atoms, the paramagnetic defects at the origin of the mechanism are ascertained to be Ga interstitials.

Having identified the paramagnetic centre, we could envisage the introduction of “ad hoc” Ga defects in high quality GaAs, not hampered by the low temperature growth of dilute nitrides. Test structures of InGaAs epilayers have been fabricated and implanted with a controlled dose of Ga ions by Focus Ion Beam at the Laboratory of Photonics and Nanostructures (LPN), Marcoussis, France by J.C. Harmand. The preliminary results obtained by time resolved photoluminescence are very encouraging as the signature of the Spin Dependent Recombination has been detected. This is the most important perspective of this work.

On the other side, the Optoelectronics group at the LPCNO plans integrate a GaAsN layer in spin polarised LED structures (Spin-LED). This layer, sandwiched between the injector (Fe or Co followed by a tunnel barrier) and the optical spin detector (Quantum wells or dots), should play the role of a spin filter supplementary to the ferromagnetic layer. This should significantly contribute to the increase of the spin polarisation of the spin polarised current injected into the well or the dots of the structures.

Résumé de la thèse en français :

Une thèse de doctorat de l'INSA rédigée en anglais doit comporter un résumé détaillé en français ; celui-ci est présenté ci-dessous. Le lecteur pourra se référer aux figures et références présentées dans les différents chapitres du manuscrit.

INTRODUCTION

Les matériaux semiconducteurs III-V à base de nitrures dilués ont été étudiés de manière très détaillée depuis plus de 10 ans. Ces composés possèdent des propriétés électroniques remarquables ; l'introduction d'azote en très faible quantité entraine de profondes modifications de la structure de bande de ces matériaux, notamment une forte réduction de l'énergie de bande interdite, typiquement de l'ordre de 150 meV par pourcentage d'azote introduit. De nombreux travaux ont consisté à évaluer le potentiel de ces matériaux semiconducteurs pour la réalisation de diodes lasers ou d'amplificateurs optiques à puits quantiques réalisés sur substrats GaAs pour les bandes passantes à 1.3 μm et 1.55 μm. Une moindre sensibilité des composants à la température a été démontrée du fait des décalages de bande de conduction plus importants existants dans ces structures par rapport à celle des lasers commercialement disponibles à base de puits quantiques InGaAsP sur substrat InP. Cependant les lasers à base de puits quantiques GaAsN ou InGaAsN ont encore des performances limitées du fait de la difficulté de croissance des matériaux et en particulier le contrôle des défauts inhérents à l'introduction de l'azote dans GaAs ou InGaAs.

Le travail de thèse présenté dans ce manuscrit concerne l'étude des propriétés de spin des électrons dans ces matériaux nitrures dilués. L'équipe optoélectronique du LPCNO a en effet montré en 2005 que la dynamique de spin des électrons dans GaAsN était très différente de celle mesurée dans GaAs : (i) une forte polarisation de spin (~40 %) pouvait être mesurée à température ambiante dans une simple expérience de pompage optique orienté en régime stationnaire et (ii) le temps de relaxation de la polarisation circulaire de la photoluminescence était beaucoup plus long que le temps de vie de celle-ci. Ces modifications très importantes des propriétés de spin étaient observées pour des structures de GaAsN avec une composition d'azote de l'ordre de 1%.

Grâce à un travail réalisé en collaboration avec Vladimir KALEVICH de l'Institut IOFFE de St-Petersbourg (Russie), les propriétés de spin surprenantes de GaAsN ont été interprétées par un effet spectaculaire de Recombinaison Dépendante du Spin (SDR) des électrons de conduction sur des centres paramagnétiques apparus dans le matériau du fait de l'introduction d'azote. Notons que cet effet de SDR a été découvert et interprété il y plus de 30 ans à l'Ecole Polytechnique de Paris par J. Lepine dans le Silicium, C. Weisbuch et G. Lampel dans AlGaAs et D. Paget dans GaAs.

Ces résultats préliminaires sur la recombinaison dépendante du spin dans GaAsN ont été présentés dans le chapitre III de la thèse de Laurent Lombez intitulée « Injection optique et Injection électrique de spin dans des nanostructures semiconductrices » soutenue à l'INSA le 13 juillet 2007 (cette thèse comportait également un travail de recherche important sur l'injection électrique de spins à base de puits quantiques GaAs).

Malgré ce travail préliminaire de nombreuses questions restaient ouvertes :

(i) Comment varie la dynamique de spin des électrons en fonction de la fraction d'azote dans le matériau ?

(ii) Quelle est la nature des centres paramagnétiques qui jouent un rôle clé pour la dynamique de spin ?

(iii) Peut-on mesurer les effets de filtrage de spin dans des puits quantiques de GaAsN (au cours de la thèse de Laurent Lombez, seuls des couches de GaAsN de 100 nm d'épaisseur avaient été étudiées)

(iv) Est-il possible de mesurer des effets de photoconductivité dépendante du spin liés au mécanisme SDR ? (seules des expériences de spectroscopie de photoluminescence avaient été mises en œuvre jusqu'ici pour mesurer les propriétés de spin de GaAsN).

Mon travail de thèse résumé brièvement ci-dessous a permis d'apporter des éléments de réponse à ces différents points.

CHAPITRE II

Echantillons et Equipements expérimentaux

La majorité des échantillons étudiée au cours de cette thèse ont été élaborées par Jean-Christophe Harmand (Laboratoire de Photonique et Nanostructures, LPN Marcoussis) par Epitaxie par Jets Moléculaires.

Pour explorer le rôle de la composition d'azote sur les propriétés de filtrage de spin, nous avons étudié une série d'échantillons de $GaAs_{1-y}N_y$ élaborées dans les mêmes conditions de croissance (température optimisée de 410°C) avec y variant de 0.76% à 2.6% avec une couche de protection de 10 nm de GaAs (l'épaisseur de la couche de GaAsN varie de 100 nm pour les faibles fractions d'azote à 50 nm pour les plus fortes). Du fait du désaccord de maille, la croissance de GaAsN sur un substrat de GaAs introduit une contrainte biaxiale en tension qui lève la dégénérescence entre les trous lourds et les trous légers au sommet de la bande de valence ; les trous légers se trouvent alors au sommet de cette bande. Pour un échantillon de GaAsN avec 2% d'azote, l'écart en énergie entre les deux bandes de valence en k=0 est typiquement de 25 meV. Les spectres de photoluminescence à basse température pour ce type d'échantillon sont donc dominés par la recombinaison radiative entre les électrons de conduction et les trous légers de la bande de valence (notons que du fait des règles de sélection optique, la polarisation circulaire de la photoluminescence mesurée sous pompage optique orienté sera alors d'hélicité opposée à la polarisation circulaire du laser d'excitation).

En collaboration avec Weimin Chen de l'Université de Linköping (Suède), nous avons également étudié la dynamique de spin dans des puits quantiques de type GaAsN/GaAs. Ces nanostructures ont été élaborées par épitaxie par jets moléculaires par C.W. Tu de l'Université de Californie, La Jolla. Il s'agit de puits quantiques de GaAsN épitaxiés sur des substrats de GaAs (001) et recouverts par une couche de protection (cap layer) de 250 nm de GaAs. Toutes les structures contiennent 7 périodes de puits quantiques identiques GaAsN/GaAs avec une fraction d'azote de 1.6 % et des barrières de GaAs de 20.2 nm; suivant les échantillons l'épaisseur du puits quantique est L_z= 3, 5, 7 ou 9 nm.

Equipements expérimentaux

Pour les études de spectroscopie de photoluminescence présentées dans ce mémoire, nous avons utilisé une chaîne constituée d'un laser solide qui sert de pompe à un oscillateur Titane-Saphir (Ti:Sa) impulsionnel.

Le laser Titane-Saphir à modes bloqués

Ce laser est un oscillateur Titane-Saphir impulsionnel dont le milieu amplificateur solide est un cristal de saphir dopé au titane (Al_2O_3 :Ti). Nous pouvons l'accorder en longueur d'onde sur un domaine spectral allant de 680 nm jusqu'à 990 nm en mode impulsionnel et nous pouvons le faire fonctionner dans deux configurations différentes qui génèrent des impulsions limitées par transformée de Fourier respectivement picosecondes (≈ 1.5 ps) et sub-picosecondes (≈ 100 fs). Au cours de ma thèse, seul le mode picoseconde a été utilisé pour l'étude de la dynamique de spin dans GaAs. Ce laser peut également être utilisé en mode continu (CW).

En régime impulsionnel, ce laser est un laser à modes bloqués (mode-locking en anglais) qui utilise l'auto-modulation de phase et l'effet Kerr dans le cristal de saphir dopé au titane. Afin d'obtenir des impulsions courtes récurrentes, les modes longitudinaux de la cavité du Ti :Sa sont synchronisés. La synchronisation est elle-même obtenue par l'effet Kerr optique dans le cristal de Saphir dopé au titane. Afin de compenser la dispersion de la vitesse de groupe, étape nécessaire pour obtenir des impulsions, le laser utilise en mode picoseconde un interféromètre de Gires-Tournois.

La fréquence de répétition du laser Ti :Sa est de 80 MHz et sa puissance moyenne suivant la longueur d'onde varie dans la gamme 0,4- 2 Watt (ce qui correspond à une énergie dans l'impulsion de 5 à 25 nJ).

Spectroscopie de Photoluminescence résolue en temps

Le dispositif expérimental d'étude de photoluminescence résolue en temps exposé dans cette thèse se base sur une caméra à balayage de fente (« streak camera » en anglais) en mode synchronisé, à photocathode S1 refroidie (Hamamatsu C5680).

Le principe du dispositif expérimental est très simple : l'échantillon est excité par des impulsions issues du laser Ti:Sa, et le signal de photoluminescence est dispersé dans un monochromateur puis envoyé dans la caméra à balayage de fente.

La lumière à analyser entre dans la caméra et arrive sur une photocathode, générant ainsi un flux d'électrons qui va être ensuite accéléré par un champ électrique dans un tube sous vide. Dans ce tube, les électrons sont déviés par une paire d'électrodes à laquelle est appliquée une tension sinusoïdale calée en phase par rapport au laser Ti :Sa (une photodiode rapide détectant les impulsions périodiques du laser Ti :Sa est employée à cet usage). Les électrons arrivent ensuite sur une galette à micro-canaux où ils sont amplifiés avant de frapper un écran de phosphore. L'image de l'écran de phosphore est collectée et intégrée par une caméra CCD. Les images collectées sont corrigées par le bruit de la photocathode et par sa sensibilité. La caméra étant précédée par un monochromateur qui disperse la lumière horizontalement, les images obtenues sont donc en deux dimensions : horizontalement nous avons la dépendance de l'intensité de la photoluminescence en fonction de la longueur d'onde et verticalement sa dépendance en fonction du temps. Un code des couleurs représente l'intensité de la photoluminescence.

Mesures de la polarisation

Afin de connaître les dynamiques de spin des porteurs dans nos nanostructures, nous utilisons la polarisation de la lumière. Dans un premier temps, il faut pourvoir faire varier la polarisation de la lumière excitatrice. Pour cela, nous disposons d'un compensateur de Soleil-Babinet. Ensuite, pour étudier la polarisation de la photoluminescence, nous disposons de lames demi onde et quart d'onde pour détecter respectivement les composantes linéaires et circulaires du signal. L'orientation des axes de ces lames permet de transformer la composante de la photoluminescence en lumière de polarisation linéaire horizontale. Dans le dispositif expérimental de la caméra à balayage de fente, nous utilisons un cube polariseur après les lames biréfringentes.

Les taux de polarisation circulaire et linéaire se définissent ainsi :

$$P_c = \frac{I^+ - I^-}{I^+ + I^-} \quad \text{et} \quad P_l = \frac{I^X - I^Y}{I^X + I^Y}$$

avec I^+, I^-, I^X, I^Y les intensités des deux composantes de la lumière polarisées circulairement et linéairement.

Mesures de la photoconductivité dépendante du spin

La photoconductivité dépendante du spin a principalement été mesurée dans deux échantillons. Le premier est constitué de 50 nm de $GaAs_{0.979}N_{0.021}$ dopé au Silicum avec une densité nominale $n_{Si}=2x10^{18}$ cm^{-3}. Le deuxième échantillon n'est pas dopé de manière intentionnelle : il est composé

d'une couche de 100 nm de $GaAs_{0.993}N_{0.007}$. Les deux structures ont été élaborées dans les mêmes conditions de croissance (température 410°C) sur un substrat de GaAs (001) semi-isolant.

Pour les mesures de photoconductivité, le laser d'excitation est focalisé sur un spot de diamètre de 150 µm entre deux électrodes d'Argent sépares de ~1 mm déposés à la surface de l'échantillon. La lumière laser, polarisée circulairement (Σ^+ ou Σ^-) ou linéairement (Σ^x ou Σ^y) est modulée par un hacheur mécanique à 700 Hz et la photoconductivité est mesurée par une détection synchrone via la variation de tension obtenue sur une résistance de charge de 10 kΩ placée en série avec l'échantillon. Une tension dans la plage $0 < V < 12$ volts est appliquée entre les deux électrodes.

CHAPITRE III

Recombinaison dépendante du spin dans GaAsN : Etudes par spectroscopie de photoluminescence :

Nous résumons ici les résultats de spectroscopie de photoluminescence présentés dans le chapitre 3 de ce manuscrit.

Mise en évidence de la Recombinaison Dépendante du Spin

Une manifestation spectaculaire de la Recombinaison Dépendante du Spin (*Spin Dependent Recombination, SDR* en anglais) est obtenue en réalisant une simple expérience de spectroscopie de photoluminescence stationnaire en excitant l'échantillon avec de la lumière polarisée circulairement (Σ^+) ou linéairement (Σ^x), les autres paramètres de l'expérience restant parfaitement identiques (énergie d'excitation du laser, puissance d'excitation, *etc*…). Nous observons alors que l'intensité de la photoluminescence est supérieure pour une excitation Σ^+ comparée à celle mesurée pour Σ^x. Pour quantifier ce rapport, on introduit le coefficient SDR qui est simplement : $R=I^+/I^x$ où I^+ est l'intensité totale de photoluminescence après une excitation polarisée Σ^+ et I^x l'intensité totale de photoluminescence après une excitation polarisée Σ^x. Nous avons réussi à mesurer un rapport R pouvant atteindre 500% à T=20 K dans un échantillon de $GaAs_{1-y}N_y$ avec une fraction d'azote de y=0.021. C'est à notre connaissance une des plus fortes valeurs jamais mesurées pour un matériau semiconducteur (nos études précédentes, présentées dans la thèse de Laurent Lombez, avaient été réalisées à température ambiante et la valeur maximale de rapport SDR était de l'ordre de 200%).

Nous avons interprété cet effet spectaculaire par un phénomène de recombinaison dépendante du spin en suivant les travaux pionniers de Lepine, Weisbuch, Lampel et Paget. Le point clé est l'existence de centres paramagnétiques profonds liés à l'introduction d'azote dans la structure (on montrera plus loin que ces centres paramagnétiques, *i.e.* avec un électron présent sur le centre à l'équilibre, sont en fait des interstitiels de Gallium).

La recombinaison dépendante du spin est tout simplement une conséquence du principe d'exclusion de Pauli selon lequel deux électrons ne peuvent pas avoir le même état quantique (même nombre quantique principal, même nombre orbital, même spin).

Lorsqu'un électron est photogénéré dans la bande de conduction, il ne peut être capturé par un centre paramagnétique situé dans la bande interdite que si son spin est anti-parallèle au spin de l'électron déjà présent sur le centre. La capture de ce photo-électron dépend donc de l'orientation relative du spin des électrons photogénérés et du spin des électrons sur les centres paramagnétiques.

Avant l'excitation lumineuse, les centres paramagnétiques ne sont pas initialement polarisés en spin (même nombre de centres peuplés avec un électron résident de spin UP que de centres peuplés avec un électron résident de spin DOWN). Par contre si l'excitation lumineuse est polarisée circulairement, ces centres vont se polariser de manière dynamique en suivant le mécanisme suivant :

(i) Comme nous l'avons dit précédemment, la capture sur le centre paramagnétique ne peut se faire que si le spin de l'électron libre photogénéré dans la bande de conduction est antiparallèle à celui de l'électron résidant sur le centre.

(ii) Une fois que le centre est peuplé par deux électrons formant un singulet , l'un des deux électrons va se recombiner radiativement ou non avec un trou photogénéré de la bande de valence (qui a très rapidement perdu son spin), laissant à nouveau le centre peuplé par un seul électron (remarquons que si cette transition est radiative, elle se fera dans l'infra-rouge et nous ne la détectons pas).

(iii) Comme la capture sur le centre est dépendante du spin mais la recombinaison entre un des deux électrons du centre avec le trou ne dépend pas du spin, les électrons des centres vont progressivement se polariser en spin après quelques cycles d'excitation. Nous sommes en présence d'une situation de polarisation dynamique des centres paramagnétiques ; le spin des électrons de ces centres est co-polarisée avec celui des électrons photogénérés.

Après une excitation polarisée circulairement (Σ^+ ou Σ^-), les centres paramagnétiques vont se polariser de manière dynamique et aucune capture d'électrons photogénérés par les centres ne sera plus possible (puisqu'ils ont le même spin) ; ces électrons vont alors se recombiner de manière radiative avec les trous photogénérés. Par contre, après une excitation polarisée linéairement (photogénération de la même densité d'électrons de spin UP que d'électrons de spin DOWN), les centres paramagnétiques vont rester non polarisés et donc la capture sur ces centres va être plus favorable que la recombinaison radiative. Ceci explique que lorsque l'on détecte la transition interbande (Bande de Conduction – Bande de Valence), l'intensité de la photoluminescence est plus

forte pour une excitation polarisée circulairement que pour une excitation polarisée linéairement. Le fait que l'on observe ces effets pour des températures variant de 10 à 300 K montrent que ces centres paramagnétiques sont profonds.

Nous avons bien-entendu étudié l'effet de la puissance d'excitation sur le rapport SDR. A très faible puissance d'excitation, nous mesurons R~100 % (pas d'effet SDR) comme attendu. En effet, si la densité d'électrons photogénérés polarisés en spin est très faible devant la densité de centres paramagnétiques, la polarisation dynamique des centres ne se produit pas. Pour un échantillon avec y=2% d'azote, nous mesurons un optimum d'effet SDR (R~500 %) pour une puissance d'excitation de 30 mW, ce qui correspond typiquement à une densité de porteurs photogénérés de l'ordre de 10^{17} cm^{-3}. Ceci donne une estimation assez grossière de la densité de centres paramagnétiques.

Lorsque la puissance d'excitation augmente davantage, nous avons observé une légère diminution du rapport SDR ; la modélisation de l'effet de recombinaison dépendante du spin montre que cet effet est lié au fait que les électrons photogénérés deviennent trop nombreux et que les canaux de recombinaison non-radiative sur des centres non paramagnétiques doivent être pris en compte.

Dynamique de la polarisation circulaire de la photoluminescence

La recombinaison dépendante du spin a de fortes répercussions sur la dynamique de spin des électrons libres dans GaAsN.

A faible puissance d'excitation, nous avons mesuré par spectroscopie de photoluminescence résolue en temps un temps de déclin de la polarisation circulaire de la photoluminescence de l'ordre de 100 ps à basse température, tout à fait comparable à celui qu'on peut mesurer dans GaAs (sans azote). Ce temps est contrôlé par le processus de relaxation de spin de l'exciton à basse température et par la relaxation de spin de l'électron de type D'yakonov-Perel à température ambiante.

A plus forte puissance d'excitation (>~2 mW) nous observons une augmentation du temps de déclin de la polarisation circulaire de la photoluminescence. Pour une puissance d'excitation de l'ordre de 30 mW, la dynamique de polarisation circulaire est tout à fait surprenante : le taux de polarisation initiale est de l'ordre de 40%, il augmente progressivement au cours des 50 premières picosecondes pour atteindre une valeur de l'ordre de 70% (valeur supérieure à la polarisation moyenne de spin des électrons photogénérés qui est de 50% !) puis reste stable au cours du temps jusqu'à la fin de la recombinaison radiative. Il semble donc que le temps « apparent » de relaxation

de spin de l'électron devient bien supérieur au temps de déclin de la photoluminescence. On pourrait imaginer un effet du type « motional narrowing » du mécanisme de relaxation de spin D'yakonov-Perel à forte puissance d'excitation mais ceci n'expliquerait pas l'augmentation initiale de la polarisation dans les premières dizaines de picosecondes, ni la valeur de polarisation très élevée de 70%. Il se trouve en fait que cette dynamique de polarisation de spin tout à fait atypique est observée pour les mêmes puissances d'excitation que celles où le rapport R de recombinaison dépendante du spin est supérieur à 1. Cette polarisation de spin géante et stable au cours du temps, mesurée à forte puissance, est bien liée au mécanisme de recombinaison dépendante du spin. L'augmentation initiale de la polarisation circulaire de la photoluminescence reflète la phase de polarisation dynamique progressive des centres paramagnétiques et le blocage qui en découle de la capture des électrons dont le spin est parallèle à celui des électrons des centres. Le taux de polarisation de spin moyen des électrons de la bande de conduction peut donc en principe atteindre 100% ; le fait qu'il ne décline plus ensuite au cours du temps n'est pas lié à un temps de relaxation de spin de l'électron de conduction très long (il reste le même qu'à basse puissance d'excitation) ; lorsque l'un des électrons de conduction relaxe son spin, il est immédiatement capturé par un centre (puisque son spin est désormais anti-parallèle au spin des électrons présents sur les centres). En conséquence, la relaxation de spin d'un électron de conduction n'a pas d'influence sur la polarisation de spin moyenne des électrons de conduction : lorsqu'un électron relaxe son spin il disparait simplement de la bande de conduction. Ceci explique que la polarisation circulaire de la photoluminescence (qui sonde, rappelons-le, la recombinaison radiative entre les électrons libres de conduction et les trous non polarisés de valence) reste stable au cours du temps avec une valeur supérieure à 50%. Nous observons donc directement l'effet de filtrage de spin lié au mécanisme de recombinaison dépendante du spin.

Filtrage de spin dynamique :

Nous avons également confirmé cet effet de filtrage de spin dynamique en réalisant une expérience de spectroscopie de photoluminescence sous pompage optique orienté avec un laser d'excitation de polarisation d'ellipticité variable.

Nous avons ainsi montré qu'en initialisant le système avec une lumière caractérisée par une polarisation circulaire de 88%, nous obtenons le même taux de polarisation circulaire de la photoluminescence après 50 picosecondes que lorsque le laser d'excitation est polarisée circulairement à 100 % (bien que le taux de polarisation mesurée à t=0 est bien sûr plus élevé dans le deuxième cas). L'effet de filtrage de spin est donc efficace tant qu'il y a un déséquilibre entre les

populations d'électrons photogénérés de spin UP et DOWN et que la puissance d'excitation est suffisante pour enclencher la polarisation dynamique des centres.

Dépendance de l'effet SDR avec la fraction d'azote :

La recombinaison dépendante du spin mise en évidence ici est clairement liée à la présence de centres paramagnétiques dans GaAsN. Nous avons vérifié qu'un effet négligeable est mesuré sur des échantillons de GaAs sans azote ou avec une fraction d'azote extrêmement faible (< 0.2 %). Ces centres paramagnétiques sont donc bien corrélés à la présence d'une fraction d'azote significative dans l'échantillon.

Nous avons étudié la dépendance de l'effet SDR pour des échantillons élaborés dans les mêmes conditions dont la composition d'azote varie de 0.7 à 2.1 %. Nous observons que l'effet SDR maximum est mesuré pour des puissances d'excitation laser d'autant plus élevées que la fraction d'azote est importante. Ceci s'explique par une augmentation de la densité de centres paramagnétiques lorsque la fraction d'azote introduit dans l'échantillon croit. Nous avons donc un moyen d'ajuster la concentration de centres paramagnétiques et de mettre en œuvre ainsi une certaine forme d'ingénierie de la recombinaison dépendante du spin. Il s'agit à notre connaissance d'une première dans la mesure où les matériaux pour lesquels la recombinaison dépendante du spin avait été mise en évidence jusqu'ici comportaient des centres paramagnétiques (souvent d'origine inconnue) et dont la densité n'était pas contrôlée.

Identification de la nature des centres paramagnétiques :

Pour identifier la nature des centres paramagnétiques nous avons réaliser des expériences d'ODMR (Optically Detected Magnetic Resonance) en collaboration avec Weimin CHEN de l'Université de Linköping.

Cette technique est particulièrement bien adaptée car elle est sensible à la concentration des électrons de conduction (via l'intensité de la photoluminescence bande de conduction – bande de valence) et à la polarisation de spin des électrons sur les centres paramagnétiques (via l'intensité de la résonance de spin électron, ESR, qui est proportionnelle à la différence de population de spin UP et DOWN des centres). Nous allons donc mesurer les variations d'intensité de photoluminescence induite par les transitions ESR sous un champ magnétique externe.

Après une excitation laser polarisée linéairement, une densité égale d'électrons de spin UP et d'électrons de spin DOWN est photogénérée ; aucune différence de population est donc attendue entre les deux états de spin des centres (la polarisation de spin thermique est négligeable du fait des faibles champs magnétiques externes appliqués ~100-500 mT). Aucun signal ODMR n'est donc observé.

Par contre, après une excitation laser polarisée circulairement, la polarisation dynamique des centres liée à l'effet SDR conduit à une très forte dissymétrie entre les populations de spin UP et DOWN des centres. Le champ micro-onde (9.3 GHz) va entrainer à la résonance une transition entre ces deux états de spin, ouvrant alors un autre canal de recombinaison pour les électrons de conduction. On s'attend donc à observer une chute du signal de photoluminescence liée à la réduction de la densité d'électrons dans la bande de conduction (signal ODMR).

Les observations expérimentales ont été en accord avec ces prédictions et ont en outre permis d'identifier la nature des centres paramagnétiques. Dans le régime de recombinaison dépendante du spin (à puissance d'excitation suffisante), nous n'observons aucun signal ODMR pour une excitation polarisée linéairement alors que des pics ODMR sont clairement identifiés après une excitation laser polarisée circulairement droite ou gauche. L'analyse du signal ODMR a permis de conclure que les centres paramagnétiques étaient des interstitiels de Gallium dont la densité augmente lorsqu'on introduit davantage d'azote dans l'échantillon. Ce résultat nous a surpris car nous nous attendions à trouver un centre plus directement lié à la présence d'azote (paires N-N, agrégats d'azote, etc…)

L'identification est fondée sur les arguments suivants :

Les transitions observées sont liées à l'interaction hyperfine entre un électron de spin ½ et un atome avec deux isotopes de spin 3/2 et une abondance relative 60/40. Ceci conduit à 4 transitions ODMR autorisées pour chaque isotope. Ceci est la signature de l'atome de Gallium

D'autre part, les spectres ODMR ne dépendent pas de l'orientation du champ magnétique appliqué par rapport aux axes cristallographiques de l'échantillon ; ceci confirme que la fonction d'onde de l'électron en interaction avec les spins nucléaires est de type S (interaction de contact de type Fermi). Enfin, le centre devant être paramagnétique pour le mécanisme SDR, ceci exclut un Ga_{As} antisite qui a un état de symétrie T_2 alors que l'interstitiel de Gallium Ga^{2+} a une symétrie T_1.

Pour confirmer que ces interstitiels de gallium sont responsables de l'effet de filtrage de spin nous avons mesuré l'intensité du signal d'ODMR en fonction de la fraction d'azote (et donc de la

concentration de centres paramagnétiques). Nous observons une excellente corrélation entre ces deux quantités pour les différents échantillons étudiés.

Recombinaison dépendante du spin dans des puits quantiques GaAsN/GaAs

Tous les résultats présentés ci-dessus ont été obtenus sur des couches de GaAsN d'épaisseur typique de 100 à 50 nm (sans effet de confinement quantique). Nous avons également démontré que le filtrage de spin à température ambiante était efficace dans des puits quantiques de GaAsN/GaAs d'épaisseur variant de 3 à 9 nm.

CHAPITRE IV

Photoconductivité dépendante du Spin dans GaAsN

Nous montrons dans ce chapitre que la photoconductivité de GaAsN peut être modulée simplement en changeant la polarisation de la lumière d'excitation (sans changer la puissance d'excitation). Ceci est une conséquence directe de la recombinaison dépendante du spin.

Contrôle de la photoconductivité par la polarisation de la lumière

Les mesures de photoconductivité ont été réalisées sur des dispositifs très simples utilisant les mêmes échantillons que ceux étudiés par spectroscopie de photoluminescence au chapitre III de cette thèse : le laser d'excitation est focalisé sur un spot de diamètre de 150 µm entre deux électrodes d'Argent sépares de ~1 mm déposés à la surface de l'échantillon. La lumière laser, polarisée circulairement (Σ^+ ou Σ^-) ou linéairement (Σ^x ou Σ^y) est modulée par un hacheur mécanique à 700 Hz et la photoconductivité est mesurée par une détection synchrone via la variation de tension obtenue sur une résistance de charge placée en série avec l'échantillon. Une tension dans la plage $0 < V < 12$ volts est appliquée entre les deux électrodes. Nous avons effectué ces expériences de photoconductivité à la fois sur des échantillons nominalement non-dopés et des échantillons dopés de type n (*cf.* chapitre II).

Sur l'échantillon dopé n avec une fraction d'azote de 2%, nous avons mesuré des variations de photoconductivité jusqu'à 40 % lorsque la polarisation de la lumière d'excitation passe de circulaire à linéaire. La conductivité de l'échantillon augmente de manière très significative lorsque la lumière d'excitation est polarisée circulairement droite ou gauche, c-à-d quand les électrons photogénérés sont polarisés en spin. Du fait de la recombinaison dépendante du spin, la densité d'électrons libres dans la bande de conduction est plus élevée, pour la même puissance d'excitation laser, avec une excitation polarisée circulairement que linéairement. Pour une excitation polarisée circulairement, la polarisation dynamique des centres paramagnétiques empêche la capture des électrons libres par ces centres (du fait du principe d'exclusion de Pauli) et la densité d'électrons libres moyenne dans la bande de conduction est donc plus importante. La conductivité qui dépend linéairement de la densité d'électrons est alors plus élevée.

Une information précise sur le taux de polarisation des électrons de conduction peut donc être obtenue en mesurant simplement l'intensité du photocourant. Nous avons ainsi mesuré la photoconductivité en fonction de l'état de polarisation du laser d'excitation, de circulaire à linéaire

(en tournant simplement la lame quart d'onde placée après le laser). Comme prévu nous avons observé une loi de type Malus. Nous avons donc ainsi fabriqué un détecteur de spin très simple fonctionnant à température ambiante et sans champ magnétique appliqué.

Cette modulation de la photoconductivité avec la polarisation de l'excitation disparait à très faible puissance d'excitation dans la mesure où le filtrage de spin lié à l'effet SDR n'est plus efficace (plus de polarisation dynamique des centres). Nous observons le même type de dépendance de la photoconductivité dépendante du spin avec la puissance d'excitation du laser que celle mesurée pour le rapport R de recombinaison dépendante du spin obtenu par spectroscopie de photoluminescence (*cf* chapitre III). La modulation de la photoconductivité est observable lorsque les centres paramagnétiques sont polarisés de manière dynamique et cette condition est obtenue pour une densité d'électrons photogénérés de l'ordre de la densité des centres paramagnétiques présents dans l'échantillon.

Influence de la tension appliquée sur la photoconductivité dépendante du spin

Pour une puissance d'excitation fixe nous avons mesuré la variation de la photoconductivité pour différentes tensions appliquées au dispositif dans la gamme O<V < 15 volts.

Lorsque la tension augmente (et donc le courant total injecté de manière optique et électrique), la photoconductivité dépendante du spin chute. La valeur mesurée est maximale (~40%) pour une fiable tension appliquée : le dispositif à base de GaAsN agit dans ces conditions comme un véritable filtre de spin. Pour des tensions appliquées supérieurs à 10 volts, on observe encore une modulation de la photoconductivité de l'ordre de quelques % bien que la densité d'électrons injectés de manière électrique à partir du contact augmente très fortement (comme le montre l'augmentation linéaire du signal de photoconductivité avec la tension appliquée) ; les centres paramagnétiques de GaAsN ne sont plus assez nombreux pour filtrer de manière efficace les électrons non polarisés injectés de manière électrique.

Ces résultats montrent qu'on peut générer un courant polarisé en spin à température ambiante sans champ magnétique appliqué et sans avoir recours à des électrodes magnétiques.

Influence d'un champ magnétique externe

Nous avons également montré que la photoconductivité dépendante du spin chute fortement lorsque l'on applique un champ magnétique externe dans la configuration Voigt (dans le plan de l'échantillon).

Dans cette configuration, le spin des électrons libres de conduction et le spin des électrons localisés sur les centres paramagnétiques vont précesser autour du champ magnétique (notons que ces précessions vont se produire à des vitesses de rotation différente du fait des facteurs de Landé différents pour les deux types d'électron). On prévoit donc que le champ magnétique externe va entrainer une disparition des effets de recombinaison dépendante du spin.

En effet nous avons observé la chute de la photoconductivité dépendante du spin avec le champ magnétique appliqué. En mesurant la photoconductivité, nous avons obtenu à température ambiante une courbe de type effet Hanle, similaire aux courbes standards obtenus par spectroscopie de photoluminescence.

Modélisation de la photoconductivité dépendante du spin

En collaboration étroite avec Alejandro Kunold (Université de Mexico), nous avons développé un modèle de transport dans GaAsN en prenant en compte le mécanisme de recombinaison dépendante du spin. Cette recombinaison est modélisée par des équations d'évolution initialement proposées par V. Kalevich et E. Ivchenko de l'Institut IOFFE de St-Petersbourg (Russie).

Les équations différentielles ont été résolues par la méthode des éléments finis. Les simulations basées sur ce modèle rendent bien compte des variations de la photoconductivité avec

(i) la polarisation du laser d'excitation
(ii) la puissance d'excitation
(iii) le champ magnétique éventuel appliqué en configuration Voigt

Notons d'autre part que le même modèle de recombinaison dépendante du spin permet de reproduire les expériences de filtrage de spin mises en évidence par spectroscopie de photoluminescence : dépendance du rapport SDR avec la puissance, évolution temporelle de la polarisation circulaire de la photoluminescence, effet d'un champ magnétique appliqué en configuration Voigt, *etc…*).

CONCLUSION

Ce travail de thèse nous a permis de montrer que la dynamique de spin électronique dans GaAsN était tout à fait singulière du fait d'un mécanisme très efficace de recombinaison dépendante du spin lié à la présence de centres paramagnétiques.

L'effet de filtrage de spin conduit à des polarisations moyennes de spin très élevées des électrons libres de conduction (> 50%) même à température ambiante. En régime de recombinaison dépendante du spin aucun déclin de la polarisation circulaire de la photoluminescence n'est mesuré.

En exploitant ces effets de filtrage de spin nous avons pu fabriquer et tester un détecteur électrique de la polarisation optique de la lumière basée simplement sur la variation de la photoconductivité. Cette photoconductivité dépendante du spin peut atteindre des valeurs jusqu'à 40% à température ambiante. Ceci démontre les potentialités de GaAsN pour générer un courant polarisé en spin sans utiliser des électrodes magnétiques.

Les expériences d'ODMR ont conduit à l'identification des centres paramagnétiques responsables de la recombinaison dépendante du spin : contrairement à l'intuition qui nous conduisait vers des défauts plus directement liés à l'azote, les centres paramagnétiques à la base des effets de filtrage de spin s'avèrent être des interstitiels de Gallium.

On peut donc imaginer mettre en évidence le même type d'effets dans des échantillons de GaAs sans azote. Des premières structures de GaAs avec une implantation contrôlée de gallium par FIB (Focused Ion Beam) ont été fabriquées au laboratoire de Photonique et de Nanostructures de Marcoussis par J.C. Harmand. Les premiers tests de spectroscopie de photoluminescence réalisés au LPCNO sont très encourageants puisque des effets de recombinaison dépendante du spin ont été mis en évidence. Il s'agit de la perspective la plus importante à l'issue de mon travail de thèse.

D'autre part, l'équipe Optoélectronique du LPCNO envisage d'introduire une couche de GaAsN dans des diodes électroluminescentes polarisées en spin (Spin-LED). Cette couche, insérée entre l'injecteur de spin (Fer ou Cobalt suivi d'une barrière tunnel de MgO) et le détecteur optique de spin (puits ou boîtes quantiques) aura un rôle de filtre de spin supplémentaire du courant injecté à partir de la couche ferromagnétique. Ceci devrait permettre d'augmenter de manière très significative la polarisation de spin du courant injecté dans le puits ou dans les boîtes quantiques de la structure.